NONLINEAR LIGHT GENERATION FROM OPTICAL CAVITIES AND ANTENNAE

Sween J. Butler, M.S.

Dissertation Prepared for the Degree of

DOCTOR OF PHILOSOPHY

UNIVERSITY OF NORTH TEXAS

May 2017

APPROVED:

Arup Neogi, Major Professor
Tae Youl Choi, Committee Member
Vladimir Drachev, Committee Member
Yuri Rostovtsev, Committee Member
Michael Monticino, Interim Chair of the
Department of Physics
David Holdeman, Dean of the College
of Arts and Sciences
Victor Prybutok, Vice Provost of the
Toulouse Graduate School

Butler, Sween J. *Nonlinear Light Generation from Optical Cavities and Antennae*. Doctor of Philosophy (Physics), May 2017, 171 pp., 5 tables, 68 figures, chapter references.

Semiconductor based micro- and nano-structures grown in a systematic and controlled way using selective area growth are emerging as a promising route toward devices for integrated optical circuitry in optoelectronics and photonics field. This dissertation focuses on the experimental investigation of the nonlinear optical effects in selectively grown gallium nitride micro-pyramids that act as optical cavities, zinc oxide submicron rods and indium gallium nitride multiple quantum well core shell submicron tubes on the apex of GaN micro pyramids that act as optical antennae. Localized spatial excitation of these low dimensional semiconductor structures was optimized for nonlinear optical light (NLO) generation due to second harmonic generation (SHG) and multi-photon luminescence (MPL). The evolution of both processes are mapped along the symmetric axis of the individual structures for multiple fundamental input frequencies of light. Effects such as cavity formation of generated light, electron-hole plasma generation and coherent emission are observed. The efficiency and tunability of the frequency conversion that can be achieved in the individual structures of various geometries are estimated. By controlling the local excitation cross-section within the structures along with modulation of optical excitation intensity, the nonlinear optical process generated in these structures can be manipulated to generate coherent light in the UV-Blue region via SHG process or green emission via MPL process. The results show that these unique structures hold the potential to convert red input pulsed light into blue output pulsed light which is highly directional.

ACKNOWLEDGEMENTS

First of all, I would like to thank God for giving me the endurance to successfully finish the path of a doctoral candidate. I must thank the two gentlemen in my life, my husband Michael Butler and our son Alexander Butler for their unwavering support, patience, love and understanding. Without them being at my side, I would not have completed this dissertation.

I would like to thank my dissertation advisor, Dr. Arup Neogi for providing me the opportunity, guidance, resources and inspiration needed to complete this work. I am greatly indebted to my committee members, Dr. Yuri Rostovtsev, Dr. Vladimir Drachev and Dr. Tae Youl Choi for the time, effort, guidance, knowledge and encouragement provided in completing this work. I would like to thank Drs. Mohammed Fikry and Klaus Thonke from Ulm University, Germany and Dr. Hongxing Jiang from Texas Tech University for providing samples used in this study. Thanks to David Jaeger at the Center for Advanced Research & Technology, University of North Texas for his technical assistance with SEM and FIB milling. I would like to acknowledge Dr. Brian Gorman at the Colorado School of Mines for doing the TEM measurements.

My lab mates and former graduates Drs. Ezekiel Walker and Ben Urban deserve to be acknowledged for the invaluable aid they provided for my research. I would also like to thank my friends, my peers and colleagues who have influenced me and helped me during my time at the department of Physics. I also appreciate the support from the Physics department staff at the financial office, electronic shop and machine shop. I would like to acknowledge the financial support from the Toulouse graduate school through Graduate Assistantship Tuition Scholarship and the Thesis Dissertation Fellowship award. Last but not least, I would like to thank my parents for providing me a good foundation for life.

TABLE OF CONTENTS

LIST OF ABBREVIATIONS

2D - two dimensional

3D - three dimensional

AlGaN - Aluminium gallium nitride

AlN - Aluminum nitride

CdS - Cadmium sulphide

ELO - Epitaxial layer overgrowth

FIB - Focused ion beam

fs - Femtosecond

GaN - Gallium nitride

III-N - Group III nitride

InGaN - Indium gallium nitride

InN - Indium nitride

InP - Indium phosphide

$KNbO_3$ - Potassium niobate

LD - Light diodes

LED - Light emitting diode

MOCVD - Metal-organic chemical vapor deposition

MPL - Multi photon luminescence

NA - Numerical aperture

NIR - Near infra-red

NLO - Nonlinear light generation

PhC - Photonic crystal

PL - Photoluminescence

SAE - Selective area epitaxy

SA-ELO - Selective area epitaxial layer overgrowth

SAG - Selective area growth

SEM - Scanning electron microscopy

SFG - Sum frequency generation

SHG - Second harmonic generation

SMR - Submicron rod

SMT - Submicron tube

TEM - Transmission electron microscopy

TRPL - Time resolved photoluminescence

UV - Ultra violet

UVL - Ultra violet luminescence

VLS - Vapor–liquid–solid method

WGM - Whispering gallery mode

YL - Yellow luminescence

ZnO - Zinc oxide

ZnTe - Zinc telluride

CHAPTER 1

INTRODUCTION

1.1 Context and Motivation

Nonlinear optics is an exciting, active research area in the optical and photonic sciences. Photonics involve the use of light to perform functions that are traditionally achieved using electronics; for example, fiber optics in telecommunications. The increasing demand for faster access to information drives the photonics research field to develop new concepts for the engineering, guiding and/or storing of light. In fact, one of the main gaps in the photonics field is the availability of potential nonlinear materials that can replace the current nonlinear crystals, which not only require strict momentum matching conditions to obtain tunable ultraviolet (UV) - blue pulsed laser light, but these blue pulsed laser systems are expensive and are hard to transport. In sharp contrast, the nonlinear optical (NLO) materials have a nonlinear response to the electric field associated with the light of a laser beam. This special property results in a variety of attractive optical phenomena, such as self-controlled light propagation and generation of a different color of light than the incident light; both can be used to accomplish feats ranging from measureable increases in communication speeds to bio-imaging with minimal negative impact on the examined specimen. Therefore, finding potential media with good nonlinear optical properties is fundamentally important to achieve micro- or nano-scale devices such as tunable source of coherent laser radiation for use in the physical, information and biological sciences that is stable at room temperature and physiological conditions, and are also cost effective and efficient.

Optical cavities and antennas can be used to generate and manipulate light at the micro- and nano-scale[1]. Both these functions are key to the realization of compact photonic devices. Optical cavities confine light to small volumes by resonant recirculation; whereas optical antennas collect free space light and confine into a small volume or radiate light from a confined volume out to the free space. Optical cavities and antennas can increase the nonlinear conversion efficiency of light. Realization of control of NLO light was explored by the use of metallic nanostructures[2] utilizing surface plasmons localized at the surfaces. However, large resistive heating losses and lack of noncentrosymmetry in metals affects the efficiency of generation of up-converted light and its control. On the other hand, exists dielectric cavities and antennas that possess high nonlinear susceptibilities without ohmic losses that exhibit strong resonances in the visible-NIR spectrum of light. Semiconductor low dimensional structures with high dielectric constant can form optical cavities that can efficiently confine light in this frequency range[1]. Also, semiconductor materials with lack of inversion symmetry exhibit bulk nonlinearity, which can generate NLO light efficiently[3]. Optical cavities consist of Fabry-Pérot[4] and whispering gallery resonators[5] as well as photonic crystals[6].

Three dimensionally grown semiconductor micro- and nano- structures such as rods, tubes, cones, prisms and pyramids have gained considerable attention as promising route toward devices for integrated optical circuitry in optoelectronics and photonics field[7–9]. Driven by this possibility, majority of the focus is on understanding the formation mechanism of these structures, improving the fabrication process, electrical and optical properties of the structures. These structures are formed by methodically growing the semiconductor material on a-, r- and m-planes and are commonly referred as semi-polar and non-polar structures, whereas, the most commonly grown crystallographic direction is c-plane known as polar structures. Advantages of these non-planar structures are high aspect ratio providing large surface-to-volume, improved light extraction efficiency and reduction in dislocation densities[10,11]. Besides, low dimensional structures owing to their small footprint on the substrate help relax the strain induced by thermal expansion mismatch. This avoids generation of cracks, which is a big problem in the growth industry due to growth on substrates with large lattice mismatches[12]. Also, as the dimensionality of the material decreases from bulk size to micro or nano-size, attractive phenomena arise that are significantly different from the properties of the same matter at the bulk scale. Several researchers have studied different shapes of micro and nano structures. While interesting phenomena were observed, the results were difficult to quantify because the samples under investigation often had randomly grown structures; hence the measured response was averaged over many individual features. This often led to qualitative conclusions about the physical origins of the observed phenomena. Recent progress in semiconductor growth technology has made it possible to fabricate nano and micro structures in a systematic and controlled way using selective area growth (SAG) or selective area epitaxy (SAE)[13–16]. This level of controlled growth of micro and nano structures enables movement from qualitative to quantitative measurement of properties from individual structures and their interaction between neighboring structures to make unambiguous conclusions. From a device processing perspective, controlled fabrication ensures consistent and reproducible performance that cannot be realized otherwise, and progresses the science to a practical technology.

The nonlinear optical response of low dimensional structures is of current interest because of the need for active elements in photonic applications. Some of the demonstrated application potentials include local excitation sources[17,18], crystallographic study of semiconducting structures[19], single nanowire optical correlator[20] and frequency conversion in a 2D photonic crystal[6]. Nonlinear optical effects such as second harmonic generation (SHG), sum frequency generation (SFG) etc. are preferred as they can be used to make coherent sources; especially doubling a source with optical communication band frequency[6,21]. SHG process has been reported from ZnO[22], GaN[23], $KNbO_3$[17], CdS[24,25], ZnTe[26,27] and InP[5] nanowires. Two photon absorption induced luminescence (TPL), a nonlinear optical effect has made significant contributions to the microscopy and imaging of biological specimens[28,29]. Similarly, SHG has also shown to be viable tool for biological imaging[30]. Input optical pump density dependence on the two-photon induced luminescence and second harmonic generation leads to spatial confinement improving resolution in imaging field. Moreover, sharp boundaries and interfaces with small dimensions possesses high charge density and electrostatic potential gradients which increases the total dipole moments, thus increasing their nonlinearity[31]. GaN and ZnO; highly transparent optical materials which lack crystal lattice inversion symmetry with high nonlinear susceptibility co-efficients[22,32–35], are good candidates which can be accessed for study, such as second harmonic generation (SHG) and multiphoton induced luminescence (MPL). Linear optical response of these micro/nano structures has been extensively studied; however, studies on the nonlinear optical response from micro-nano structures grown discretely using controlled methods is still in its infancy. Majority of the studies available on individual structures are done on sample structures that are extracted from randomly grown structures. Examples of nonlinear studies in semiconductor micro-nano scale structures include far field imaging of SHG in single GaN nanowire[23], resonant SHG in a GaN 2D photonic crystal[6], frequency conversion via SHG in bulk

ZnO nanorods[36], single ZnO nanowires[22] and nanorods[37], coupling of SHG to nanocavity Fabry-Pérot modes in ZnO nanocombs[38], and competition between SHG and two-photon induced luminescence in ZnO nanorods[39].

This dissertation focuses on the experimental investigation of the nonlinear optical processes in vertically standing individual semiconductor micro and nano structures from an array of selectively grown GaN micro-pyramids, GaN micro-pyramids with a zinc oxide (ZnO) submicron rod or GaN submicron tube on the apex of the pyramid, and indium gallium nitride (InGaN)/GaN multiple quantum well core shell submicron tubes on the apex of GaN micro pyramids. This study aims to estimate 1) the efficiency and range of the frequency conversion that can be achieved using semiconductor micro-cavities 2) whether the light emission from GaN micro pyramids is being efficiently harvested using ZnO or GaN nanorods as optical antennae, 3) how to control the nonlinear processes in these structures and 4) the effect of InGaN/GaN multi quantum well nanowire on the nonlinear light generation. I have experimentally determined the range of frequency conversion in the blue region that can be achieved in these vertically standing individual structures of various geometries. My results show that these unique structures hold the potential to convert red input pulsed light into blue output pulsed light which is highly directional. I have quantified that SHG from these structures can be selectively turned on using low optical excitation intensity. Also, controlling the local excitation cross-section within the structures along with modulation of optical excitation intensity, the nonlinear optical process generated in these structures can be manipulated. This correlation between observation and quantification implies that by controlling the optical excitation density, light-matter interaction length and absorption cross section, these structures can be utilized to generate coherent light in the UV-Blue region via SHG process or green emission via MPL process.

Besides laser diodes and optoelectronics applications, these nanostructures can be used to make a bio-sensing assay, where proteins of different emission wavelengths can be selectively excited on a single platform. Although not demonstrated in this dissertation, this can be achieved by incorporating a biocompatible polymer based multi-well plate assay on these micro-structures, where each well is critically aligned with an individual structure. By generating the appropriate frequency needed for the excitation of these proteins, biological specimen tagged with multiple fluorescent proteins loaded in each well can be selectively excited. This bio-sensing platform would provide an inbuilt coherent source with a narrow optical spectrum that can be tuned to increase the throughput of the assay; provided the proteins itself do not have nonlinear emission.

1.2 Overview of Dissertation

This dissertation is organized as follows.

Chapter 2 is purposed to brief the fundamental properties of the materials and concepts that underlay the foundation of this dissertation. Here, I introduce the basics of group III nitrides and its alloys such as their material properties, challenges in their growth, why nitrides are going non-planar, and state-of-the-art on the growth of these non-planar 3D structures. A brief introduction to ZnO is provided. An introduction to nonlinear optics and some of the fundamental nonlinear properties studied in this dissertation are discussed. Also, the experimental techniques used in this work is briefly discussed in this chapter.

Chapter 3 provides an insight into the nonlinearity in GaN hexagonal micro-pyramid emitters. It discusses the results of the structural, linear and nonlinear optical studies of GaN micro-pyramids fabricated using MOCVD growth. A spatial mapping of the nonlinearity along the symmetric axis of the micro-pyramid shows spatial variation of second- and third order nonlinearity. Optimum cross-sections for both nonlinearities are determined. Frequency conversion due to second order nonlinearity was found to be maximum because of the confinement of fundamental and harmonic frequency via formation of quasi-whispering gallery modes.

Chapter 4 explores the role of micron and submicron size GaN and ZnO based emitters on the generation and propagation of second harmonic and multiphoton luminescence. This chapter studies the polarization dependence of the nonlinear light generation on the fundamental light, which provides an insight into the origin of the polarity of the nonlinear light generation in these structures.

Chapter 5 discusses the results of optical and structural characterization of InGaN/GaN co-axial submicron tubes (SMTs) on GaN pyramids. InGaN/GaN co-axial SMTs are grown using ZnO submicron rods as templates. Therefore, structural and light matter interaction of step wise growth is presented. Temporal dynamics of the quantum well emission is explored from linear and nonlinear perspective. Finally, the origin of nonlinear light generation and spectral characteristics are detailed in this chapter.

Chapter 6 concludes with the summary of this dissertation work, achievements of this work and future outlook.

1.3 References

(1) Vahala, K. J. Optical Microcavities. *Nature* **2003**, *424* (6950), 839–846.

(2) Kauranen, M.; Zayats, A. V. Nonlinear Plasmonics. *Nat. Photonics* **2012**, *6* (11), 737–748.

(3) Peyghambarian, N.; Koch, S. W.; Mysyrowicz, A. *Introduction to Semiconductor Optics*; Prentice Hall series in solid state physical electronics; Prentice Hall: Englewood Cliffs, N.J, 1993.

(4) Coulon, P.-M.; Hugues, M.; Alloing, B.; Beraudo, E.; Leroux, M.; Zuniga-Perez, J. GaN Microwires as Optical Microcavities: Whispering Gallery Modes Vs Fabry-Perot Modes. *Opt. Express* **2012**, *20* (17), 18707.

(5) Wang, F.; Reece, P. J.; Paiman, S.; Gao, Q.; Tan, H. H.; Jagadish, C. Nonlinear Optical Processes in Optically Trapped InP Nanowires. *Nano Lett.* **2011**, *11* (10), 4149–4153.

(6) Zeng, Y.; Roland, I.; Checoury, X.; Han, Z.; Kurdi, M. E.; Sauvage, S.; Gayral, B.; Brimont, C.; Guillet, T.; Mexis, M.; Semond, F.; Boucaud, P. Resonant Second Harmonic Generation in a Gallium Nitride Two-Dimensional Photonic Crystal on Silicon. *Appl. Phys. Lett.* **2015**, *106* (8), 81105.

(7) Duan, X.; Huang, Y.; Cui, Y.; Wang, J.; Lieber, C. M. Indium Phosphide Nanowires as Building Blocks for Nanoscale Electronic and Optoelectronic Devices. *Nature* **2001**, *409* (6816), 66–69.

(8) Huang, M. H.; Mao, S.; Feick, H.; Yan, H.; Wu, Y.; Kind, H.; Weber, E.; Russo, R.; Yang, P. Room-Temperature Ultraviolet Nanowire Nanolasers. *Science* **2001**, *292* (5523), 1897–1899.

(9) Crowley, M. T.; Kovanis, V.; Lester, L. F. Breakthroughs in Semiconductor Lasers. *IEEE Photonics J.* **2012**, *4* (2), 565–569.

(10) Li, S.; Waag, A. GaN Based Nanorods for Solid State Lighting. *J. Appl. Phys.* **2012**, *111* (7), 71101.

(11) Paskova, T. Development and Prospects of Nitride Materials and Devices with Nonpolar Surfaces. *Phys. Status Solidi B* **2008**, *245* (6), 1011–1025.

(12) Zubia, D.; Hersee, S. D. Nanoheteroepitaxy: The Application of Nanostructuring and Substrate Compliance to the Heteroepitaxy of Mismatched Semiconductor Materials. *J. Appl. Phys.* **1999**, *85* (9), 6492.

(13) Kitamura, S.; Hiramatsu, K.; Sawaki, N. Fabrication of GaN Hexagonal Pyramids on Dot-Patterned GaN/Sapphire Substrates via Selective Metalorganic Vapor Phase Epitaxy. *Jpn. J. Appl. Phys.* **1995**, *34* (Part 2, No. 9B), L1184–L1186.

(14) Scholz, F. Semipolar GaN Grown on Foreign Substrates: A Review. *Semicond. Sci. Technol.* **2012**, *27* (2), 24002.

(15) Lundskog, A.; Forsberg, U.; Holtz, P. O.; Janzén, E. Morphology Control of Hot-Wall MOCVD Selective Area Grown Hexagonal GaN Pyramids. *Cryst. Growth Des.* **2012**, *12* (11), 5491–5496.

(16) Choi, K.; Arita, M.; Arakawa, Y. Selective-Area Growth of Thin GaN Nanowires by MOCVD. *J. Cryst. Growth* **2012**, *357*, 58–61.

(17) Nakayama, Y.; Pauzauskie, P. J.; Radenovic, A.; Onorato, R. M.; Saykally, R. J.; Liphardt, J.; Yang, P. Tunable Nanowire Nonlinear Optical Probe. *Nature* **2007**, *447* (7148), 1098–1101.

(18) Dutto, F.; Raillon, C.; Schenk, K.; Radenovic, A. Nonlinear Optical Response in Single Alkaline Niobate Nanowires. *Nano Lett.* **2011**, *11* (6), 2517–2521.

(19) Ren, M.-L.; Agarwal, R.; Liu, W.; Agarwal, R. Crystallographic Characterization of II–VI Semiconducting Nanostructures via Optical Second Harmonic Generation. *Nano Lett.* **2015**, *15* (11), 7341–7346.

(20) Yu, H.; Fang, W.; Wu, X.; Lin, X.; Tong, L.; Liu, W.; Wang, A.; Shen, Y. R. Single Nanowire Optical Correlator. *Nano Lett.* **2014**, *14* (6), 3487–3490.

(21) Mariani, S.; Andronico, A.; Lemaître, A.; Favero, I.; Ducci, S.; Leo, G. Second-Harmonic Generation in AlGaAs Microdisks in the Telecom Range. *Opt. Lett.* **2014**, *39* (10), 3062.

(22) Johnson, J. C.; Yan, H.; Schaller, R. D.; Petersen, P. B.; Yang, P.; Saykally, R. J. Near-Field Imaging of Nonlinear Optical Mixing in Single Zinc Oxide Nanowires. *Nano Lett.* **2002**, *2* (4), 279–283.

(23) Long, J. P.; Simpkins, B. S.; Rowenhorst, D. J.; Pehrsson, P. E. Far-Field Imaging of Optical Second-Harmonic Generation in Single GaN Nanowires. *Nano Lett.* **2007**, *7* (3), 831–836.

(24) Barrelet, C. J.; Ee, H.-S.; Kwon, S.-H.; Park, H.-G. Nonlinear Mixing in Nanowire Subwavelength Waveguides. *Nano Lett.* **2011**, *11* (7), 3022–3025.

(25) Ren, M.-L.; Liu, W.; Aspetti, C. O.; Sun, L.; Agarwal, R. Enhanced Second-Harmonic Generation from Metal-Integrated Semiconductor Nanowires via Highly Confined Whispering Gallery Modes. *Nat. Commun.* **2014**, *5*, 5432.

(26) Liu, W.; Wang, K.; Liu, Z.; Shen, G.; Lu, P. Laterally Emitted Surface Second Harmonic Generation in a Single ZnTe Nanowire. *Nano Lett.* **2013**, *13* (9), 4224–4229.

(27) Barzda, V.; Cisek, R.; Spencer, T. L.; Philipose, U.; Ruda, H. E.; Shik, A. Giant Anisotropy of Second Harmonic Generation for a Single ZnSe Nanowire. *Appl. Phys. Lett.* **2008**, *92* (11), 113111.

(28) Denk, W.; Strickler, J. H.; Webb, W. W. Two-Photon Laser Scanning Fluorescence Microscopy. *Science* **1990**, *248* (4951), 73–76.

(29) So, P. T. C.; Dong, C. Y.; Masters, B. R.; Berland, K. M. Two-Photon Excitation Fluorescence Microscopy. *Annu. Rev. Biomed. Eng.* **2000**, *2* (1), 399–429.

(30) Campagnola, P. J.; Loew, L. M. Second-Harmonic Imaging Microscopy for Visualizing Biomolecular Arrays in Cells, Tissues and Organisms. *Nat. Biotechnol.* **2003**, *21* (11), 1356–1360.

(31) Ebothé, J.; Kityk, I. V.; Fuks-Janczarek, I. Two-Photon Absorption Study of the Large-Sized Nanocrystallites. *Appl. Surf. Sci.* **2006**, *252* (16), 5763–5767.

(32) Miragliotta, J.; Wickenden, D. K.; Kistenmacher, T. J.; Bryden, W. A. Linear- and Nonlinear-Optical Properties of GaN Thin Films. *J. Opt. Soc. Am. B* **1993**, *10* (8), 1447–1456.

(33) Angerer, W. E.; Yang, N.; Yodh, A. G.; Khan, M. A.; Sun, C. J. Ultrafast Second-Harmonic Generation Spectroscopy of GaN Thin Films on Sapphire. *Phys. Rev. B* **1999**, *59* (4), 2932–2946.

(34) Kim, D.; Libon, I. H.; Voelkmann, C.; Shen, Y. R.; Petrova-Koch, V. Multiphoton Photoluminescence from GaN with Tunable Picosecond Pulses. *Phys. Rev. B* **1997**, *55* (8), R4907–R4909.

(35) Abe, M.; Awata, N.; Matsushita, T.; Hakamata, M.; Ozawa, K.; Murakami, R.; Shoji, I.; Kondo, T. Accurate Measurement of Quadratic Nonlinear-Optical Coefficients of Zinc Oxide. *J. Opt. Soc. Am. B* **2012**, *29* (9), 2392.

(36) Chan, S. W.; Barille, R.; Nunzi, J. M.; Tam, K. H.; Leung, Y. H.; Chan, W. K.; Djurišić, A. B. Second Harmonic Generation in Zinc Oxide Nanorods. *Appl. Phys. B* **2006**, *84* (1–2), 351.

(37) Liu, W.; Wang, K.; Long, H.; Chu, S.; Wang, B.; Lu, P. Near-Resonant Second-Order Nonlinear Susceptibility in c-Axis Oriented ZnO Nanorods. *Appl. Phys. Lett.* **2014**, *105* (7), 71906.

(38) Capeluto, M. G.; Grinblat, G.; Tirado, M.; Comedi, D.; Bragas, A. V. Nonlinear Excitation of Polariton Cavity Modes in ZnO Single Nanocombs. *Opt. Express* **2014**, *22* (5), 5341.

(39) Dai, J.; Zeng, J.-H.; Lan, S.; Wan, X.; Tie, S.-L. Competition between Second Harmonic Generation and Two-Photon-Induced Luminescence in Single, Double and Multiple ZnO Nanorods. *Opt. Express* **2013**, *21* (8), 10025.

CHAPTER 2

FUNDAMENTALS, MATERIALS AND METHODS

This chapter's purpose is to give an understanding about the fundamentals of materials and methods used in this dissertation work. The first part provides a comprehensive description of GaN and its alloys, challenges in their growth, why nitride material are going non-planar, and state-of-the-art on the growth of these non-planar 3D structures. It also provides basic properties of ZnO. The second part introduces the background to nonlinear optics and some of the fundamental nonlinear properties studied in this dissertation. The third section of this chapter provides some insights into the luminescence properties of the semiconductors used in this study and the techniques used to measure and study them.

2.1 Introduction to Group III Nitrides

Group III Nitrides refer to gallium nitride, indium nitride (InN), aluminum nitride (AlN), and their alloys such as InGaN and AlGaN. GaN, a representative of this group is the second mature semiconductor material behind silicon in the market for electronics, optoelectronics and photonic applications. Although research on GaN goes back to the late 1960s[40], it was in the late 1980s GaN research made a breakthrough progress. The credit goes to H. Amano and I. Akasaki, who fabricated high quality GaN epi-layers[41] (1986) and obtained high p-type doping[42] (1989). The major turn in this field happened with the demonstration of nitride based blue light emitting diodes (LEDs) by S. Nakamura in 1993[43]. These scientists were awarded Nobel Prize in 2014 for their contributions to nitride base lighting. Nakamura's discovery opened up the enormous market potential for replacing conventional lighting sources such as filament bulbs and fluorescent tube lights. Driven by this, significant efforts have been invested in the development of low energy consuming, efficient and long lasting LEDs which emit visible light. The technological significance of GaN based optical devices comes from the fact that they can emit bright light in a wide range of colors and temperatures because the band gap of GaN and thus emission range can be tuned from IR to deep UV by alloying with other group III elements. AlN, GaN and InN are direct band gap semiconductors; therefore, a photon can be directly generated from an electron-hole pair within the band gap without the assistance of a phonon. The bandgap energies of AlN, GaN, and InN are 6.2, 3.4, and 0.7 eV at room temperature which cover the entire visible spectrum from the IR to the deep UV range. Besides LEDs, GaN has found a place in large area displays, traffic lights, vehicle lights, street lighting, and laser diodes. GaN based LD's are the backbone of Blu-ray technology; the current standard for high definition storage disks. III-nitride semiconductors also have strong chemical bonds[44], which makes the nitrides very stable and resistant to degradation under high electric fields and temperatures. Combination of wide band gap and high breakdown voltage properties have found GaN in a demanding application; high electron mobility transistors (HEMT)[45]. GaN HEMT is an indispensable component for power amplifiers for transmission of wireless communication systems and radar systems, which need high-output power and high efficiency performance.

2.1.1 Crystal Structure

Group III nitrides crystallizes mainly in the form of wurtzite (hexagonal) and zinc blende (cubic) lattice structures; however, under thermodynamically stable conditions, GaN takes the form of wurtzite structure. The samples studied in this work has wurtzite structure, also known as α-GaN. The wurtzite structure has a hexagonal unit cell with two lattice constants: the in-plane lattice constant, a (edge length of the basal plane of the hexagonal cell) and an out of plane lattice constant, c (the height of the cell) as represented by figure 2.1. The internal parameter u represents the relative length of the III-N bonds parallel to the c-axis, and is represented in units of c. Each unit cell consists of two embedded hexagonal close-packed (HCP) sublattices, each with one type of atom, offset by 5/8 of the cell height (5c/8) along the c-axis. Each sublattice has either a group III metal atom or nitrogen atom in its center, bonded to four atoms of the other species in a tetrahedral configuration, T.

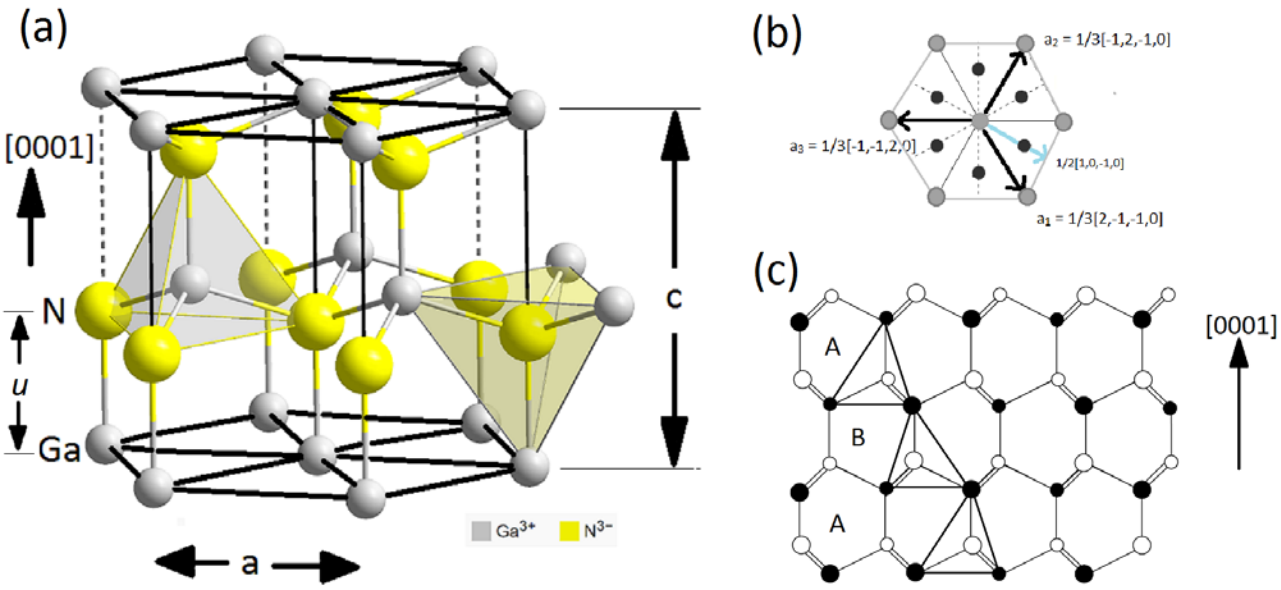

Figure 2.1. The crystal structure of wurtzite GaN. a) Wurtzite structure consisting of two hexagonally close-packed sub-lattices, b) Bravais-Miller index of wurtzite GaN structure, c) Wurtzite ABABA stacking sequence along [0001] axis.

The basal plane of this structure is defined by one face of the tetrahedron and the bond perpendicular to this plane defines the c-axis; where +c direction is represented by a vector pointing from group III atom to the nitrogen atom. Nitride crystals are anisotropic in nature because their lattice parameters are not equal (c ≠ a, which gives rise to unique properties. The crystal surfaces, directions and planes of a hexagonal unit cell of wurtzite structure can be described using Miller-Bravais indices (hkil). In this notation, i = − (h + k) because the three basis vectors a_1, a_2 and a_3 in the basal plane have an angle of 120^0 as shown in figure 2.1 and the fourth vector a_4 lies perpendicular to the basal plane in the c-direction. The wurtzite structure consists of alternating biatomic close-packed (0 0 0 1) planes of Ga and N pairs forming a stacking sequence of *ABABA…* in the [0 0 0 1] direction. The wurtzite structure has a space grouping and point group symmetry of P63mc and 6mm (Hermann–Mauguin notation), respectively. For clarity, the notations (hkil), [hkil] and {hkil} represent surfaces, directions and crystallographic planes.

2.1.2 Polarity

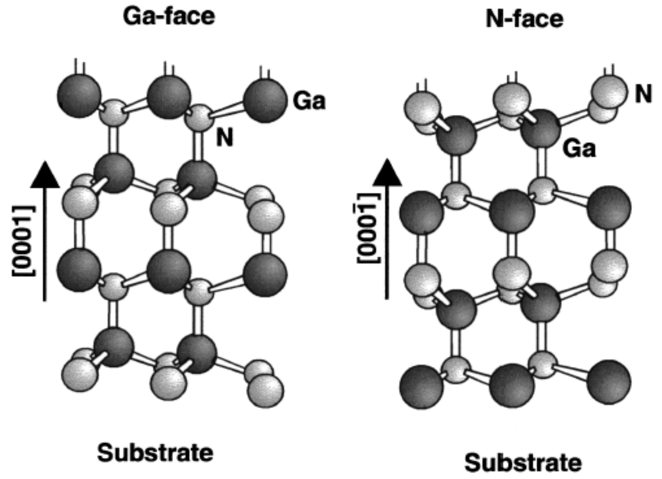

Figure 2.2. Schematic representing the two polarities of GaN with Ga- face and N- face orientations.

The wurtzite structure is non-centrosymmetric; in other words, their lattice lack inversion symmetry (hence asymmetric) in the [0001] direction (c-axis). This means that the orientation/configuration of crystal structure in [0001] direction is invariant to the configuration of crystal structure in $[000\bar{1}]$ direction. As a result, a finite wurtzite III-nitride crystal possesses two distinguishable surfaces that exhibits different surface morphology, chemical reactivity and growth conditions. The surfaces have identical structure, but the opposite set of elements, thus determining the polarity of the surface as shown in figure 2.2[46]. The (0001) surface with Ga atoms on the top surface is referred to as the “Ga- face” and the $(000\bar{1})$ surface with nitrogen atoms is called “N-face”. The {0001} or c-planes are usually referred to as “polar” GaN and is the mostly grown and studied orientation because of the maturity of their growth processes.

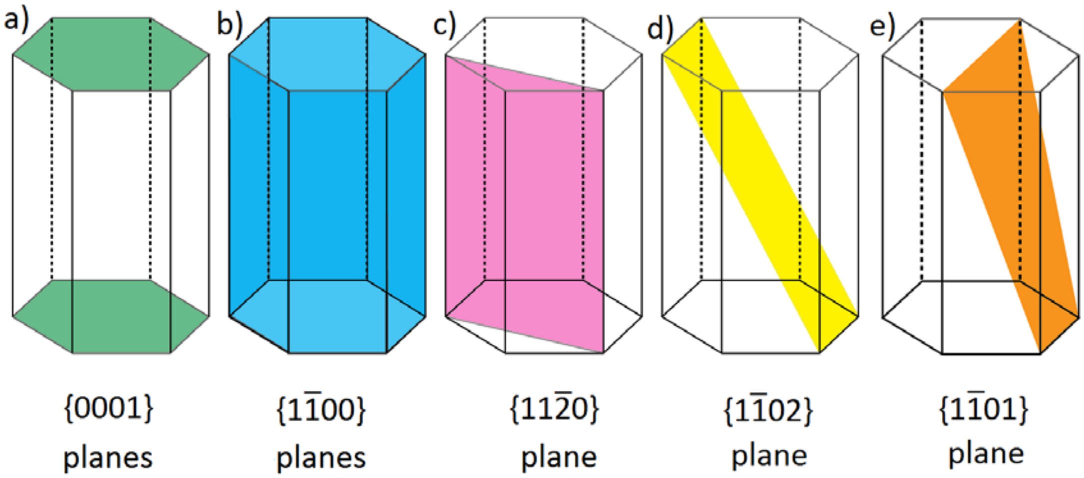

Figure 2.3. Schematic views of different planes of wurtzite GaN crystal. (a) represents polar, (b) and (c) represents non-polar and (d) and (e) represents semi-polar planes.

Besides polar c-plane, there are two other important types of crystal planes: the nonpolar and the semi-polar. The non-polar corresponds to planes with $l = 0$ in the standard Miller-Bravais notation $\{hkil\}$ and the semi-polar are the planes with nonzero h or k and nonzero l. Figure 2.3 illustrates the crystal planes of GaN. The {0001} plane (the c-plane) is known as polar planes. The $\{1\bar{1}00\}$ and $\{11\bar{2}0\}$ planes; otherwise known as m- and a- planes are classified as non-polar planes, while the $\{1\bar{1}01\}$ and $\{1\bar{1}02\}$ planes are classified into semi-polar planes.

2.1.3 Lattice Parameters

As mentioned earlier, the basal plane lattice parameter, the axial lattice parameter and the internal parameter are represented by letters a, c and u, respectively. In an ideal wurtzite structure, value of the ratio of lattice parameters, c/a is 1.633 and that of internal parameter u is

0.375. However, the values of internal parameter u and the ratio c/a deviates from the ideal values during growth due to the distortion in bond angles from ideal angles. As a consequence, hexagonal nitrides show large bond ionocities. The values of the lattice parameters for AlN, GaN, and InN at 300 K are listed in table 2.1[47].

Table 2.1. Lattice constants and thermal expansion coefficients for group III-nitride binary alloys[7,8].

Parameters (T = 300 K)	GaN	AlN	InN
a [Å]	3.189	3.112	3.545
c [Å]	5.185	4.982	5.703
u	0.376 c	0.380 c	0.377 c
TEC (10^{-6} K^{-1})	a 5.59/ c 3.17	a 4.15 / c 5.27	

For ternary alloys such as $In_xGa_{1-x}N$ and $Al_xGa_{1-x}N$, the compositional dependence of the lattice parameters are usually approximated by Vegard's law[48]:

$$a_{A_{(x)}B_{(1-x)}N} = (x)a_A + (1-x)a_B$$

$$c_{A_{(x)}B_{(1-x)}N} = (x)c_A + (1-x)c_B \tag{2.1}$$

where *a* and *c* represents lattice parameters, *A* represents either InN or AlN and *B* represents GaN, and *x* represents the molar fraction.

The coefficient of thermal expansion relates change of volume of the material to change in temperature. Normally, III-nitrides are grown at elevated temperatures than the room temperature. For instance, epitaxy of GaN is conducted at temperatures ranging from 500 °C to 1000 °C depending on the epitaxial method. In heteroepitaxy, the substrate and epi-layer are different materials and thus have different coefficients of thermal expansion. Therefore, thermal expansion of these materials plays a major role in the crystalline quality. The thermal expansion co-efficients (TECs) of III-nitrides[46] are included in table 2.1. The mismatch in TECs between epi-layers and the substrate combined with lattice mismatch plays a key role in the introduction of defects in the epitaxial growth process.

2.1.4 Band Structure

The electrical and optical properties of semiconductors are mainly determined by the electronic band structure near the Γ point on the momentum axis. The concept of electronic band formation comes from the fact that atoms in a solid are closely packed and their outer orbitals begin to overlap with each other. The overlapping orbitals interact strongly broadening the discrete levels of free atoms into bands. Optical transitions can occur between the bands if they are allowed by the selection rules. Since the transition is between two broad bands; otherwise called interband absorption, it can be over a continuous range of photon energies as determined by the lower and upper limits of the energy bands. The highest occupied band is called the valence band while the lowest unoccupied band is called the conduction band with Fermi level lying within the energy gap between the two aforementioned bands. To excite electrons from the valence band to the empty states of the conduction band, it takes energy equal to or greater than the band gap, E_g. Excitation of an electron in to the conduction band leaves an empty state in the valence band called a hole, which acts as a positive charge. When the conduction happens by thermally excited electrons and holes in a semiconductor, it is called intrinsic semiconductor. Impurities with extra electrons can be introduced into the crystal during growth which act as donors and these extra electrons lie in the donor levels just below the conduction band. The electrons in the donor levels can be easily excited to the conduction band at room temperature. This is called an n type extrinsic semiconductor. Similarly, impurities with a deficit of electrons can be introduced into the crystal giving rise to a p-type extrinsic semiconductor. Such impurity atoms make up acceptor levels that lie just above the top of valence band and can accept electrons from the valence band. Electrons can be easily excited to these states at room temperature.

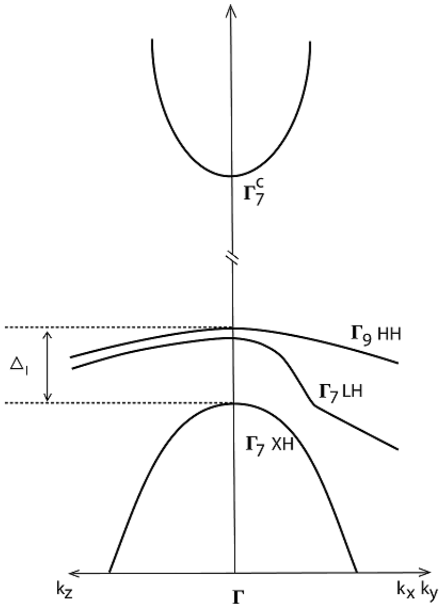

Figure 2.4. Schematic representation of the Γ point valence and conduction bands in wurtzite GaN. Spin-orbit splitting leads to the bands labeled HH and LH. Crystal field splitting creates band labeled as XH.

III-nitrides are direct bandgap semiconductors which means the energies of both the conduction band minimum and valence band maximum lie Γ point. The bottom of the conduction band is primarily formed from the s-levels of Ga atoms and the upper valence band states form the p-levels of N atoms[49]. The band structure of GaN near k = 0 is shown in figure 2.4. Because of the asymmetry of WZ structure, valence band of GaN is split into three excitonic sub-bands: heavy holes (denoted by A), light holes B, and split-off band C, with the crystal field splitting and spin-orbit splitting taken into account. The band gap energies of the group III nitrides cover from 0.7 eV (near infrared) to 6.2eV (ultra-violet) as shown in figure 2.5. An undoped GaN crystal has a bandgap of 3.4 eV at 300K[49].

The bandgap of III-nitrides changes as a function of temperature and can be expressed using Varshni's law[50]:

$$E_g(T) = E_g(T = 0) - \frac{\alpha T^2}{T+\beta} \qquad (2.2)$$

where α and β are empirical parameters called Varshni parameters; values of which can be adjusted depending on the semiconductor (see table 2.2).

Table 2.2. Bandgap energies E_g and Varshni parameters α and β for group-III nitrides[49,51]

Parameters	GaN	AlN	InN
Eg [eV], (T = 1.6 K)	3.505	6.1	0.7
Eg [eV], (T = 300 K)	3.42	6.0	0.6
α [meV/K]	0.914	2.63	0.414
β [K]	825	2082	154

As mentioned earlier, it is possible to grow ternary compounds such as InGaN and AlGaN. By adjusting the ratio of Ga:In or Ga:Al, the bandgap of the compound can be tuned. In the case of the ternary compound InGaN, the fractional composition is written as $In_xGa_{1-x}N$, where *x* is the

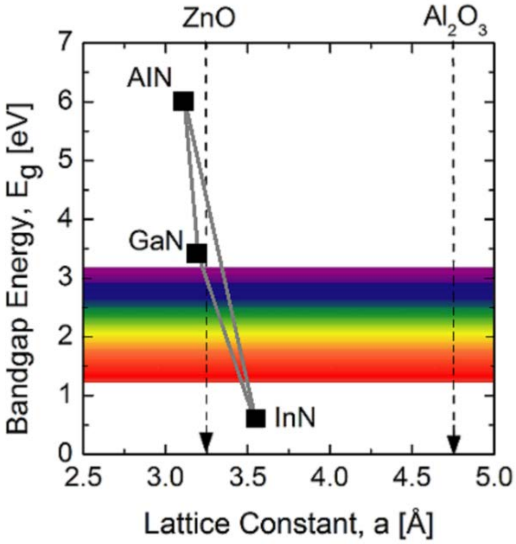

Figure 2.5. Bandgap Energies of group III-nitride binary alloys as a function of lattice parameter, a. The solid black line represents the range of bandgap of the ternary alloys depending on composition. Lattice constants of the Al2O3 and ZnO substrates used for the growth of samples in this study is also shown.

Indium fraction of the alloy. The lattice parameter as expressed by equation 1.3 is a linear superposition of the compounds; however, the bandgap is not linear in the In fraction used. Generally, for an unstrained ternary alloy, the dependence of bandgap on the composition can be calculated with following expression[49]:

$$E_g(In_{(x)}Ga_{(1-x)}N = xE_g(InN) + (1-x)E_g(GaN) - bx(1-x) \tag{2.3}$$

The parameter, *b*, is the bowing parameter which accounts for the deviation from a linear relationship between two binary points. The bowing parameter is dependent on the quality, composition of elements and the growth methods. However, the bowing parameter of *b* = 1.43 eV[49] fits well in the entire composition range affecting the bandgap of InGaN.

2.1.5 Strain Effects

The high melting temperature of GaN makes quality GaN growth sophisticated. GaN crystals can be grown 1) from a solution, 2) from vapor phase and 3) epitaxial method[52]. The first two methods result in bulk GaN crystals which must be further processed to be ready for thin film growth of nitrides. Also, achieving high crystalline quality large wafers using the first two methods is difficult. Therefore, epitaxial method, specifically heteroepitaxial method has become the main choice for the growth of GaN and its alloys. Quality GaN crystal growth is achieved in the form of epitaxial layers on a substrate using metal-organic vapor phase epitaxy (MOVPE), Hydride vapor phase epitaxy (HVPE), molecular beam epitaxy (MBE) or metal-organic chemical vapor deposition (MOCVD). Epitaxial growth is mainly determined by the diffusion of the chemical species at the growth surface. The common substrates used for the growth of GaN are sapphire (Al_2O_3), silicon carbide (SiC) and silicon (Si). A major problem in the growth of III-nitride layers is the large lattice mismatch and the difference in thermal expansion coefficients between epitaxial layers and substrates. III-nitrides are mostly grown in the direction of c-axis. Lattice and thermal misfits causes strained or relaxed growth in the epitaxial layers as shown in figure 2.6 and can lead to interfacial defects. For instance, the growth of InGaN epi-layer on GaN buffer layer results in pseudomorphic strain in the InGaN layer until a critical thickness is reached, after which it is relaxed introducing threading dislocations. Relaxed growth introduces dislocation defects to accommodate for the lattice mismatch. These dislocations propagate through the epi-layer.

Defects can be classified into planar, linear, point and volume defects. Point defects are created when an atom is missing, misplaced or substituted by an impurity atom. The common defects in III-nitrides are basal-plane stacking faults and the threading dislocations. Basal-plane stacking faults (BSFs) are planar defects that interrupt the regular stacking sequence along c-axis by introducing one or more faulted planes to the stacking rules[53]. The lattice mismatch between various epi-layers or the substrate and the overgrown epi-layer can create misfit dislocations. Misfit dislocations follow the growth direction creating linear defects which propagate to the surface. They are called threading dislocations (TDs)[44].

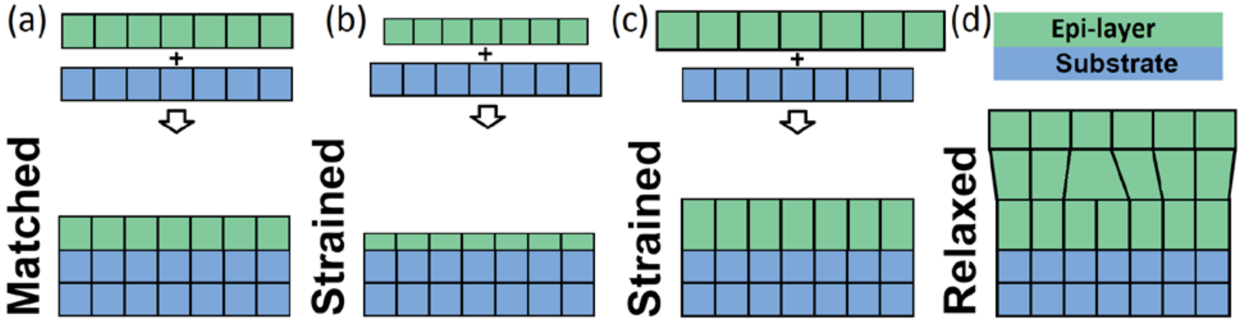

Figure 2.6. Schematic representing lattice mismatch between the substrate (a_s) and the epi-layer (a_e). a) perfectly matched growth ($a_e = a_s$), b) the epi-layer undergoes tensile strain ($a_e < a_s$), b) the epi-layer undergoes compressive strain ($a_e > a_s$) and d) further growth of epi-layers relaxes the strain.

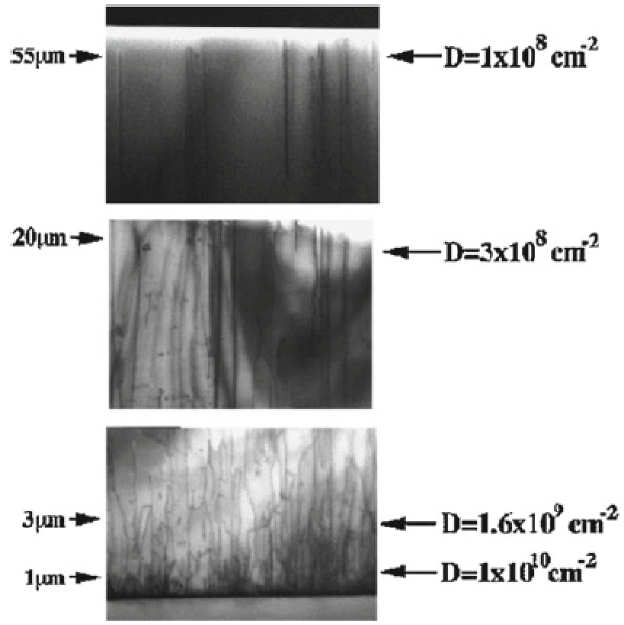

Figure 2.7. Transmission electron microscopy images showing threading dislocation densities present in 55 µm layer thick GaN grown by HVPE[54]. Threading dislocations are reduced in the top layers as many layers are grown compared to the substrate interface.

The defect density of GaN heteroepitaxy layer on sapphire and silicon carbide are typically between 10^8 - 10^{10} cm^{-2} (54,55). TD densities reduce further away from the interface as depicted in figure 2.7. The dislocation densities can be decreased to 5x 10^8 - 10^{10} cm^{-2} using epitaxial lateral overgrowth (ELOG) process[56]. To compensate for the mismatch between III-nitride layers and the substrate, usually an epi-layer of AlN[57] is grown on the substrate which is either directly used or a GaN buffer layer is introduced to decrease the defects. Formation of defects in the crystal introduces non-radiative recombination centers[58] that creates intermediate energy states in the forbidden band. As a result, carrier lifetimes are reduced decreasing the emission efficiency.

2.1.6 Growth Techniques to Reduce Defects In III-Nitrides

The quest for reducing threading dislocations was accompanied by significant efforts by many researchers and resulted in the development of many techniques. Most of these techniques are based on lateral growth. The principle of epitaxial layer overgrowth (ELOG) is to grow an initial buffer layer, use a patterned mask to cover part of the substrate which blocks the dislocations beneath from propagating vertically, which aids in the subsequent growth of layers through unmasked regions with reduced density of dislocations as illustrated in figure 2.8. This is the standard one step ELOG process. The facet assisted ELO redirects the threading dislocations by bending them such that they do not propagate through the entire active layer.

2.1.6.1 Epitaxial Layer Over-Growth

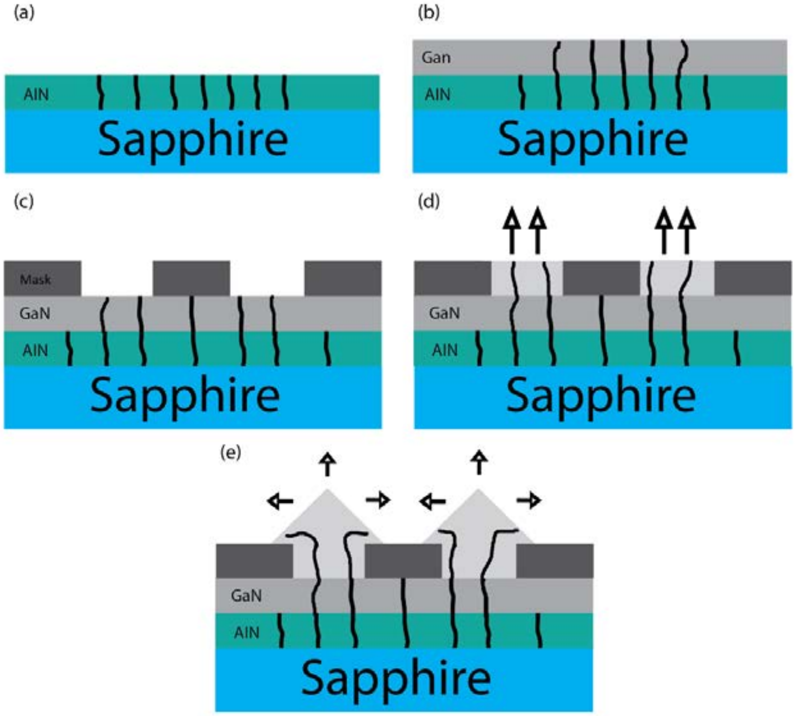

Figure 2.8. Schematic representation of ELOG process of GaN growth. a) AIN buffer layer growth on sapphire substrate to reduce lattice mismatch, b) GaN buffer layer growth, c) Patterned mask to prevent the threading dislocations (black curves), d) d) GaN growth resumed where mask openings act as buffer regions, and e) Growth proceeds normal to the buffer surface and parallel to the buffer surface to create epi-layers. Threading dislocation bends and propagates laterally before it comes to a halt.

In ELO, a dielectric mask (either SiO_2 or Si_3N_4) is deposited atop of GaN buffer layer with patterned openings/windows[13,59]. When GaN growth is resumed under optimized growth conditions, these aperture sites where GaN buffer layer is exposed acts as nucleation sites and allows for the continued growth of the GaN. No adatoms are deposited on the masked area. Once the GaN layer fills the unmasked area, the growth continues both laterally and vertically over the masked areas. The lateral growth can be accelerated by taking advantage of the growth anisotropy; growth rates differ on different crystallographic directions as well as the mask to window area ratio. The vertically grown regions coalesce to form epi-layers with smooth surfaces. Significant reduction in threading dislocation density is obtained in the epi-layer above the masked areas[60].

2.1.6.2 Selective Area Epitaxy

Selective area epitaxy, an epitaxial lateral overgrowth process (SA-ELO) based on selective area growth (SAG) is a controlled way of depositing material in a well-defined area on a substrate using MOCVD or MOVPE. Selective deposition is achieved by the use of either silicon-nitride (SiN) or silicon-oxide (SiO) dielectric mask with patterned openings. Patterns are generated in the mask using standard lithography and etching procedures. Under ideal growth conditions, the reactive precursors arriving from the gas phase to the mask surface will not crystallize on the masked area. This creates gradients in the adatom concentrations over the substrate, forcing the adatoms to diffuse to the mask openings resulting in an enhancement in the growth rate at the openings, where vertical growth happens to the fill the window opening. After the windows are filled, growth continues both laterally and vertically over the masked area. The diffusion of adatoms consists of three phases: vertical vapor phase diffusion, lateral vapor phase diffusion and surface migration from the mask region. The shape of the crystal is determined by the surface energy at thermal equilibrium conditions. In the growth of (0001) oriented GaN pyramids, the

$\{1\bar{1}01\}$ facets appear in hydrogen rich conditions. The main difference between the conventional ELO growth and SA-ELO growth is that the growth can be controlled by controlling growth conditions and the ratio between the mask and window areas (fill factor), which locally determines the distribution of the growth species. Controlling growth kinetics results in the coalescence of the vertical regions of the overgrown layer to form a smooth surface. The asymmetry of the GaN wurtzite crystal leads to anisotropy of free surface energy in GaN leading to different growth rates along different crystal directions[61]. It determines the fabrication of a wide variety of shapes and sizes of GaN structures. Success in selective area growth depends on growth conditions, specifically temperature[13], pressure[62], and molar fraction of the reactive species[63]. SA-ELO was utilized to fabricate GaN micropyramids studied in chapter 3. An extension of SA-ELO was used to selectively grow ZnO and subsequently InGaN/GaN tubes on the top of GaN micro-pyramids; the structures studied in chapters 4 and 5, respectively.

2.1.7 Polarization and Its Effects

III-nitride crystals are known for the existence of polarization fields due to the anisotropy and asymmetry of the wurtzite lattice. Polarization in III-nitrides can be divided into spontaneous and piezoelectric polarization. Electrically negative nitrogen atoms and positive metal atoms owing to the asymmetry of the crystal are offset from each other forming an electric dipole and forms a charge distribution in the c-axis direction. This leads to a macroscopic spontaneous polarization, $\vec{\boldsymbol{P}}_{\text{sp}}$ in the material resulting in an intrinsic electric field. Also, spontaneous polarization depends on the lattice parameters; especially, u. Theoretical values of $\vec{\boldsymbol{P}}_{\text{sp}}$ in III-nitride materials are listed in table 2.3. Negative sign denotes that the spontaneous polarizations are in [0001] direction.

Table 2.3. Spontaneous polarization parameters for Group III-nitride binary alloys[64]

Parameter	GaN	AlN	InN
$\vec{\boldsymbol{P}}_{\mathrm{sp}}$ [C/cm^2]	-0.029	-0.081	-0.032

During crystal growth, lattice mismatch between substrate or epi-layers can modify the position of atoms resulting in mechanical deformation of the crystal due to induced strain, thus changing the charge distribution in the strained layers. This leads to piezoelectric polarization, $\vec{\boldsymbol{P}}_{\mathrm{pz}}$. The relationship between piezoelectric polarization and strain in wurtzite III-nitrides is given by the following equation[65]:

$$\begin{pmatrix} P_x \\ P_y \\ P_z \end{pmatrix} = \begin{pmatrix} 0 & 0 & 0 & 0 & e_{15} & 0 \\ 0 & 0 & 0 & e_{15} & 0 & 0 \\ e_{31} & e_{31} & e_{33} & 0 & 0 & 0 \end{pmatrix} \cdot \begin{pmatrix} \epsilon_{xx} \\ \epsilon_{yy} \\ \epsilon_{zz} \\ \epsilon_{yz} \\ \epsilon_{zx} \\ \epsilon_{xy} \end{pmatrix} \qquad (2.4)$$

where P_i, e_{ij} and $\boldsymbol{\epsilon}_{ij}$ are the piezoelectric polarization, the piezoelectric coefficients of the material and strain in the strained layer, respectively. Here, z direction represents the axis parallel to the [0001] axis. The strain elements in a wurtzite structure are:

$$\epsilon_{xx} = \epsilon_{yy} = \frac{a_s - a_e}{a_e}$$

$$\epsilon_{zz} = \frac{c_s - c_e}{c_e} = -\frac{2C_{13}}{C_{33}} \cdot \epsilon_{xx}$$

$$\epsilon_{yz} = \epsilon_{zx} = \epsilon_{xy} = 0 \qquad (2.5)$$

where a_e and a_s are the free-standing a-axis lattice constants of the epitaxial layer and the substrate, and C_{ij} is the elastic stiffness constant for the epitaxial layer, respectively. The epi-layer is under biaxial compression if a_e is greater than a_s, and vice versa. In wurtzite crystals, for crystal growth in c-direction (z-axis), the strain is in the x-y plane, which is perpendicular to the c-axis.

Therefore, $\boldsymbol{\epsilon_{xx}} = \boldsymbol{\epsilon_{yy}}$ gives in-plane strain, $\boldsymbol{\epsilon_{\perp}}$ and $\boldsymbol{\epsilon_{zz}}$ gives out-of-plane strain, $\boldsymbol{\epsilon_{\parallel}}$ values. Theoretical values of piezo electric and elastic constants are listed in table 2.4.

Table 2.4. Piezoelectric co-efficient and elastic constants of wurtzite group III-nitride binary alloys

Parameters	GaN	AlN	InN
$\boldsymbol{e_{15}}$ [C/m^2]	-0.3[66]	-0.48[66]	-
$\boldsymbol{e_{31}}$ [C/m^2]	-0.49[64]	-0.60[64]	0.57[64]
$\boldsymbol{e_{33}}$ [C/m^2]	0.73[64]	1.46[64]	0.97[64]
$\boldsymbol{C_{13}}$ [GPa]	68[49]	94[49]	70[49]
$\boldsymbol{C_{33}}$ [GPa]	354[49]	377[49]	205[49]

The electric field due to piezoelectric effect along [0001] direction in the strained layer is given by[65]

$$E_z = -\left(\frac{P_z}{\varepsilon_r * \varepsilon_0}\right) \tag{2.6}$$

where $\boldsymbol{\varepsilon_r}$ and $\boldsymbol{\varepsilon_0}$ are the dielectric constant of the material and permittivity of free space. The overall polarization in the crystal is given by the vector sum of the spontaneous and piezoelectric polarizations given by

$$\vec{P} = \vec{P}_{\mathrm{sp}} + \vec{P}_{\mathrm{pz}} \tag{2.7}$$

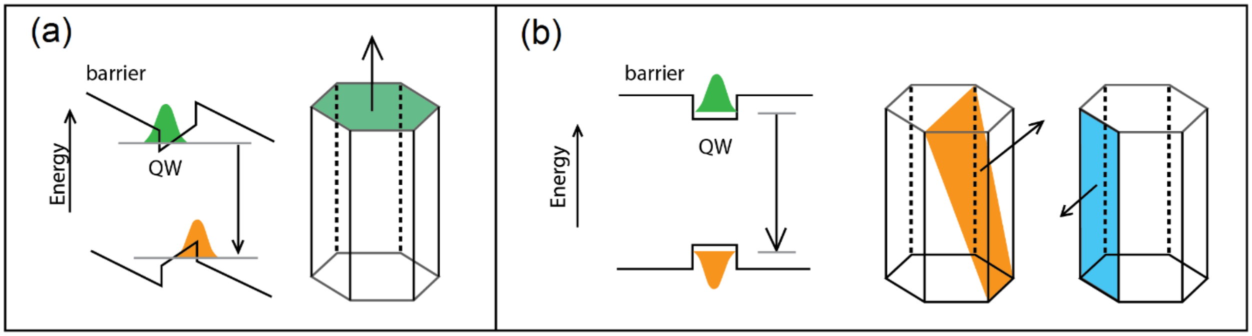

Figure 2.9. Band gap and wave functions a) unstrained; no electric field and b) strained; under the presence of intrinsic electric fields. Band bending as shown in (b) reduces the energy levels and the electron-hole wave functions are separated. Emission energy shifts to the lower side of the spectrum.

In the case of InGaN/GaN multiple quantum wells, InGaN layers on top of GaN undergo compressive strain due to the larger lattice constant InN. This results in discontinuities of the polarization vector at interfaces leading to charge accumulation, which in turn creates internal electrostatic fields, when grown in the direction of polar plane. Piezo electric field have a direct influence on the bandgap of hetero-structures. The strain induced electric field tilts the conduction and valence bands within the well, resulting in spatial separation of bound electrons and holes in opposite directions (see figure 2.9). This reduces the overlap between the wavefunctions which results in reduced oscillator strength thereby reducing the radiative recombination rate[67]. This effect is known as quantum confined Stark effect (QCSE)[68]. QCSE makes the polar III-Nitrides less favorable for light generation in device applications including light emitting diodes and laser diodes. Therefore, it is highly desired to obtain GaN epitaxy on other planes of its unit cell[11,69–71] (see figure 2.3), where there is no polarization discontinuity in quantum well structures. However, achieving this is technically challenging.

2.1.8 Polar to Nonpolar

One of the hot research topic in the GaN optoelectronics field is the development of nonpolar and semipolar nitrides. Currently, commercial products; for example, light emitters based on III-nitride alloys are grown on the polar plane. A major physical problem hindering the advances in nitride emitters made of hetero-structures and QWs is the presence of large electrostatic fields within the active layers induced by spontaneous and piezoelectric polarization resulting in a reduction of the radiative recombination efficiencies and a redshift in the emission wavelength. This redshift is caused by the QCSE effect as discussed in previous section. Second issue is the inefficient performance of LEDs and LDs based on III-nitrides in the green region compared to their blue counter parts[14]. This arises from the fact that longer wavelength emitting devices based on InGaN requires high In content. However, In content exceeding 10% encounters large composition gradients in the active layer due to the miscibility gap in the phase diagram of InGaN[72]. Third problem is that QCSE limits the thickness of the QWs used in light emitters reducing output light efficiency. This is a result of the decrease in total density of states available in the thin single QW. A natural solution to this problem would be increase the number of QWs; however, composition and thickness fluctuations can cause inhomogeneous broadening of the QW absorption. Presence of QCSE becomes highly problematic because it amplifies the worse effects in MQWs.

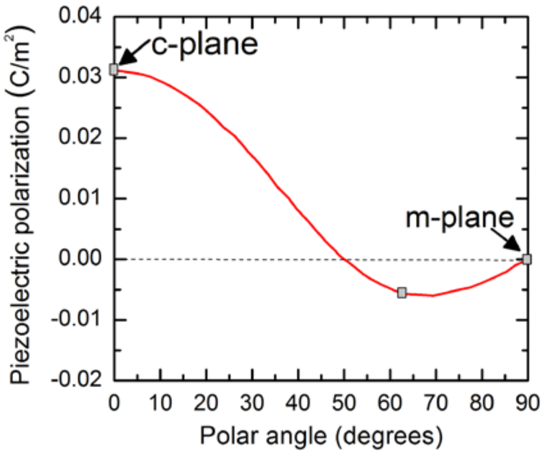

Figure 2.10. Estimated piezoelectric polarization of an In$_x$Ga$_{1-x}$N quantum between relaxed GaN barriers. Red line represents the polarization perpendicular to the growth plane. Data extracted from reference 31.

To overcome these problems, nitride hetero-structures and QWs need to be grown along crystallographic directions where the piezoelectric field is zero or negligible[65]. The growth in nonpolar and semipolar orientations result in vanishing and reduced QCSE[69,49]. Crystal planes perpendicular to the c-plane are referred to as nonpolar planes; a-plane $\{11\bar{2}0\}$ and m-plane $\{10\bar{1}0\}$ shows completely vanishing internal fields (see figure 2.10). Alternatively, for facet orientations between these planes; the so-called inclined planes or semi-polar planes such as $\{10\bar{1}\bar{1}\}$ and $\{1\bar{1}01\}$ show reduced fields. The hetero-structures grown on non-polar planes do not show tilting of bandgap or spatial separation of carrier wavefunctions as shown in figure 2.9 b. The pioneering work in this field by Waltereit et al[73] demonstrated that the epitaxial growth of GaN/ AlGaN in the non-polar direction results in structures free of electrostatic fields. The history and timelines of initial to progressive work in the non- and semi-polar planar growth are elegantly reviewed by T. Pasakova[11]. Initial attempts to realize this consisted of cutting crystals in the direction of a- or m- planes from polar substrates and subsequent planar growth of nitride layers using epitaxy[74]. Also, growth of nitride layers was attempted on different planes of sapphire substrate as well as on other substrates. However, epitaxy of nitrides on these orientations resulted in high densities of basal plane faults and threading dislocations[11,75]. Although high quality free standing nonpolar and semipolar GaN templates are available, commercial growth of these hetero-structures is hindered by the small wafer size and high cost[69]. Besides the disadvantages, sufficient motivation still exists to find a compromise between reduced defect density and intrinsic electric fields for enhanced light output.

One of the parallel approach to resolve the issues in polar nitrides was the growth of micro- and nano- structures of GaN which can be used as a template for the growth of hetero-structures or QWs. These structures, owing to the small area of contact with the template reduced the strain build up from lattice[76] and TEC misfits. The high surface-to-volume ratio facilitates the relaxation of strain without creating defects in the crystal[77]. Micro- and nano-structures grown in the polar direction demonstrated reduction in polarization[73], increase in recombination efficiency[78,79]. Also, reduction in strain allows higher In incorporation in the InGaN MQWs, which allows the possibility of green and red emitters. This progress stemmed the growth of nonpolar and semi polar micro/nano GaN templates for subsequent growth of ternary alloys of GaN. QWs on these facets have reduced number of stacking faults compared to the nonpolar hetero-epitaxial thin films[80].

2.2 Zinc Oxide

Zinc Oxide (ZnO) is a II-VI semiconductor compound which possess wurtzite crystal symmetry similar to GaN. It has a direct wide bandgap with an energy of $E_g \approx 3.37$ eV at 300 K[81]. ZnO has great potential for photonic applications especially UV-light emitters. The central advantage of ZnO as a light emitter is its large exciton binding energy (≈ 60 meV >> thermal energy (27meV)), which allows efficient excitonic recombination even at room temperature. Unlike GaN, growth techniques of ZnO are less sophisticated and therefore ZnO is available as large bulk crystals. However, p-type doping of ZnO is difficult to achieve which has hindered the practical development of ZnO based semiconductor devices. Nevertheless, it has been shown that ZnO can be used as a substrate to grow GaN owing to the reduced TEC mismatch and close match of their lattice parameters[81,82]. One of the samples studied in this dissertation; ZnO submicron rods (SMRs), is used as a template to grow InGaN/GaN submicron tubes with multiple quantum wells. ZnO have high second order susceptibility co-efficients and has been demonstrated to be an efficient NLO emitter. Chapter 4 discusses NLO generation and its control from ZnO SMRs.

2.3 Optics: Light Matter Interaction

Optics is a term associated with light which plays a significant role in our everyday life. Light brings visual information to us through interactions with matter. Light, the study of light, the study using light and the equipment that studies and uses light all fall under the mighty branch of optics. Advances in science in general and specifically in optics has enabled the observation of fascinating phenomena not directly accessible to human senses. Studying optical interactions with matter allows you to advance knowledge about the matter; whether it be a piece of glass or a biological cell. Optics can be classified into two major realms; linear and nonlinear. Linear optics involves the interaction of weak light with matter, whereas nonlinear optics involves interaction of strong light with matter. The difference between the two interactions is the manifestation of the induced polarization in the interacting medium as discussed here. The effect of linear interactions is a dispersion relation and the light propagation in the matter is slower than in a vacuum which gives rise to refractive index of the matter. Maxwell approximated that the induced polarization was independent of the strength of the applied field making it linearly proportional to the field amplitude. In nonlinear media, the response of the induced dipoles is nonlinear causing nonlinear oscillation of dipoles. The time varying polarization act as a source to produce new components of the incident field. Therefore, they radiate at frequencies different than the frequencies of the applied light waves, leading to the generation of new frequencies. In the optical regime, this means generation of different color(s) of light.

2.3.1 Linear Interaction

Linear light-matter interaction can be described by the classical Lorentz model of harmonic oscillator consisting of a single atom with an electron and a nucleus. The electric field of the light induces oscillating dipoles in the matter in which it propagates; in other words, the electron oscillates about its equilibrium position. The induced dipoles radiate a secondary light wave at their oscillation frequencies. In linear media, the frequencies of the applied light and radiated light are the same; however, phases differ. The equation of motion of the electron with mass m, and charge e oscillating harmonically at its natural frequency ω_0 can be given by:

$$\frac{d^2r}{dt^2} + 2\gamma\frac{dr}{dt} + \omega_0^2 r = -\frac{e}{m}E \qquad (2.8)$$

where r is the displacement of the electron from its equilibrium position, γ is a damping constant and E is the applied electric field. The steady state solution to equation 1 with an electric field in the form $\mathcal{E}\cos(\omega t - \varphi)$ is

$$r = -\frac{e}{m}\, E(\omega)\frac{e^{-i\omega t}}{{\omega_0}^2 - 2i\gamma\omega - \omega^2} \qquad (2.9)$$

inducing a linear polarization of $P = -N\epsilon_0 er$, where N is the electron density in the medium and ϵ_0 is the permittivity of free space. Therefore, linear polarization can be written as:

$$P = \epsilon_0\chi^{(1)}(\omega)E(\omega)e^{i\omega t} \qquad (2.10)$$

where $\chi^{(1)}$ is the linear susceptibility of the medium.

2.3.2 Nonlinear Interaction

When the applied field strength is comparable in size to the inter-atomic electric field within the medium the linear polarization response is no longer sufficient. A typical threshold for this transition is ~ 10^6 W/cm^2, which can be easily obtained by pulsed lasers. The nonlinear optical response of a medium to applied field can be described by expressing the induced polarization as a power series expansion of the electric field[83],

$$\tilde{P}(t) = \epsilon_0[\chi^{(1)}\tilde{E}(t) + \chi^{(2)}\tilde{E}^2(t) + \chi^{(3)}\tilde{E}^3(t) + \cdots]$$

$$= \tilde{P}^{(1)}(t) + \tilde{P}^{(2)}(t) + \tilde{P}^{(3)}(t) + \cdots$$

$$= \tilde{P}_L + \tilde{P}_{NL} \qquad (2.11)$$

where $\chi^{(1)}$ is the linear susceptibility, $\chi^{(2)}$ and $\chi^{(3)}$ are the second and third order nonlinear susceptibilities, respectively and $\tilde{P}^{(1)}(t)$ and $\tilde{P}_L$ are referred to as linear polarization, $\tilde{P}^{(2)}(t)$, $\tilde{P}^{(3)}(t)$ and $\tilde{P}_{NL}$ are referred to second order, third order and nonlinear polarization, respectively. The higher order polarizations constitute nonlinear polarization. Relationships given by equation (3) and (4) assume that the polarization at time t depends only on the instantaneous value of the electric field strength, which implies that the medium must be lossless and dispersion less. If we consider $\tilde{P}(t)$ and $\tilde{E}(t)$ to be vector quantities, susceptibility terms $\chi^{(n)}$ becomes (n+1)th rank tensors. To represent second order susceptibility, theorists use $\chi^{(2)}$-tensor; whereas, experimentalists tend to use *d*-tensor. Both conventions can be related by[84] $d = \chi^{(2)}/2$. The physical processes that occur as a result of second order nonlinearity is different than those occur as a result of third order nonlinearity and is also dependent on the symmetry of the medium.

The wave equation describing the propagation of light in a non-absorbing, non-conducting dielectric nonlinear media with no free charges inducing electric displacement field, $\tilde{D} = \epsilon_0 \tilde{E} + \tilde{P} = \epsilon_0(1 + \chi^{(1)})\tilde{E} + \tilde{P}_{NL}$ can be derived from Maxwell's equations as,

$$\nabla^2 \tilde{E} - \frac{n^2}{c^2}\frac{\partial^2 \tilde{E}}{\partial t^2} = \frac{1}{\epsilon_0 c^2}\frac{\partial^2 \tilde{P}_{NL}}{\partial t^2} \qquad (2.12)$$

where n is the new refractive index of the material and c is the speed of light in vacuum. The nonlinear polarization, $\tilde{P}_{NL}$ drives the electric field $\tilde{E}$ resulting in the generation of new electric fields.

For a dispersive medium, each frequency component of the field must be considered separately[83] and the wave equation becomes:

$$\nabla^2 \tilde{E}_n - \epsilon^{(1)} \frac{\omega_n^2}{c^2} \frac{\partial^2 \tilde{E}_n}{\partial t} = \frac{1}{\epsilon_0 c^2} \frac{\partial^2 \tilde{P}_n^{NL}}{\partial t^2} \qquad (2.13)$$

Equation (2.13) expresses that whenever $\partial^2 \tilde{P}_n^{NL} / \partial t^2$ is nonzero, charges are being accelerated, and accelerated charges generate electromagnetic radiation.

This dissertation involves both second order and third order nonlinear processes. The second order and third order nonlinearities involved in this work are the second harmonic generation and the two-photon absorption processes.

2.3.3 Second Harmonic Generation

Second harmonic generation is a second order process in which the applied field of frequency ω is converted into a new field of frequency 2ω. When a sufficiently intense optical field of fundamental frequency ω interacts with a nonlinear material, the second order susceptibility, $\chi^{(2)}$ is non-zero. The nonlinear polarization induced is

$$\tilde{P}^{(2)}(t) = \epsilon_0 \chi^{(2)} \tilde{E}^2(t) \qquad (2.14)$$

If the incident field can be represented as a monochromatic light wave with a frequency of ω,

$$\tilde{E}(t) = E e^{-i\omega t} + c.c. \qquad (2.15)$$

the second order nonlinear polarization in equation (7) becomes,

$$\tilde{P}^{(2)}(t) = 2\epsilon_0 \chi^{(2)} E E^* + \epsilon_0 \chi^{(2)} E^2 e^{-i2\omega t} + c.c. \qquad (2.16)$$

where c.c. stands for complex conjugate. Equation (2.16) describes that second order polarization consists of a contribution at zero frequency (the first term) and a contribution at frequency 2ω (the second term). The first term creates a dc field responsible for optical rectification and the second term leads to the generation of radiation at second harmonic frequency. The process of SHG is illustrated in figure 2.11.

Second harmonic generation can occur in the bulk of noncentrosymmetric materials as well as at the surface of centrosymmetric materials, where the surface interface provides the inversion symmetry. However, it cannot occur in the bulk of centrosymmetric materials.

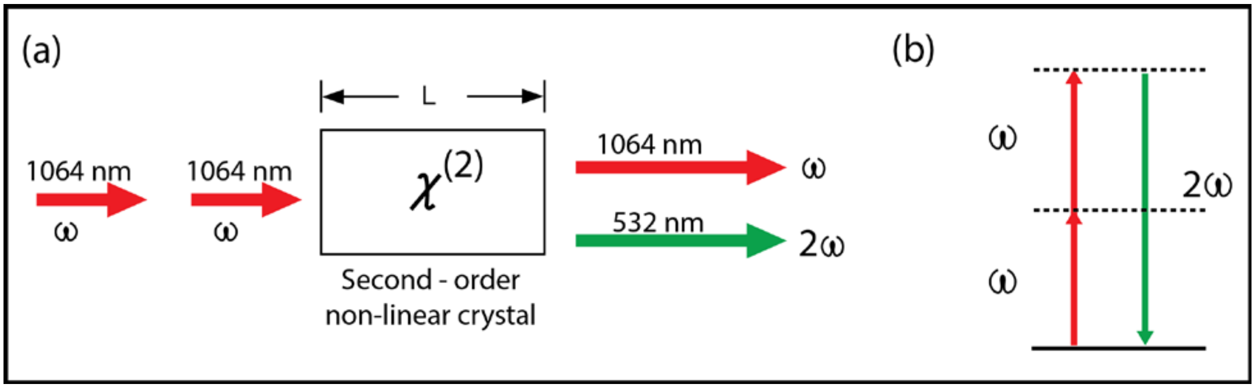

Figure 2.11. The process of second harmonic generation. (a) shows the geometry of SHG, (b) represents the energy level diagram describing SHG. The dashed lines represent intermediate levels. L is the interaction length of the crystal.

2.3.4 Wave Equation Description of SHG

SHG process can be viewed as a three wave mixing process, where three interacting optical waves satisfy the energy conservation condition, $\omega_2 = 2\omega_1$. Assuming propagation in +z direction, the fundamental and second harmonic waves can be described to be plane waves of the form as:

$$\tilde{E}_i(z,t) = E_i(z)\, e^{i(k_i z - \omega_i t)} + c.c. = A_i(z)\, e^{i(k_i z - \omega_i t)} + c.c. \qquad (2.17)$$

where *i = 1* represent the fundamental fields and *i=2* represent the SHG field. Here $\tilde{E}_i(z)$ represents the complex amplitude and $A_i(z)$ represents the spatially slowly varying amplitude of the waves, which is constant in a linear medium. The nonlinear polarization in the wave equation (2.13) can be represented in the form:

$$\tilde{P}_2(z,t) = P_2(z)\, e^{i(2k_1 z - 2\omega_2 t)} + c.c \qquad (2.18)$$

where $P_2 = P(\omega_2) = \epsilon_0 \chi^{(2)} E_1^2 = 2\epsilon_0 d_{eff} A_1^2 e^{2ik_1 z}$ represents the amplitude of the nonlinear polarization.

Substituting equations (2.17) and (2.18) in (2.13) and simplifying

$$\frac{dA_2}{dz} = \frac{i\omega_2}{n_2 c} d_{eff} A_1^2 e^{i(2k_1 - k_2)z} \qquad (2.19)$$

Equation (2.19) expresses that two fundamental waves interact with the nonlinear material to generate an additional wave with double the frequency. The second harmonic wave generated becomes stronger as it propagates through the material. During the simplification process, higher order derivatives of A_2 is omitted assuming that A_2 is much smaller. Under the assumption that A_1 is not appreciably modified by the nonlinear interaction, A_1 is considered to be a constant to solve equation (2.19) by direct integration in the limits of z = 0 to L, where L is the length of the nonlinear material. Thus the amplitude of the SH field after propagation through a distance L is:

$$A_2(L) = \frac{i\omega_2}{n_2 c} d_{eff} A_1^2 \left(\frac{e^{i\Delta k} - 1}{i\Delta k L} \right) \qquad (2.20)$$

where,

$$\Delta k = 2k_1 - k_2 \qquad (2.21)$$

is the wave vector or momentum mismatch between the fundamental and SH fields.

Since the intensity is related to field strength according to $I = 2n\epsilon_0 c|A|^2$, the intensity of generated radiation is given by:

$$I_2(L) = \frac{8 d_{eff}^2 \omega_2^2}{\epsilon_0 c^2} \frac{I_1^2}{n_1^2 n_2} L^2 sinc^2\left(\frac{\Delta k L}{2}\right) \qquad (2.22)$$

where,

$$sinc\left(\frac{\Delta kL}{2}\right) \equiv \frac{\sin\left(\frac{\Delta kL}{2}\right)}{\left(\frac{\Delta kL}{2}\right)} \qquad (2.23)$$

SHG is most efficient when the perfect phase matching condition, $\Delta k = 0$ is achieved. When perfect phase matching is fulfilled, the *sinc* function in equation (2.22) becomes unity, and thus the intensity of second harmonic radiation scales with the square of the length L of the interaction region. When equation (2.21) is satisfied, the individual dipoles that constitute the nonlinear material are in phase with each other such that the field emitted is added coherently in the forward direction. Equation (2.22) also expresses that when $L \gg 1/\Delta k$, the intensity of SHG decreases, because at these lengths the SH wave is out of phase with the polarization wave restricting sufficient energy transfer between the fundamental and SH waves. It can be seen from equation (2.22) that the SH intensity oscillates as a function of *L* (see figure 2.12) with a period:

$$L_c = \frac{\pi}{|\Delta k|} = \frac{\lambda_\omega}{4|n_\omega - n_{2\omega}\ |} \qquad (2.24)$$

where n_ω and $n_{2\omega}$ are the values of refractive indices at the applied and SH frequencies, and λ_ω is the wavelength of the applied field. This characteristic length, *L_c* of the nonlinear crystal where coherent buildup of SH field occurs and reaches maximum value is called the coherence length.

To achieve phase matching condition, $n(\omega)$ must be equal to $n(2\omega)$ according to equation (2.21). However, material dispersion causes the refractive indices to be scaled differently as a function of frequency. In the anomalous dispersion region, which is close to the linear absorption peak, it is possible to achieve the phase matching condition[83] as there may exist two frequencies for which the refractive index of the medium is same. The phase matching condition is often fulfilled by using a birefringent material, which can achieve nearly perfect phase matching. However, not all materials with high second order nonlinearity possess significant birefringence. Another approach is quasi phase matching, which periodically inverts the sign of the second order nonlinear co-efficient in the material at intervals of length equal to multiples of coherence length to compensate for the phase mismatch[85]. See figure 2.12 b for phase matching effects on SH amplitude.

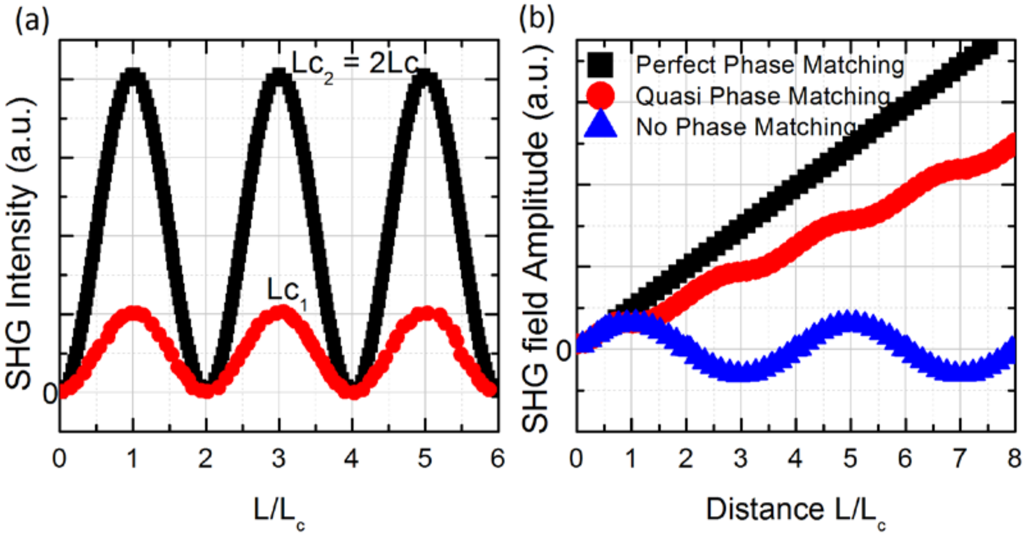

Figure 2.12. Second harmonic intensity as a function of interaction length and the effect of phase matching. a) SH intensity as a function of the length L of the nonlinear material normalized to the coherence length Lc for two values, b) SH field amplitude as a function of interaction length for phase matching techniques.

2.3.5 Second Order Nonlinear Susceptibility

Generalized second order polarization in the frequency domain for three interacting waves of frequencies ω_1, ω_2 and $\omega_3 = \omega_1 + \omega_2$ in a nonlinear material can be expressed as:

$$P_i(\omega_n+\omega_m) = \epsilon_0 \sum_{jk}\sum_{(nm)} \chi_{ijk}^{(2)}(\omega_n+\omega_m,\omega_n,\omega_m)E_j(\omega_n)E_k(\omega_m) \qquad (2.25)$$

where $\chi_{ijk}^{(2)}$ is a third-rank tensor, *i* represents the output field, *j* and *k* represent the input fields. In the case of SHG, *j* and *k* can be permuted under symmetry. The 27 element susceptibility tensor can be reduced to an 18 element matrix, d_{il} by applying symmetric conditions and contracting the indices using the following notation[83]:

$$\begin{array}{lcccccc} jk: & 11 & 22 & 33 & 23=32 & 13=31 & 12=21 \\ l: & 1 & 2 & 3 & 4 & 5 & 6 \end{array} \tag{2.26}$$

By this convention, the nonlinear polarization resulting in SHG in terms of d_{il} can be written as:

$$\begin{bmatrix} P_x(2\omega) \\ P_y(2\omega) \\ P_z(2\omega) \end{bmatrix} = 2\epsilon_0 \begin{bmatrix} d_{11} & d_{12} & d_{13} & d_{14} & d_{15} & d_{16} \\ d_{21} & d_{22} & d_{23} & d_{24} & d_{25} & d_{26} \\ d_{31} & d_{32} & d_{33} & d_{34} & d_{35} & d_{36} \end{bmatrix} \begin{bmatrix} E_x(\omega)^2 \\ E_y(\omega)^2 \\ E_z(\omega)^2 \\ 2E_y(\omega)E_z(\omega) \\ 2E_x(\omega)E_z(\omega) \\ 2E_x(\omega)E_y(\omega) \end{bmatrix} \tag{2.27}$$

The number of independent elements in the tensor d_{il} can be reduced further depending on the crystal structure. Hexagonal crystalline materials with 6mm symmetry like GaN and ZnO are anisotropic and exhibits rotational symmetry about the crystal axis. Therefore, d_{il} for these materials can be reduced to[86]:

$$d_{il} = \begin{bmatrix} 0 & 0 & 0 & 0 & d_{15} & 0 \\ 0 & 0 & 0 & d_{15} & 0 & 0 \\ d_{31} & d_{31} & d_{33} & 0 & 0 & 0 \end{bmatrix} \tag{2.28}$$

2.3.6 Nonlinear Absorption

Two-photon absorption is a nonlinear absorption process which is a manifestation of the third order nonlinear susceptibility of the material which the applied intense field interacts with. In fact, the third order susceptibility is a complex quantity where the real and imaginary parts are responsible for nonlinear refraction and nonlinear absorption, respectively. The nonlinear polarization produced by third order susceptibility is

$$\tilde{P}^{(3)}(t) = \epsilon_0 \chi^{(3)} \tilde{E}^3(t) \tag{2.29}$$

For a monochromatic input field with a frequency ω, equation (2.29) leads to a polarization oscillating at two frequencies; 3ω and ω. The polarization component that oscillates at the fundamental frequency causes an intensity dependent refractive change in the material. The nonlinear refractive index given by $n = n_0 + n_2 I$ results in nonlinear absorption.

The probability of the two-photon absorption can only be induced by intense applied fields; for example, a pulsed laser excitation. Two-photon absorption is a transition from the ground state to an excited state by the simultaneous absorption of two photons from the applied fields (see figure 2.13). The absorption of two-photons is facilitated by intermediate levels that may or may not be stable states in the material system. The two-photon atomic transition rate is given by

$$R = \frac{\sigma^{(2)} I^2}{\hbar\omega} \tag{2.30}$$

where $\sigma^{(2)}$ is the two-photon absorption cross-section and ω is the frequency of the excitation photons. In semiconductors, the probability of a two-photon transition can be expressed as[3]

$$P = \frac{2\pi}{\hbar} \sum_{i,f} \left|W_{if}\right|^2 g(E) \tag{2.31}$$

where $g(E)$ is the density of states and *i* and f are initial and final states. In the dipole approximation, the transition matrix is given by[3]:

$$W_{if} = \frac{e^2}{m^2 c^2} A_1 A_2 \sum_{l} \left(\frac{\langle f|e_1 p|l\rangle\langle l|e_2 p|i\rangle}{E_{li} - \hbar\omega_2} + \frac{\langle f|e_2 p|l\rangle\langle l|e_1 p|i\rangle}{E_{li} - \hbar\omega_1} \right) \tag{2.32}$$

where e_1 and e_2 are polarization vectors of the two applied fields, A_1 and A_2 are the vector potentials at frequencies ω_1 and ω_2, l represents the intermediate states and E_{li} is the energy difference between the initial and intermediate states.

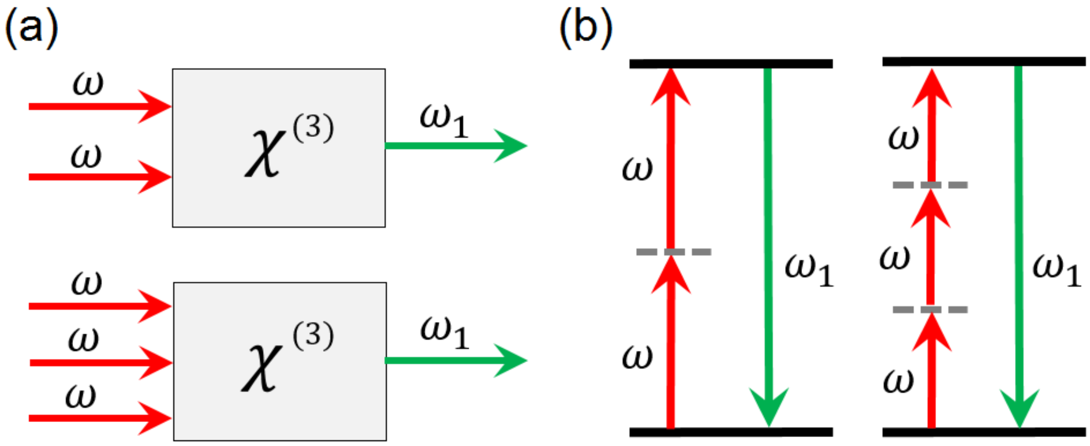

Figure 2.13. Third order nonlinear process resulting in nonlinear absorption. (a) shows the geometries for 2 photon and 3 photon absorption processes, (b) represents the energy level diagram describing resonant multiphoton absorption and multi-photon induced emission. The dashed lines represent intermediate levels.

When more than two photons are involved in the absorption process, it is called a multi-photon absorption process (see figure 2.13 b). The relaxation of excited carriers' results in the emission process is known as two-photon/multi-photon induced luminescence identical to single photon process. Multi-photon absorption process is analogous to single photon absorption; however, the selection rules are different[3]. Third order nonlinearity can occur in both centrosymmetric and noncentrosymmetric materials. In a noncentrosymmetric crystal, exciton states allowed in single photon transition can also be observed in two-photon transition[3]. The color and line width of two- or multi-photon emission peak are determined by the energy differences of the ground and excited states and the density of states; whereas the emission life time is related to the oscillator strength which is typically in the range of nanoseconds. In contrast, the SHG peak characteristics derives from the excitation laser source. SHG peak has a line width of $1/\sqrt{2}$ of the bandwidth of the excitation laser, and has the same temporal values as the applied field[87].

2.4 Photoluminescence in Semiconductors

This section of the chapter provides a brief discussion on the physical origin of photoluminescence mechanisms in semiconductors that are pertinent to GaN and ZnO and this work. These are free and bound excitons, donor-acceptor pairs (DAP), band-acceptor transitions (e-A) and electro-hole plasma as is represented in figure 2.15.

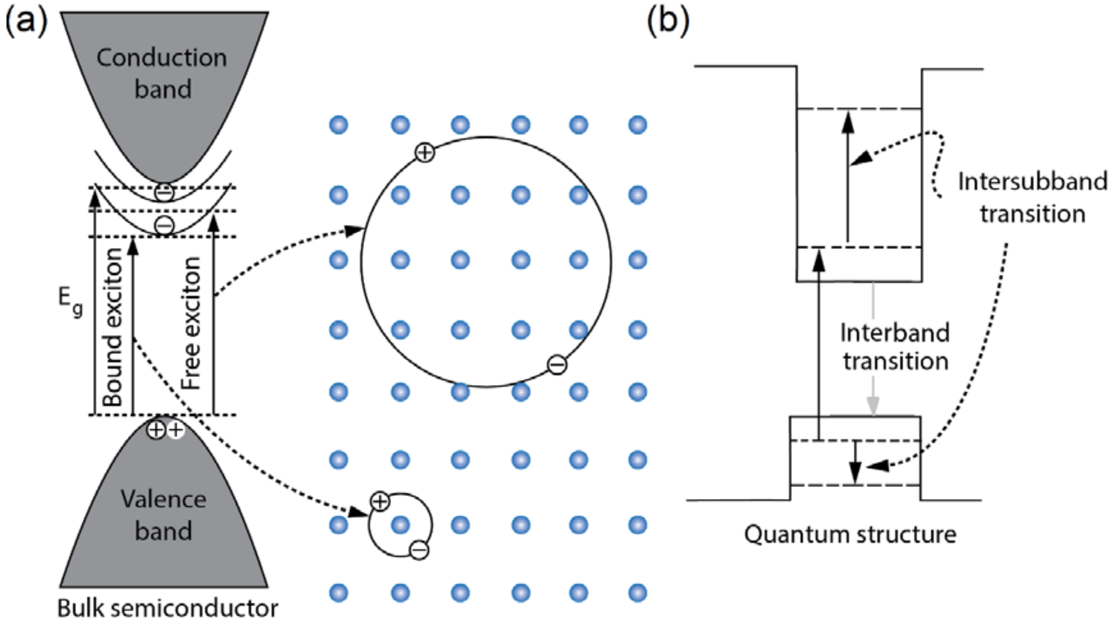

Figure 2.14. Schematic of direct bandgap bulk semiconductor and quantum well structure. (a) Optical bandgap of a bulk semiconductor. Exciton levels in the bandgap is shown along with free and bound exciton configuration in the crystal lattice. (b) Effective bandgap of a single quantum well structure. Transitions between the conduction and valence bands are called interband transitions and transitions between the discrete levels in a conduction band is called intersubband transition, which may occur in QW structures.

Semiconductor materials with a direct bandgap like GaN and ZnO can generate light through the photo-absorption of applied field. During this process, electrons in the valence band absorb photons with an energy equal to or above the bandgap energy, E_g and be excited into the conduction band. This is called inter-band transition or absorption. To restore equilibrium, the excited electrons transit back from the conduction band to the valence band with the release of energy in the form of photons, phonons or collisions. Release of energy of photons is called spontaneous recombination process, whereas release in the form of other forms result in non-radiative recombination process. The energy released is equal to the difference in the energies of states occupied by electrons and holes. This step is called the emission process resulting in photoluminescence and is schematically represented in figure 2.14. Generally, the photoluminescence process is a combination of radiative and non-radiative recombination processes. Non-radiative recombination occurs when the excited electron undergoes some energy loss in the continuum of the conduction band via vibrations to reach the minima of the conduction band. The band-to-band transition in bulk materials is referred to as optical band gap, whereas, in quantum wells it is referred to as effective bandgap.

2.4.1 Band-to-Band Transitions

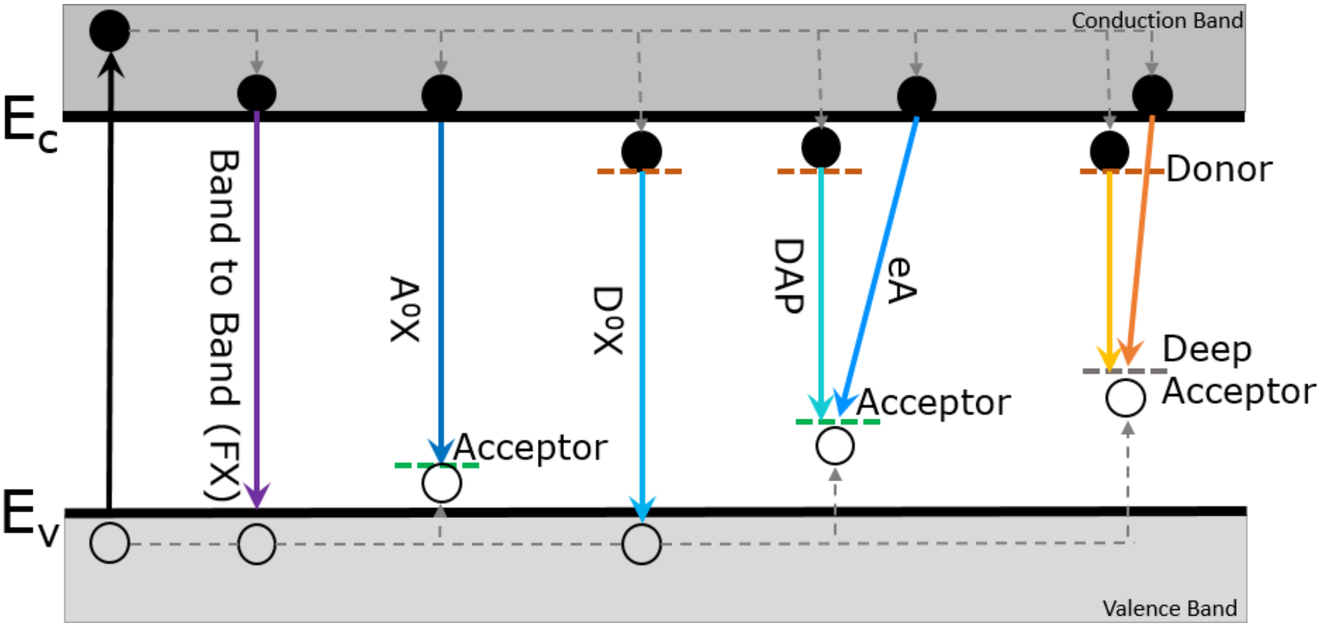

Figure 2.15. Transition processes associated with photluminescence. FX: free excitons, A^0X: acceptor bound excitons, D^0X: Donor bound excitons, DAP: Donor-acceptor pair, eA: free electron-acceptor pair [Figure adapted from reference 10].

Band-to-band transitions consist of the recombination of free electrons and holes. In a perfect semiconductor, electron-hole pairs will thermalize and accumulate at the extrema of conduction and valence band, where they undergo recombination. This increases the probability of recombination process in a direct band gap semiconductor owing to momentum conservation. The lifetime of the recombination process can be expressed as[3]

$$\frac{1}{\tau_{PL}} = \frac{1}{\tau_R} + \frac{1}{\tau_{NR}} \tag{2.32}$$

where τ_{PL} is the total recombination lifetime, τ_R and τ_{NR} are the radiative and nonradiative recombination times.

2.4.2 Excitons

During photo-absorption, the excited electron leaves a positively charged hole behind in the valence band creating an electron-hole pair. When the electron and hole interacts via a Coulomb interaction, they form an exciton. There are two types of excitons; free exciton or Wannier-Mott exciton and bound exciton or Frenkel exciton. As the names suggest, free excitons can move about the crystal lattice undisturbed whereas bound exciton is trapped by an impurity in the crystal lattice. The binding energy of free exciton is smaller than the bound exciton.

The intrinsic transition energy involving a free exciton is given by:

$$\hbar\omega = E_g + E_{kin} - E_x \tag{2.33}$$

where E_g is the bandgap energy, E_x describes the ground state exciton binding energy.

Transitions involving bound excitons emit photons with an energy

$$\hbar\omega = E_g + E_{kin} - E_x - E_{bx} \tag{2.34}$$

where E_{bx} is the binding energy of the bound exciton at the location of impurity.

Semiconductors may contain impurities that can act as donors or acceptors in their crystal lattice. The excitons can be bound to shallow donors, deep donors and structural defects. Depending on the type of impurities, excitons can be bound to a neutral acceptor (A^0) or a neutral donor (D^0) or an ionized donor (D^+) resulting in PL emission called A^0X, D^0X and D^+X transitions respectively.

2.4.3 Free-to-Bound Transitions

Band-to-band transitions are dominant at higher temperatures where all the shallow impurities are ionized. However, at low temperatures; for example, low temperature photoluminescence spectroscopy, carriers are frozen on impurities. When the density of free electrons is smaller than the impurities as in the case of an n-type semiconductor, free electrons can recombine radiatively or nonradiatively with the holes trapped on the acceptors. Transitions involving a free carrier (an electron) and a hole bound to an impurity, are known as free-to-bound transitions. As the acceptor concentration is increased (> 10^{18} cm^{-3}), their wavefunctions tend to overlap as the proximity of the acceptors reduce. This results in broadening of the acceptor levels into an impurity band, which results in the broadening of photoluminescence spectra. When the impurity band is so broad that it overlaps with the valence band, holes are no longer localized on the acceptors and become free carriers. This transformation of carriers from a localized state to a delocalized one is known as a Mott transition[88]. This can result in a redshift called bandgap renormalization.

2.4.4 Donor–Acceptor Pair Transitions

All Semiconductors contain both donors and acceptors, where some of the electrons from the donors are captured by the acceptors forming ionized donors (D^+) and acceptors (A^-) under equilibrium conditions. The electrons and holes generated by optical excitation can then be trapped at the (D^+) and (A^-) sites to produce neutral D^0 and A^0 centers. To establish equilibrium some of the electrons on the neutral donor sites will recombine radiatively with holes on the neutral acceptors. This process is known as a donor–acceptor pair transition (or DAP transition). With increasing temperature, the DAP lines often disappear as the shallow donor state thermally ionizes.

2.4.5 Electron-Hole Plasma

The exciton-exciton interactions are negligible when the optical excitation density is low, as the separation between excitons are large. When the excitation optical density increases, so does the density of the electron-hole pair and hence the exciton-exciton interactions becomes significant and results in many body effects such as screening of exciton resonances. The exciton becomes unbound at an e-h density greater than 10^{18} cm^{-3}. This is called Mott density[89]. At this density, the excitonic collisions result in disassociation of e-h pairs forming electron-hole plasma. The main properties of EHP are broadening of emission spectra and reduction in optical gap thus shifting the emission energy to the lower side of the spectrum.

2.4.6 Quantum Well Emission

Quantum wells are hetero-structures made from at least two different materials using epitaxial growth techniques, where the two materials are deposited alternately such that the material with lower bandgap energy (well) is sandwiched between a material with higher bandgap energy (barrier). When the thickness of the well material is comparable to the de Broglie wavelength of the electrons or holes (quantum well), quantum confinement of electrons occurs resulting in emission at room temperature. Figure 2.16 shows the schematic of an InGaN/GaN quantum wells.

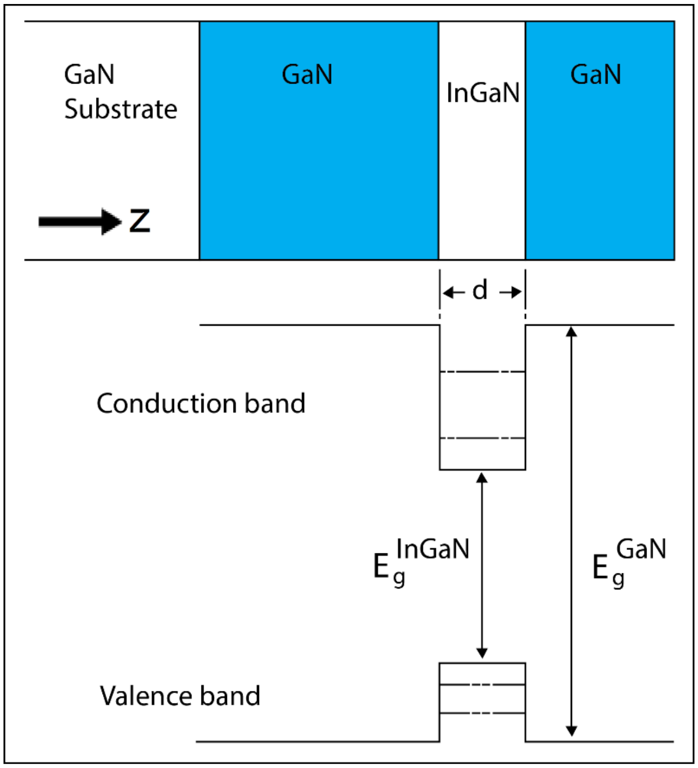

Figure 2.16. Schematic of InGaN/GaN MQW grown in the z direction as directed by the arrow and the corresponding band diagram for the quantum well with thickness d. The dashed lines in the QW represents the discrete energy levels. QWs are made of InGaN and barrier layers are made of GaN.

In this figure, motion of electrons is confined in the z direction by the barrier layers, while they are free to move in x-y plane. Multiple quantum wells (MQWs) have large barrier widths compared to single QW such that the QW is well isolated. The energy of the n^{th} level can be found from solving Schrödinger equation as

$$E_n = \frac{\hbar^2 k_n^2}{2m^*} = \frac{\hbar^2}{2m^*}\left(\frac{n\pi}{d}\right)^2 \qquad (2.35)$$

where n is an integer that gives the quantum number of the state, d is the thickness of the QW and m* is the effective mass of the electron.

2.5 Spectroscopy and Imaging Techniques

2.5.1 Single-Photon Excitation Vs. Multi-Photon Excitation

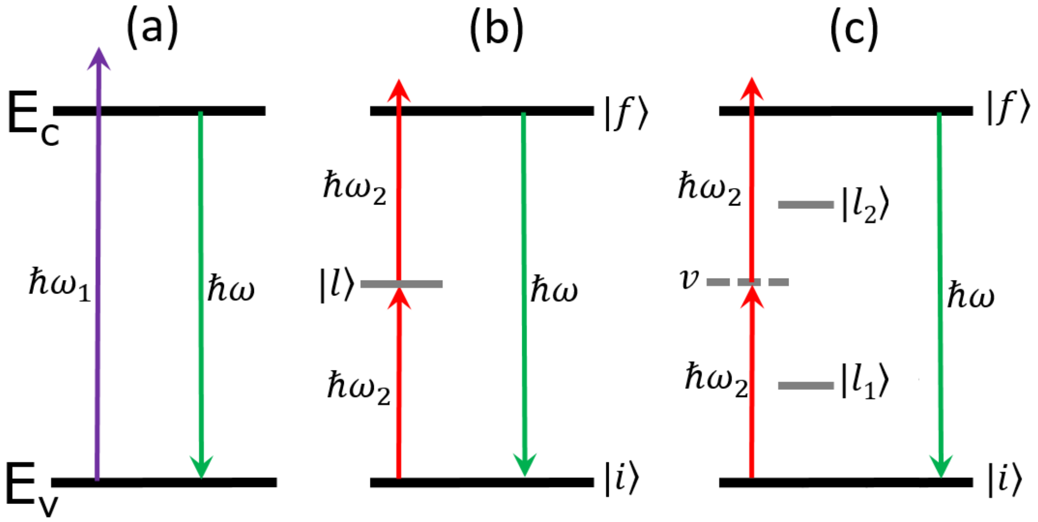

Figure 2.17. Electron transition schemes. (a) Single photon excitation, (b) two-photon excitation via real intermediate state and (c) two-photon excitation via a virtual state. Excitation energies used for single and two-photon are different; however, emission has same energy in all the cases.

Excitation refers to the method that creates carriers in materials. Absorption process due to photo-excitation was described in section 2.1.4, while linear and nonlinear matter interactions were discussed in sections 2.3.1 and 2.3.2. In semiconductors, single photon excitation refers to the electron transition process from the valence band to conduction band, where the incident photon possesses an energy $\hbar\omega_1$ such that $\hbar\omega_1 \geq E_g$ as shown in figure 2.17. In the two-photon absorption process, the medium is incident with two photons of energy $\hbar\omega_2$ which are transparent to the medium such that $\hbar\omega_2 < E_g$. When the incident photon has an energy lower than E_g, an electron transition into the conduction band cannot be achieved via a single photon process. However, when the incident field is sufficiently intense, electron can transit into the conduction band via intermediate energy states (see figures 2.17 b-c). The intermediate states can be real (l) or virtual (v) and act as an 'energy ladder' facilitating the electron transition[90]. Figure 2.17 b shows a two-step photo-absorption process called two-photon absorption process and is associated with the absorption of two photons via the real intermediate levels. In this process, the "first" photon excites the electron from ground state into the real intermediate state, and the "second" photon excites the electron from the intermediate state to the final excited state. The life time of carriers in the intermediate states must be short enough to conserve energy, and can be estimated from the uncertainty principle which can be written as[91]

$$\tau_l = \frac{1}{\Delta\omega} = \omega_{il}\,\frac{1}{|\omega_{il} - \omega_2|} \qquad (2.36)$$

where ω_{il} and ω_2 are the transition frequency and the pump frequency, respectively. The intermediate life time, τ_l should be in the time scale of femtoseconds. The virtual intermediate levels assist the electron to simultaneously absorb two photons completing the electron transition into the conduction band. This fictitious virtual level is represented by a linear combination of the wave functions of all real levels $|l_n\rangle$ that combine with $|i\rangle$ by allowed single-photon transitions. The excitation of $|v\rangle$ is equivalent to the off-resonance excitation of all the $|l_n\rangle$ real levels. Similarly, transition to $|f\rangle$ from $|v\rangle$ is also facilitated by real levels. In general, when two or more photons are involved in the electron transition process into the conduction band, it is called a multi-photon process. A multi-photon process can however be induced only at high optical excitation densities as supplied by focused pulsed laser excitations. The intermediate states can be real states introduced by defect levels within the bandgap[92,93]. The dipole selection rules for a two-photon process is different from the single photon process such that the two-photon process can excite carriers to the final states that are normally optically forbidden by single photon excitation. The details on the two-photon selection rules are given in section 2.5.2. Experimental observation of photoluminescence in nitrides and ZnO via single photon requires a UV excitation source, whereas the multi-photon excitation can be achieved via near infra-red pulsed laser excitation. This means that the penetration depth is much less in wide bandgap semiconductors in the case of a single photon excitation. Hence, single photon excited photoluminescence provides information mostly from the surface of the bulk semiconductors; whereas, multi-photon excited photoluminescence provides volume information as depicted in figure 2.18.

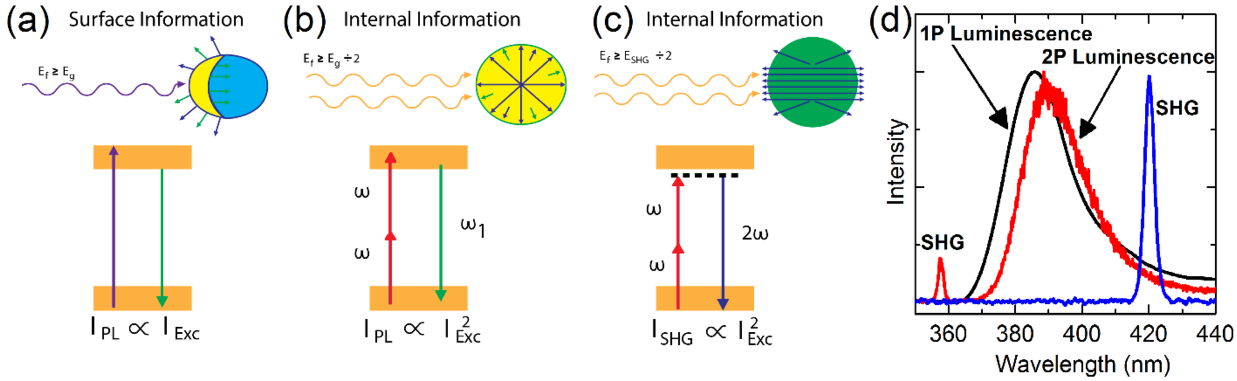

Figure 2.18. Comparison of Luminescence and SHG via single and two-photon excitation. (a) Single photon luminescence provides information of surface defects, (b) two-photon luminescence provides information deep within the bulk, (c) SHG also provides bulk information. Unlike single- and two-photon, SHG does not require excitation into the conduction band and (d) spectra of the different processes from a ZnO crystal.

Apart from photoluminescence, second harmonic generation can also be created via multi-photon excitation process. A brief comparison of them is provided in figure 2.18. More details about SHG can be found in section in 2.3.3. Like multi-photon induced luminescence, SHG can provide internal information of the semiconductor crystal as well. Single and multi-photon luminescence is isotropic. However, unlike MPL, SHG is a coherent process and is highly directional.

2.5.2 Selection Rules for Two-Photon Process

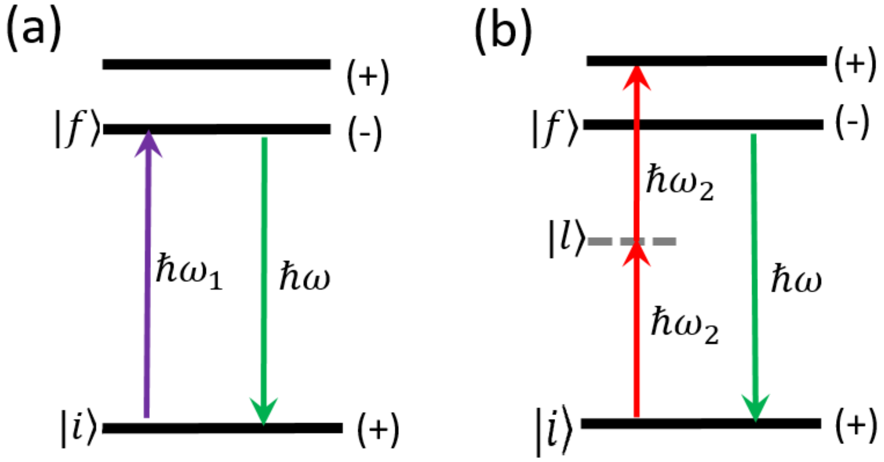

Figure 2.19. Schematic representation of photo-absorption process indicating parity of the states involved in the transition. (a) Single-photon transition occurs between states with opposite parity and (b) two-photon transition process occurs between states with same parity.

Atomic/molecular transition between energy levels of a material is dictated by angular momentum and parity conservation rules[51]. In centrosymmetric crystals, when parity is a good quantum number, single-photon transitions are dipole allowed between states of opposite parity. On the other hand, two-photon transitions are allowed between states with same parity. Therefore, single-photon allowed transitions are two-photon forbidden and vice-versa. Schematic representation two-photon process with parity selection rules is depicted in figure 2.19. In noncentrosymmetric crystals, parity is not a good quantum number and hence the parity selection rules are not valid. Therefore, exciton states allowed in single-photon transition can also be observed in two-photon transition. Also, a larger number of possible excitonic states can be reached via two-photon transition.

2.5.3 Multi-Photon Microscopy

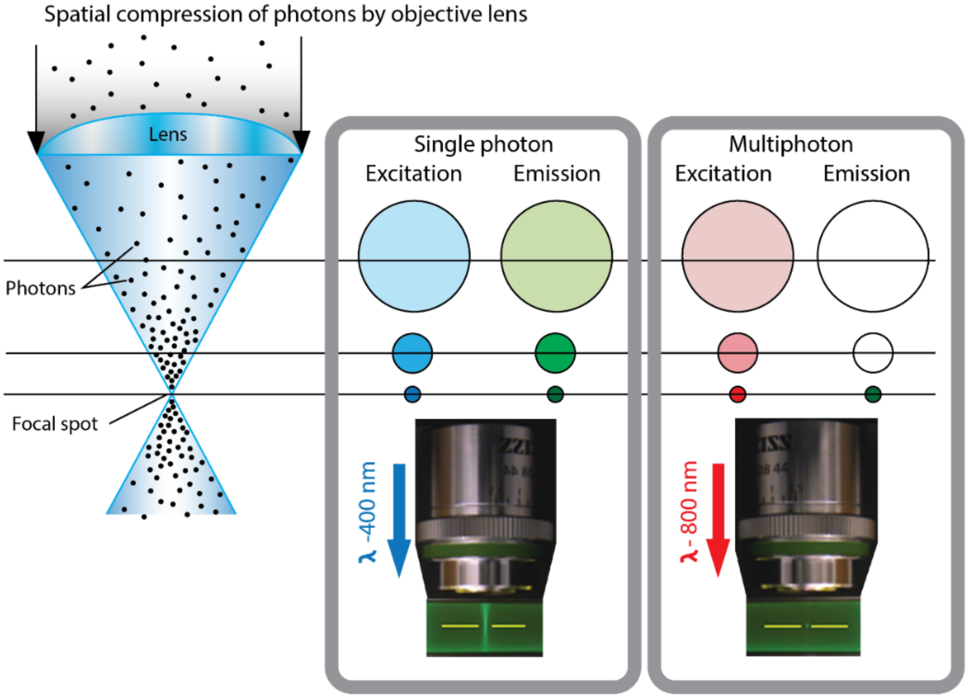

Figure 2.20. Scheme of the working principle of microscopy. (a) Spatial compression of photons through a high NA objective lens, (b) Optical density and emission efficiency along the axial position of a focused beam waist using a single photon excitation and multi-photon excitation. Right panel shows that emission due to multi-photon excitation only occurs at the focused spot providing intrinsic high resolution sectioning.

The most widely used optical technique in this dissertation work to study the nonlinear effects of semiconductors is multiphoton microscopy and spectroscopy. Multiphoton microscopy is a nonlinear microscopy technique which uses the phenomena like MPL and SHG. Since the structures studied in this study ranges from 500 nm to 15 microns, a high numerical aperture of 0.9 objective lens was used to excite individual structures. The highest NA available

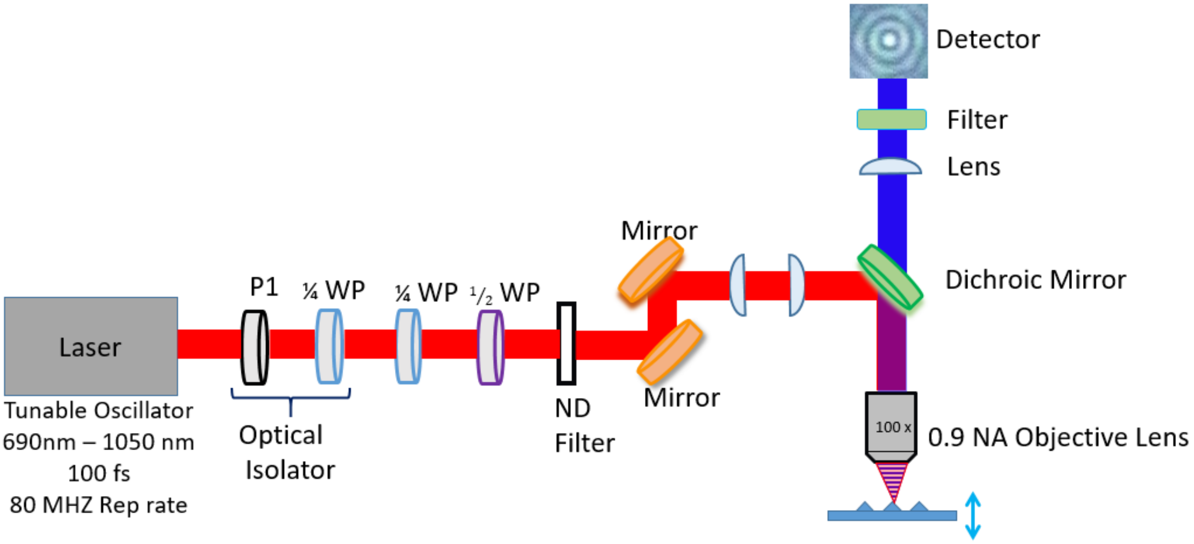

Figure 2.21. Multi-photon microscopy setup in the epi-illumination configuration. A 0.9 NA objective with 100 x magnification is used for excitation of individual sub-micron structures. A DSLR camera is used for imaging, while a TE cooled CCD is used for spectral detection. P1: Glan-Calcite polarizer, WP: waveplate, ND filter: neutral density filter, Beam expander are used to steer and guide the beam to the sample.

on a dry objective lens is 0.9. The nonlinear optical measurements were performed by tightly focusing a femtosecond pulsed near infrared (NIR) light through a high numerical aperture (NA) objective to achieve high resolution with intrinsic confocal sectioning. High NA corresponds to spatial confinement of the excitation power to a smaller focal volume. The basic principle of nonlinear microscopy is represented schematically in figure 2.20. The confocal sectioning of the nonlinear microscopy comes from the fact that

$$I_{NL} = I_{pump}^{n} \qquad (2.37)$$

where I_{NL} is the intensity of the nonlinear light generation and I_{pump} is the intensity of the pump beam. This shows that nonlinear light generation can only happen at the focus of the laser beam as shown in figure 2.20 c, where sufficient optical density can be achieved. In the case of a single photon excitation, this is not the case as emission is present away from the beam waist minima.

Therefore, special techniques must be employed to achieve confocal sectioning in the case of single photon excitation.

The probability, P_{2P} that a material absorbs two photons during a single pulse, in the paraxial approximation is given by[28]

$$P_{2P} \; \alpha \; \frac{\delta_2 P_{ave}^2}{\tau_p f_p^2}\left(\frac{NA^2}{2\eta c\lambda}\right)^2 \qquad (2.38)$$

where τ_p is the pulse width, f_p is the laser repetition rate, $\eta = h/2\pi$, P_{ave} is the time averaged power of the laser beam and λ is the excitation wavelength. From equation (2.38), some of the optimal parameters that maximizes excitation efficiency is the pulse laser parameters and NA of the lens used to focus the beam on the sample. Using high NA objective lens such as 0.9 NA objective lens results in tightly focused beam at the sample. The resolution that can be achieved by a microscope can be determined using point spread function (PSF) of the microscope. PSF describes the response of the microscope in real space. Using Rayleigh criterion, the lateral and axial resolution of a microscope can be calculated as tabulated in table 2.5[91] .

Table 2.5. Spatial resolution of a conventional fluorescence and two-photon fluorescence microscope.

Microscope Design	Lateral Resolution	Axial Resolution
Conventional	$r_{xy} = \frac{0.6\lambda_{em}}{NA}$	$r_z = \frac{2n\lambda_{em}}{NA^2}$
Two-photon	$r_{xy} = \frac{0.7\lambda_{em}}{NA}$	$r_z = \frac{2.3n\lambda_{em}}{NA^2}$

Experimentally, PSF was measured by directly focusing the laser beam on a glass cover slip. The experimental beam waist was measured by taking the FWHM of a one-dimensional intensity histogram across centroid of a low fluence laser spot on the imaging plane of the CCD. Measurements show that the beam waist was approximately 600 nm for 840 nm excitation. For incident beam at 840 nm, lateral resolution can be calculated using conventional formula to be 560 nm.

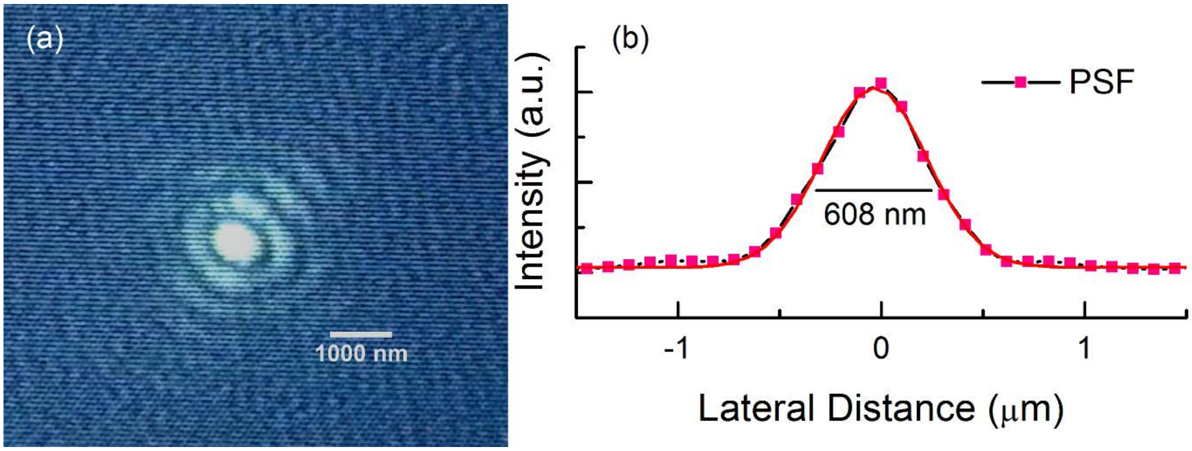

Figure 2.22. PSF of the focused excitation beam on a glass cover slip at 840 nm excitation. (a) CCD image of the PSF and (b) Gaussian fit of the PSF intensity vs lateral distance showing ~ 600 nm FWHM.

The schematic representation of the experimental setup of nonlinear microscopy is shown in figure 2.21. The NIR excitation source was a tunable Ti: Sapphire laser with pulse width of 100 fs and repetition rate of 80 MHz. The excitation wavelengths for multi-photon experiments were tuned from 720nm to 900 nm. The sample was mounted on a microscope stage that allowed XYZ positioning of the sample with ~500 nm resolution. An optical isolator comprising of a polarizer and a quarter wave-plate is used to prevent the reflections back to the laser cavity. This made the excitation laser beam circularly polarized. A variable attenuator was used to control the power of the incident laser on the sample. MPL was collected in the reflection geometry by an optical fiber coupled with a spectrometer equipped with a back thinned CCD detector. A 350-670 nm interference band pass filter was used to block the laser beam from entering into the spectrometer. Polarization dependent studies of MPL and SHG were performed by inserting a combination of a quarter and half wave plate. A second Glan polarizer was used to clean up the polarization completely to produce a linear polarization. This setup provided a polarization vector parallel to the x-axis which can be rotated along the x-y plane of the sample surface.

2.5.4 Photoluminescence Spectroscopy: Far-Field

PL spectroscopy in the far-field can be classified into two forms of excitation as discussed earlier. The most commonly used method to study semiconductor emission is the far-field single photon PL. Various samples used in this study are characterized first using single PL to understand the emission process from a linear optical properties perspective. The schematic of the experimental set up is depicted in figure 2.23. Single-photon optical excitation was achieved using the 325 nm line from a continuous wave Helium- Cadmium laser of 15 mW focused to a 100 µm diameter spot size on the sample. The multi-photon excitation was achieved using a femtosecond Ti:Sapphire laser with a repetition rate of 80 MHz and a pulse width of 100 fs. The incident beams were at a 45^{0} angle from the normal of the sample substrate. The emission from the excited sample is then collected through a pair of collimating lenses and is focused on the entry-slit of a spectrometer with a TE cooled CCD camera. The measured data displays the emitted intensity as a function of wavelength of photons. The collection optics are optimized for UV-visible optics, whereas the excitation optics are swapped between UV and NIR optics depending on the type of excitation. Appropriate laser blocking filters were used to block the incident laser from entering the CCD. A closed cycle helium cryostat that can cool down to 15 K was used whenever a low temperature PL measurement was needed. Information such as peak intensity, energy and line width can be extracted from PL spectrum.

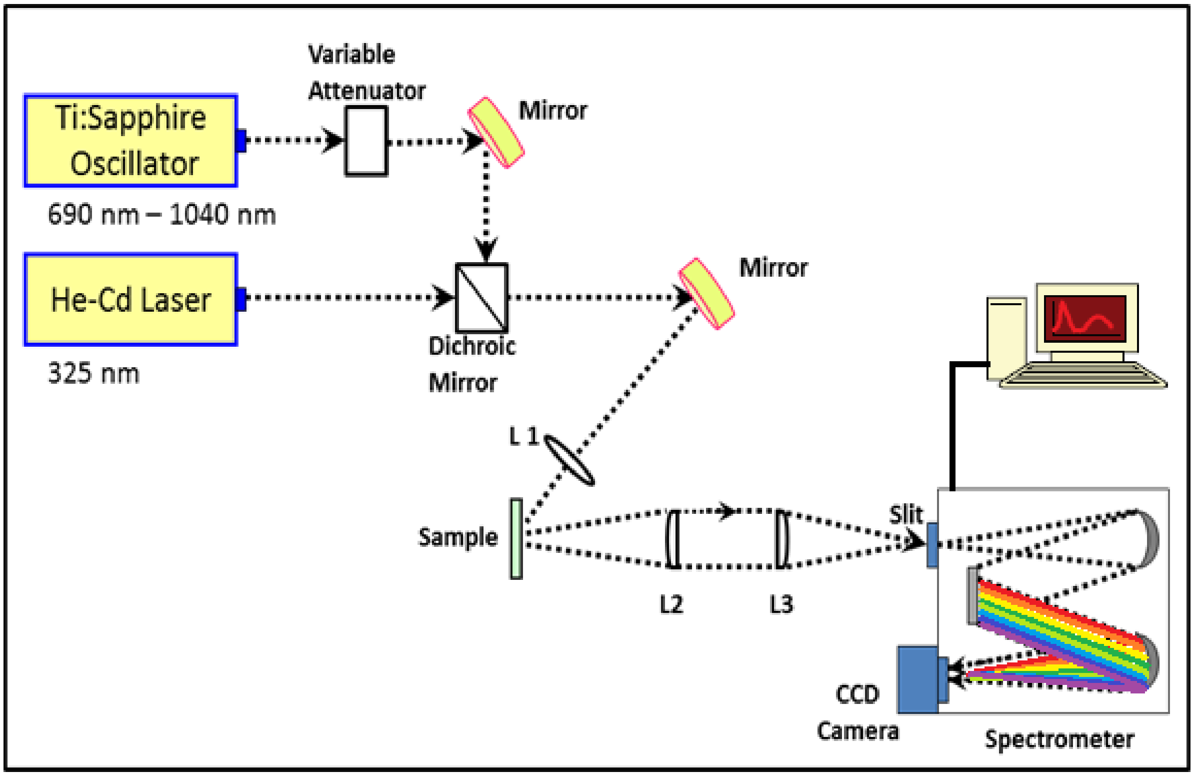

Figure 2.23. Schematic diagram of the PL experimental setup. Excitation from He-Cd laser is used for above bandgap or single photon excitation. Excitation from Ti:Sapphire oscillator is used for below band gap or multi-photon excitation. Variable attenuator consists of a half wave plate and a Glan-Thompson Calcite polarizer was used to control the power of multi-photon excitation laser beam. The PL signal from sample is collected and directed towards a CCD camera after spatial separation of the signal using a UV-Vis grating for recording.

2.5.5 Time-Resolved Photoluminescence Spectroscopy

Time-resolved PL spectroscopy is used for studying transient dynamics of emission. The time scale and shape of the PL decay provide information regarding the physical recombination mechanism. The experimental set up is represented in figure 2.24. TRPL measurements differ from common PL measurements mainly because of the excitation source and detector. To study the transient dynamics, the excitation source used here is a 100 femtosecond pulsed laser. A 100 fs pulsed source should provide an initial significantly short duration pulse which can excite the carriers into the conduction band. This is represented by the rise time of the signal measured.

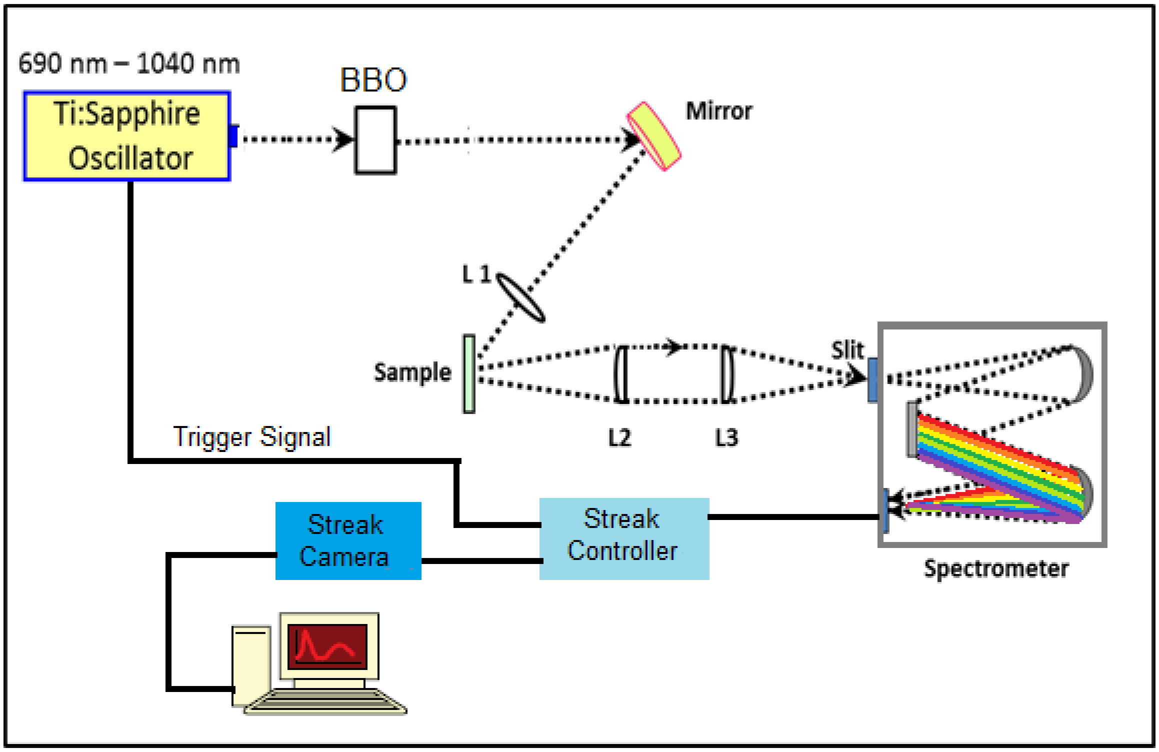

Figure 2.24. Schematic diagram of the time-reolved photoluminescnece spectroscopy set-up. Excitation from the Ti:Sapphire laser is used directly for multi-photon excited TRPL. The NIR beam is directed through a BBO crystal optic assembly for up-converting the energy of the beam for single photon excited TRPL measurements. A streak camera combined with its controller and spectrometer disperses the collected signal in the time and wavelength axes.

The 80 MHz repetition rate of the laser allows a 12.5 ns delay before the second pulse to arrive. This pulse duration allows enough time for the carriers to relax back into the valence band. Majority of the carrier dynamics of the semiconductors fall within a timescale between a few picoseconds for nonradiative recombination, while the radiative recombination is within ~ 10 nanoseconds. The transient PL signal is collected and passed through a grating and directed towards a streak camera with a micro-channel counting plate. This setup disperses the collected PL signal into wavelength and time along the x and y axes, respectively. The minimum resolution of the streak camera (Hamamatsu C4334) used here is ~15 ps. The maximum lifetime we can measure is restricted by the repetition rate of our laser which is ~12 ns. This setup employs a frequency doubling and tripling crystal to up-convert the NIR light from the Ti-Sapphire to produce deep UV to visible excitation. The pulsed laser employed here is tunable from 700 nm to 920 nm with maximum mode lock wavelength at 800 nm with a maximum power of 2.85 W. The PL decay time can generally be fitted using a single- or double exponential decay as:

$$I_{PL}(t) = \sum_{i} A_i \, e^{-t/\tau_i} \qquad (2.39)$$

Where *i* = 1,2, $\sum A_i$ = 1 and τ_i is the decay constant.

2.5.6 Photoluminescence Excitation Spectroscopy

Photoluminescence excitation spectroscopy provides the excitation spectrum profile most efficient to provide a particular emission band of the PL which is of interest. The experiment setup for performing PLE is shown in figure 2.25. This setup used two monochromators, one for the excitation line and the other for the emission line. The excitation used is a 300 W UV enhanced Xenon lamp which is passed through the excitation monochromator and each line is focused onto the sample. The collected PL is focused into a 0.55 m monochromator. The detection wavelength of this monochromator is fixed at the peak maximum of interest, while the excitation wavelength is scanned. The intensity of the PL feature for each excitation wavelength is measured by a photomultiplier tube. Whenever the excitation energy is in resonance with an excited state, the monitored PL emission band will increase in intensity because of the resonant photon absorption by the excited state. Therefore, by scanning the excitation energy through all energy levels, the excited states of a specific PL band emission can be understood. Care must be taken to normalize the intensity variation of Xenon spectra across all energy levels.

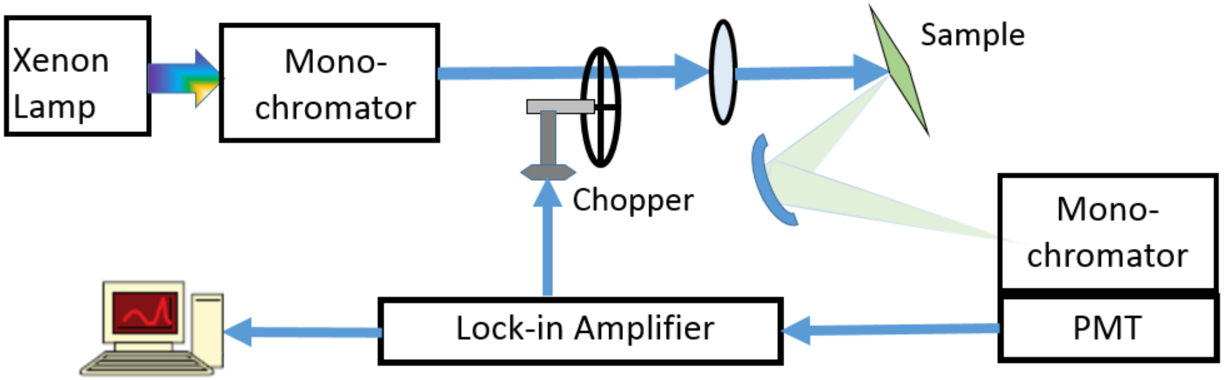

Figure 2.25. Schematic of the experimental setup for photoluminescence excitation spectroscopy.

2.5.7 Scanning Electron Microscopy and Energy Dispersive X-Ray Spectroscopy

The scanning electron microscopy (SEM) is a widely used tool for surface characterization of materials. SEM uses an electron beam instead of an optical beam to examine a material. The advantages of SEM over a traditional optical microscope is that it has a large depth of field and high resolution. Therefore, one can observe fine and closely spaced features. For this study, a field emission scanning electron microscope (FESEM) was used. The working principle of SEM is that an electron beam is focused over the sample surface which results in the generation of electrons. The generated secondary electrons are detected to form high resolution images. Since the secondary electrons are generated from within a few nanometers ad hence provide a good tool for topological studies. The quality of the image depends on the number of secondary electrons generated, which in turn depends on the energy of the applied electron beam generated by an electron gun. The voltage and current parameters of the gun are adjusted to get a good resolution image. Most SEMs are equipped with a detection system that allows to get information about the atomic concentration in a compund called energy dispersive x-ray detection system. In energy dispersive x-ray spectroscopy , the emitted x-rays from the interaction volume provide a chemical fingerprint of the atoms present in the sample. It also enables to study the atomic weight percentange of the chemical species that make the sample under study.

2.5.8 Scanning Transmission Electron Microscopy

Transmission electron microscopy is an electron microscopy technique in which the electron beam is transmitted through a thin sample that interacts with the sample. TEM offers a higher resolution than SEM and is in the atomic scale. The TEM sample requires to be very thin for the electron beam to pass through. Hence sample preparation is so rigorous such that the sample has to be thinned down to less than 100 nm using a focused ion beam to get good resolution images. Once the sample in impinged with an electron beam, various scattering process happen as in SEM method. Scanning transmission electron microscopy is a TEM mode, where the electromagnetic lens focuses the electron beam down to about a nm, which is scanned over the sample. An advanced STEM technique is the high angle annular dark field (HAADF) imaging that provides high atomic number contrast. The HAADF detectors measure the intensity of high angle elastically scattered electrons of the sample. The scattering intensity of the electrons is directly proportional to the sample thickness and square of the atomic mass number. STEM HAADF technique was used to image the InGaN/GaN quantum wells.

2.6 References

(1) Maruska, H. P.; Tietjen, J. J. The Preparation and Properties of Vapor-deposited Single-crystal-line GaN. *Appl. Phys. Lett.* **1969**, *15* (10), 327–329.

(2) Amano, H.; Sawaki, N.; Akasaki, I.; Toyoda, Y. Metalorganic Vapor Phase Epitaxial Growth of a High Quality GaN Film Using an AlN Buffer Layer. *Appl. Phys. Lett.* **1986**, *48* (5), 353–355.

(3) Amano, H.; Kito, M.; Hiramatsu, K.; Akasaki, I. P-Type Conduction in Mg-Doped GaN Treated with Low-Energy Electron Beam Irradiation (LEEBI). *Jpn. J. Appl. Phys.* **1989**, *28* (Part 2, No. 12), L2112–L2114.

(4) Nakamura, S.; Senoh, M.; Mukai, T. High-power InGaN/GaN Double-heterostructure Violet Light Emitting Diodes. *Appl. Phys. Lett.* **1993**, *62* (19), 2390–2392.

(5) Ponce, F. A.; Bour, D. P. Nitride-Based Semiconductors for Blue and Green Light-Emitting Devices. *Nature* **1997**, *386* (6623), 351–359.

(6) Wu, Y.-F.; Kapolnek, D.; Ibbetson, J. P.; Parikh, P.; Keller, B. P.; Mishra, U. K. Very-High Power Density AlGaN/GaN HEMTs. *IEEE Trans. Electron Devices* **2001**, *48* (3), 586–590.

(7) Ambacher, O. Growth and Applications of Group III-Nitrides. *J. Phys. Appl. Phys.* **1998**, *31* (20), 2653–2710.

(8) Neumann, H. J. H. Edgar (Ed.). Properties of Group III Nitrides. (EMIS Datareviews Series No. 11). INSPEC, The Institution of Electrical Engineers, London 1994. 302 Seiten, 121 Abbildungen, 77 Tabellen. ISBN 0–85296–818–3. *Cryst. Res. Technol.* **1995**, *30* (7), 910–910.

(9) Liou, B.-T.; Yen, S.-H.; Kuo, Y.-K. Vegard's Law Deviation in Band Gaps and Bowing Parameters of the Wurtzite III-Nitride Ternary Alloys; Yao, J., Chen, Y. J., Lee, S., Eds.; 2005; p 296.

(10) Morkoç, H. General Properties of Nitrides. In *Nitride Semiconductor Devices*; Wiley-VCH Verlag GmbH & Co. KGaA, 2013; pp 1–61.

(11) Varshni, Y. P. Temperature Dependence of the Energy Gap in Semiconductors. *Physica* **1967**, *34* (1), 149–154.

(12) Piprek, J. Introduction. In *Nitride Semiconductor Devices: Principles and Simulation*; Piprek, J., Ed.; Wiley-VCH Verlag GmbH & Co. KGaA, 2007; pp 1–11.

(13) Gil, B. Group III Nitride Semiconductor Compounds.

(14) Stampfl, C.; Van de Walle, C. G. Energetics and Electronic Structure of Stacking Faults in AlN, GaN, and InN. *Phys. Rev. B* **1998**, *57* (24), R15052–R15055.

(15) Morkoç, H. Comprehensive Characterization of Hydride VPE Grown GaN Layers and Templates. *Mater. Sci. Eng. R Rep.* **2001**, *33* (5–6), 135–207.

(16) Yu, L. P.; Shi, J. Y.; Wang, Y. Z.; Zhang, H. Study of Different Type of Dislocations in GaN Thin Films. *J. Cryst. Growth* **2004**, *268* (3–4), 484–488.

(17) Gibart, P. Metal Organic Vapour Phase Epitaxy of GaN and Lateral Overgrowth. *Rep. Prog. Phys.* **2004**, *67* (5), 667.

(18) Yoshida, S.; Misawa, S.; Itoh, A. Epitaxial Growth of Aluminum Nitride Films on Sapphire by Reactive Evaporation. *Appl. Phys. Lett.* **1975**, *26* (8), 461–462.

(19) Sasaoka, C.; Sunakawa, H.; Kimura, A.; Nido, M.; Usui, A.; Sakai, A. High-Quality InGaN MQW on Low-Dislocation-Density GaN Substrate Grown by Hydride Vapor-Phase Epitaxy. *J. Cryst. Growth* **1998**, *189–190*, 61–66.

(20) Kitamura, S.; Hiramatsu, K.; Sawaki, N. Fabrication of GaN Hexagonal Pyramids on Dot-Patterned GaN/Sapphire Substrates via Selective Metalorganic Vapor Phase Epitaxy. *Jpn. J. Appl. Phys.* **1995**, *34* (Part 2, No. 9B), L1184–L1186.

(21) Yang, W.; McPherson, S. A.; Mao, Z.; McKernan, S.; Carter, C. B. Single-Crystal GaN Pyramids Grown on (111)Si Substrates by Selective Lateral Overgrowth. *J. Cryst. Growth* **1999**, *204* (3), 270–274.

(22) Zheleva, T. S.; Nam, O.-H.; Bremser, M. D.; Davis, R. F. Dislocation Density Reduction via Lateral Epitaxy in Selectively Grown GaN Structures. *Appl. Phys. Lett.* **1997**, *71* (17), 2472–2474.

(23) Gačević, Ž.; Gómez Sánchez, D.; Calleja, E. Formation Mechanisms of GaN Nanowires Grown by Selective Area Growth Homoepitaxy. *Nano Lett.* **2015**, *15* (2), 1117–1121.

(24) Miyake, H.; Takeuchi, R.; Hiramatsu, K.; Naoi, H.; Iyechika, Y.; Maeda, T.; Riemann, T.; Bertram, F.; Christen, J. High Quality GaN Grown by Facet-Controlled ELO (FACELO) Technique. *Phys. Status Solidi A* **2002**, *194* (2), 545–549.

(25) Akasaka, T.; Kobayashi, Y.; Ando, S.; Kobayashi, N.; Kumagai, M. Selective MOVPE of GaN and AlxGa1−xN with Smooth Vertical Facets. *J. Cryst. Growth* **1998**, *189–190*, 72–77.

(26) Bernardini, F.; Fiorentini, V.; Vanderbilt, D. Spontaneous Polarization and Piezoelectric Constants of III-V Nitrides. *Phys. Rev. B* **1997**, *56* (16), R10024–R10027.

(27) Takeuchi, T.; Sota, S.; Katsuragawa, M.; Komori, M.; Takeuchi, H.; Amano, H.; Akasaki, I. Quantum-Confined Stark Effect due to Piezoelectric Fields in GaInN Strained Quantum Wells. *Jpn. J. Appl. Phys.* **1997**, *36* (4A), L382.

(28) Ambacher, O.; Smart, J.; Shealy, J. R.; Weimann, N. G.; Chu, K.; Murphy, M.; Schaff, W. J.; Eastman, L. F.; Dimitrov, R.; Wittmer, L.; Stutzmann, M.; Rieger, W.; Hilsenbeck, J. Two-Dimensional Electron Gases Induced by Spontaneous and Piezoelectric Polarization Charges in N- and Ga-Face AlGaN/GaN Heterostructures. *J. Appl. Phys.* **1999**, *85* (6), 3222–3233.

(29) Monemar, B.; Pozina, G. Group III-Nitride Based Hetero and Quantum Structures. *Prog. Quantum Electron.* **2000**, *24* (6), 239–290.

(30) Miller, D. A. B.; Chemla, D. S.; Damen, T. C.; Gossard, A. C.; Wiegmann, W.; Wood, T. H.; Burrus, C. A. Band-Edge Electroabsorption in Quantum Well Structures: The Quantum-Confined Stark Effect. *Phys. Rev. Lett.* **1984**, *53* (22), 2173–2176.

(31) Schwarz, U. T.; Kneissl, M. Nitride Emitters Go Nonpolar. *Phys. Status Solidi RRL – Rapid Res. Lett.* **2007**, *1* (3), A44–A46.

(32) Frentrup, M.; Ploch, S.; Pristovsek, M.; Kneissl, M. Crystal Orientation of GaN Layers on (1010) M-Plane Sapphire. *Phys. Status Solidi B* **2011**, *248* (3), 583–587.

(33) Paskova, T. Development and Prospects of Nitride Materials and Devices with Nonpolar Surfaces. *Phys. Status Solidi B* **2008**, *245* (6), 1011–1025.

(34) Ahn, D.; Park, S.-H. Theory of Non-Polar and Semi-Polar Nitride Semiconductor Quantum-Well Structures. *Semicond. Sci. Technol.* **2012**, *27* (2), 24011.

(35) Scholz, F. Semipolar GaN Grown on Foreign Substrates: A Review. *Semicond. Sci. Technol.* **2012**, *27* (2), 24002.

(36) Ho, I.; Stringfellow, G. B. Solid Phase Immiscibility in GaInN. *Appl. Phys. Lett.* **1996**, *69* (18), 2701.

(37) Waltereit, P.; Brandt, O.; Trampert, A.; Grahn, H. T.; Menniger, J.; Ramsteiner, M.; Reiche, M.; Ploog, K. H. Nitride Semiconductors Free of Electrostatic Fields for Efficient White Light-Emitting Diodes. *Nature* **2000**, *406* (6798), 865–868.

(38) Schmidt, M. C.; Kim, K.-C.; Farrell, R. M.; Feezell, D. F.; Cohen, D. A.; Saito, M.; Fujito, K.; Speck, J. S.; DenBaars, S. P.; Nakamura, S. Demonstration of Nonpolar *M* -Plane InGaN/GaN Laser Diodes. *Jpn. J. Appl. Phys.* **2007**, *46* (No. 9), L190–L191.

(39) Häberlen, M.; Badcock, T. J.; Moram, M. A.; Hollander, J. L.; Kappers, M. J.; Dawson, P.; Humphreys, C. J.; Oliver, R. A. Low Temperature Photoluminescence and Cathodoluminescence Studies of Nonpolar GaN Grown Using Epitaxial Lateral Overgrowth. *J. Appl. Phys.* **2010**, *108* (3), 33523.

(40) Chang, H. J.; Hsieh, Y. P.; Chen, T. T.; Chen, Y. F.; Liang, C.-T.; Lin, T. Y.; Tseng, S. C.; Chen, L. C. Strong Luminescence from Strain Relaxed InGaN/GaN Nanotips for Highly Efficient Light Emitters. *Opt. Express* **2007**, *15* (15), 9357.

(41) Boulbar, E. D. L.; Gîrgel, I.; Lewins, C. J.; Edwards, P. R.; Martin, R. W.; Šatka, A.; Allsopp, D. W. E.; Shields, P. A. Facet Recovery and Light Emission from GaN/InGaN/GaN Core-Shell Structures Grown by Metal Organic Vapour Phase Epitaxy on Etched GaN Nanorod Arrays. *J. Appl. Phys.* **2013**, *114* (9), 94302.

(42) Chang, Y.-L.; Wang, J. L.; Li, F.; Mi, Z. High Efficiency Green, Yellow, and Amber Emission from InGaN/GaN Dot-in-a-Wire Heterostructures on Si(111). *Appl. Phys. Lett.* **2010**, *96* (1), 13106.

(43) Hong, Y. J.; Lee, C.-H.; Yoon, A.; Kim, M.; Seong, H.-K.; Chung, H. J.; Sone, C.; Park, Y. J.; Yi, G.-C. Visible-Color-Tunable Light-Emitting Diodes. *Adv. Mater.* **2011**, *23* (29), 3284–3288.

(44) Sun, Q.; Han, J. Heteroepitaxy of Nonpolar and Semipolar GaN. In *GaN and ZnO-based Materials and Devices*; Pearton, S., Ed.; Springer Series in Materials Science; Springer Berlin Heidelberg, 2012; pp 1–27.

(45) Djurišić, A. B.; Kwok, W. M.; Leung, Y. H.; Chan, W. K.; Phillips, D. L.; Lin, M. S.; Gwo, S. Ultrafast Spectroscopy of Stimulated Emission in Single ZnO Tetrapod Nanowires. *Nanotechnology* **2006**, *17* (1), 244.

(46) Fikry, M.; Madel, M.; Tischer, I.; Thonke, K.; Scholz, F. Luminescence Properties of Epitaxially Grown GaN and InGaN Layers around ZnO Nanopillars. *Phys. Status Solidi A* **2011**, *208* (7), 1582–1585.

(47) Boyd, R. W. Chapter 1 - The Nonlinear Optical Susceptibility. In *Nonlinear Optics (Third Edition)*; Academic Press: Burlington, 2008; pp 1–67.

(48) Zernike, F.; Midwinter, J. E.; Physics. *Applied Nonlinear Optics*; Dover Publications, 2006.

(49) Sheik-Bahae, M.; Hagan, D. J.; Van Stryland, E. W. Dispersion and Band-Gap Scaling of the Electronic Kerr Effect in Solids Associated with Two-Photon Absorption. *Phys. Rev. Lett.* **1990**, *65* (1), 96–99.

(50) Sutherland, R. Handbook of Nonlinear Optics https://www.crcpress.com/Handbook-of-Nonlinear-Optics/Sutherland/p/book/9780824742430 (accessed Oct 15, 2016).

(51) Peyghambarian, N.; Koch, S. W.; Mysyrowicz, A. *Introduction to Semiconductor Optics*; Prentice Hall series in solid state physical electronics; Prentice Hall: Englewood Cliffs, N.J, 1993.

(52) Mohler, W.; Millard, A. C.; Campagnola, P. J. Second Harmonic Generation Imaging of Endogenous Structural Proteins. *Methods San Diego Calif* **2003**, *29* (1), 97–109.

(53) Kittel, C. Wiley: Introduction to Solid State Physics, 8th Edition - Charles Kittel http://www.wiley.com/WileyCDA/WileyTitle/productCd-EHEP000803.html (accessed Oct 17, 2016).

(54) Optical Properties of Solids | Mark Fox | 9780199573363 | Oxford University Press Canada http://www.oupcanada.com/catalog/9780199573363.html (accessed Oct 18, 2016).

(55) Institutionen för fysik, kemi och biologi, Funktionella elektroniska material, Linköpings universitet, Sweden; Chen, S. *Excitonic Effects and Energy Upconversion in Bulk and Nanostructured ZnO*; Linköping University Electronic Press, 2013.

(56) Diaspro, A. Wiley: Confocal and Two-Photon Microscopy: Foundations, Applications and Advances - Alberto Diaspro http://www.wiley.com/WileyCDA/WileyTitle/productCd-0471409200.html (accessed Oct 19, 2016).

(57) Ivanov, V. Y.; Semenov, Y. G.; Surma, M.; Godlewski, M. Anti-Stokes Luminescence in Chromium-Doped ZnSe. *Phys. Rev. B* **1996**, *54* (7), 4696–4701.

(58) Cao, W.; Du, W.; Su, F.; Li, G. Anti-Stokes Photoluminescence in ZnO Microcrystal. *Appl. Phys. Lett.* **2006**, *89* (3), 31902.

(59) Denk, W.; Strickler, J. H.; Webb, W. W. Two-Photon Laser Scanning Fluorescence Microscopy. *Science* **1990**, *248* (4951), 73–76.

CHAPTER 3

MAPPING OF NONLINEAR OPTICAL PROPERTIES ALONG THE SYMMETRIC AXIS OF THREE DIMENSIONAL GAN MICRO-CAVITY EMITTERS

3.1 Introduction

Semiconductor based micro- and nano-structures grown in a systematic and controlled way using selective area growth are emerging as a promising route toward devices for integrated optical circuitry in optoelectronics and photonics field [1–3]. Advantages of these structures are high aspect ratio providing large surface-to-volume, improved light extraction efficiency and reduction in strain induced by growth on lattice mismatched substrates[4,5]. The nonlinear optical response of low dimensional structures are of current interest because of the need for active elements in photonic applications[6–10]. Nonlinear optical effects such as harmonic generation, sum frequency generation etc. are preferred as they can be used to make coherent sources; especially doubling a source with optical communication band frequency[11,12]. Input optical pump density dependence on the two-photon induced luminescence and second harmonic generation (SHG) leads to spatial confinement improving resolution in imaging. Two-photon induced luminescence is a third order nonlinearity where as SHG is a second order nonlinearity. Wurtzite semiconductors like ZnO and GaN, owing to their non-centrosymmetric crystal structure are good candidates because of their high nonlinear susceptibility co-efficients[13–17].

Parts of this chapter have been previously published, either in part or in full, from "Hyperspectral Nonlinear Optical Light Generation from a Monolithic GaN Microcavity", S. Butler et al, Advanced Optical Materials 2017, 5, 1600804. Copyright © Wiley-VCH Verlag GmbH & Co. KGaA, DOI: 10.1002/adom.201600804. Reproduced with permission from Wiley-VCH Verlag GmbH & Co. KGaA.

Also, sharp boundaries and interfaces with small dimensions possesses high charge density and electrostatic potential gradients which increases the total dipole moments, thus increasing their nonlinearity[18]. Selectively grown micro- and nano-structures made of these materials enable us to quantitatively measure the nonlinear properties of individual structures to make unambiguous conclusions. ZnO is one of the well-studied material for nonlinear applications in the literature[10,19–21]. However, GaN is of particular interest due to its technological importance. GaN technology stands in second place next to Silicon in growth and manufacturing advancements and semiconductor applications. Properties that make GaN attractive are wide and direct bandgap, chemical inertness, high thermal stability and mechanical robustness[22]. III-nitride semiconductors are very stable and resistant to degradation under high electric fields and temperatures due to strong chemical bonds[23]. Also, band gap of GaN and thus emission range can be tuned from IR to deep UV by alloying with other group III elements.

The historical reason for selecting GaN micro-pyramids for nonlinear optical studies is because these structures were first introduced in the late 90's, gained immense popularity[24] for their linear optical properties and was then abandoned for a decade. Linear optical properties like WGM micro-cavity formation and lasing were observed from similar structures[25–27] in late 1990's. Recently, since 2010, a renewed interest in GaN micro-pyramid structures has resulted in application discoveries such as single photon emitters[2], and LEDs[28]. The scientific reasons for studying these structures are 1) although linear optical responses of various shaped GaN structures have been reported, reports on nonlinear optical response of controlled grown structures of GaN are rare, 2) the smaller dimensions makes it possible to generate SHG without the stringent phase matching conditions required in a bulk crystal[29] and 3) micro-cavity formation in the nonlinear regime along with established control growth would make these structures ideal for all optical circuitry applications.

The research works on nonlinear studies on GaN in the accessible literature include quantitative evaluation of the magnitude of the nonlinear susceptibility elements in GaN films[13], two-photon absorption study of GaN[30], CW blue green emission from GaN films grown by MBE by SFG and SHG[31], multiphoton-induced photoluminescence of bulk GaN excited below the middle of the band gap[32], accurate measurement of quadratic nonlinear-optical coefficients of high-quality bulk GaN[33], second- and third-harmonic (THG) generation and THG induced photoluminescence in a two-dimensional GaN photonic crystal[34], large enhancement of reflected SHG using the one-dimensional photonic effect in regularly arranged InGaN/GaN single-quantum-well nanowalls[35], far field imaging of SHG in a single GaN nanowire[7] and resonant second harmonic generation in a GaN 2D photonic crystal[12]. Literature review demonstrates thorough nonlinear optical studies of bulk GaN. Although efforts have been put to studying photonic crystal structures made of GaN, there is no study available on the GaN three dimensional structures made by SAG/SAE methods. For practical applications, semiconductor materials are good candidates for multi-photon devices because of their high MPA co-efficient and mature device manufacturing techniques. Furthermore, GaN micro-pyramids are good candidates of hexagonal cavities where multiple round trips within a microcavity can enhance the light matter interaction due to the high Q of the cavity without increasing the device dimensions.

This chapter presents the experimental study of nonlinear optical properties; SHG and multi-photon induced PL from an individual GaN micro-pyramid at room temperature, and how these properties are affected by the geometry of the pyramid. Multi-photon induced ultra-violet luminescence (UVL) and yellow luminescence (YL) were observed for excitation at and above half bandgap energy of GaN, whereas for excitation below half bandgap energy an additional narrow peak recognized as SHG was also observed along with UVL and YL emission peaks. The evolution of both processes are mapped along the symmetric axis of the micro-pyramid for multiple fundamental input frequencies of light. Studies were conducted on micro-pyramids with two different dimensions; a 3 µm and a 15 µm. The aspect ratio of both pyramids was close to unity. The nonlinear light generation such as MPL and SHG from the GaN micro-pyramid is optimized by controlling the cavity modes formed by the semipolar $(1\bar{1}01)$ wurtzite facets and the tip enhanced effects from the pyramid. Spatial dependent measurements along the symmetric axis of the pyramid (optic axis direction) shows higher intensity of second harmonic signal about 3-4 microns above the base of the pyramid in the case of 15 µm tall pyramids. In contrast, UVL and YL are higher towards the apex of the pyramid for excitation energies below the half band gap of GaN. However, YL luminesce seemed generally uniform for excitations above $E_g/2$. The dependence of SHG and MPL intensities on input laser power was measured to determine how many photons were involved in the excitation/annihilation process to induce the nonlinear effects. For excitations with photon energies higher than half bandgap energy of GaN, UVL was induced by two photon absorption, whereas for excitations with energies lower than the half bandgap energy of GaN, UVL was induced by three photon absorption. SHG is evidenced by the quadratic power dependence and spectral dependence on the incident fundamental beam.

3.2 Materials and Methods

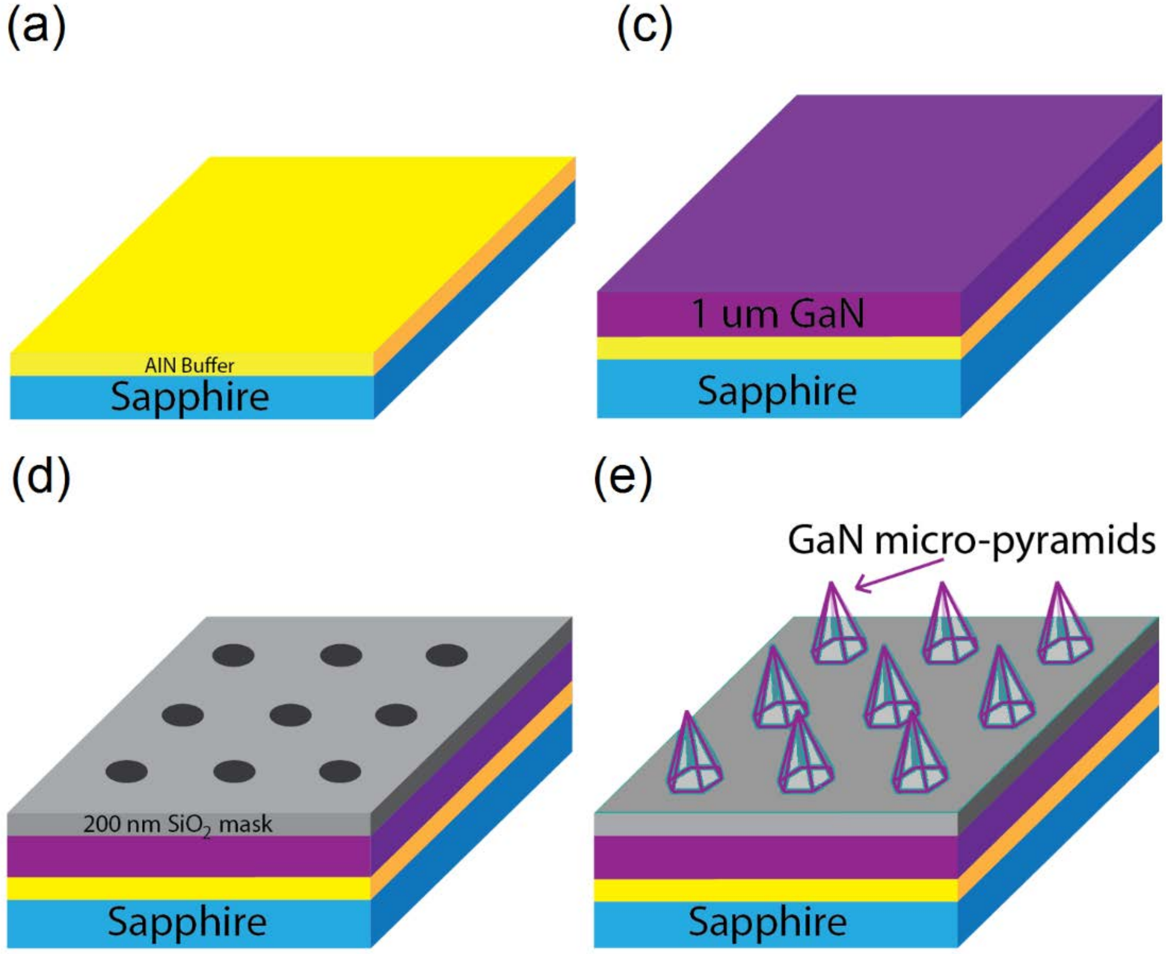

Figure 3.1. Schemes representing the growth process of GaN pyramids. a) Clean sapphire substrate to initiate growth process, b) AlN and GaN epilayers overgrown on sapphire. AlN buffer layer reduces lattice mismatch between GaN and sapphire, GaN epilayer acts as the buffer layer for the growth of GaN pyramids, c) SiO2 mask with windows to achieve selective area epitaxial growth, d) GaN micro-pyramids grown using epitaxial process.

Test samples were an array of GaN micro-pyramids with different dimensions; a 3 ± 1 µm (referred to as smaller pyramid hereafter) and a 15 ± 1 µm (referred to as larger pyramid hereafter). The arrays of GaN micro pyramids were prepared using selective area epitaxial layer overgrowth (SA-ELO) as discussed in chapter 2 in a metal organic chemical vapor deposition (MOCVD) chamber. The SA-ELO process is represented in figure 3.1. In this fabrication process, a

1 µm GaN buffer layer was deposited on a c-plane sapphire substrate with a 100 nm aluminum indium nitride (AlN) buffer layer. A 200 nm silicon dioxide (SiO_2) masking layer was deposited on the GaN epilayer using plasma enhanced CVD process to serve as a growth mask for position controlled selective growth of GaN micro-pyramids. An array of circular windows was fabricated by optical lithography and dry etching techniques. For larger size GaN pyramid array, window patterns had a diameter and pitch of 5 µm and 20 µm respectively; whereas, for smaller GaN pyramid array sample, window openings had a diameter and pitch of 3 µm and 10 µm. GaN micro pyramids were then selectively grown on the patterned substrate in a MOCVD chamber at 1050^o C with ammonia (NH_3) and triethylgallium (TEG) as reactants with hydrogen as carrier gas. GaN pyramids with 15 µm size were grown for a three-hour duration whereas 3 µm size pyramids were grown for 26 minutes. In the case of larger pyramids, during the three-hour lateral overgrowth process, NH_3 flow rate was maintained at 1.8 standard liters per min (slm), whereas TEG flow rate was varied from 1.8 µmol/min for the first hour to 5.3 µmol/min for the remaining two hours of growth process. For the smaller pyramids, the growth temperature was maintained at 1110^o C with NH_3 and TEG flow rate at 6 slm and 150 µmol/min.

Linear optical excitation with above the bandgap energy (referred to as single photon excitation in this dissertation) was used to obtain a general understanding of the steady state emission properties of GaN micro-pyramid emitters. This was achieved using the 325 nm line from a continuous wave (CW) Helium- Cadmium laser with 15 mW power focused to a 100 µm diameter spot size on the sample. The incident beam was at a 45-degree angle from the normal of the sample substrate, whereas the luminescence from the sample was collected normal to the sample surface. Single photon luminescence was also performed at cryogenic temperatures of

15 K for CW excitation. Photoluminescence excitation (PLE) spectroscopy was done to estimate the absorption peak position of GaN pyramid samples. To understand the nonlinear optical properties of GaN pyramid emitters, near infra-red (NIR) laser was used as the pumping source to induce multi-photon transitions in the band gap of GaN. Multi-photon excitation was achieved using a femtosecond tunable Titanium: Sapphire laser with pulse width of 100 fs and repetition rate of 80 MHz. The excitation wavelengths for multi-photon induced PL experiments were tuned from 720 nm to 900 nm. The excitation was focused to a diffraction limited spot size of 600 nm in the lateral direction and 1200 nm in the axial dimension via a 0.9 NA objective lens. The sample was mounted on a microscope stage that allowed XYZ positioning of the sample with approximately 500 nm resolution. A variable attenuator was used to control the power of the incident laser on the sample. The input laser beam has circular polarization set by a quarter waveplate. Emission from the sample was collected in the reflection geometry by an optical fiber coupled with a spectrometer equipped with a thermoelectrically cooled CCD detector. A 350-670 nm interference band pass filter was used to block the laser beam from entering into the spectrometer. The surface morphology and elemental composition of GaN micro-pyramids were evaluated using scanning electron microscopy (SEM) with a FEI Nova Nanolab 200 electron microscope. The energy of the beam used for characterization was 5kV.

3.3 Results and Discussion

The results and characterization of both GaN pyramid emitters with different dimensions were studied to understand the nonlinear optical effects and are presented in the following sections. Nonlinear light generation such as MPL and SHG were observed from both samples. The origin of the nonlinear light generation was concluded mainly from the studies on the larger pyramid sample because it provided a platform for less experimental uncertainties. This is due to the fact that the dimension of the pyramid is much larger relative to the lateral and axial resolution of the pump beam as compared to the 3 μm pyramid array. A slight deviation in the positioning of the pump beam on the apex of the pyramid can introduce a significant change in the reflection and transmission properties of the incident light and subsequent collection of the nonlinear signal by the detector. Also, the larger pyramid sample showed better homogeneity in the shape and size distribution compared to the smaller pyramid array.

3.3.1 Morphology of Gan Micro-Pyramids

The high resolution images taken using SEM of larger pyramids and smaller pyramids are presented in figures 3.2 and 3.3 respectively. These figures show top and tilted views of a two dimensional array of selectively grown GaN hexagonal pyramids with semi-polar $\{1\bar{1}01\}$ facets respectively. There are no signs of GaN deposition on the SiO_2 mask indicating excellent selectivity of GaN pyramid growth. The circular openings in the SiO_2 mask under optimum conditions[36–38] enabled the growth of hexagonal pyramids with six $\{1\bar{1}01\}$ converged facets. The pyramid structure is formed as a direct consequence of the hexagonal characteristics of the wurtzite crystal. Also, under certain growth conditions, the $\{1\bar{1}01\}$ plane is energetically more stable[36,37]. The images of a single pyramid in figures 2 and 3 show six facets of the pyramid with extremely smooth surfaces (figures 3.2c, 3.2d and 3.3c) as there is no etching involved unlike top-down growth process.

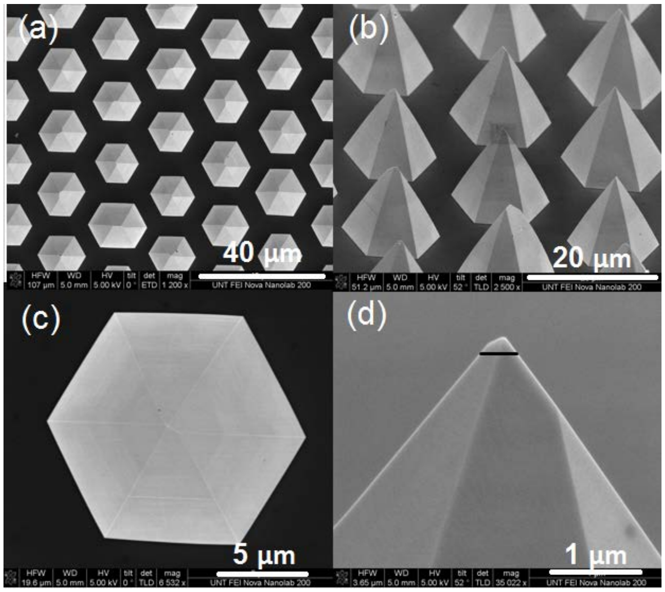

Figure 3.2. SEM images of 15 µm sized GaN micro-pyramids grown on sapphire using selective lateral overgrowth. a) Top view of an array of GaN micro-pyramids, b) tilted and zoomed in view of an array of GaN micro-pyramids, c) top view of a single pyramid and d) tilted view of the apex of a single pyramid.

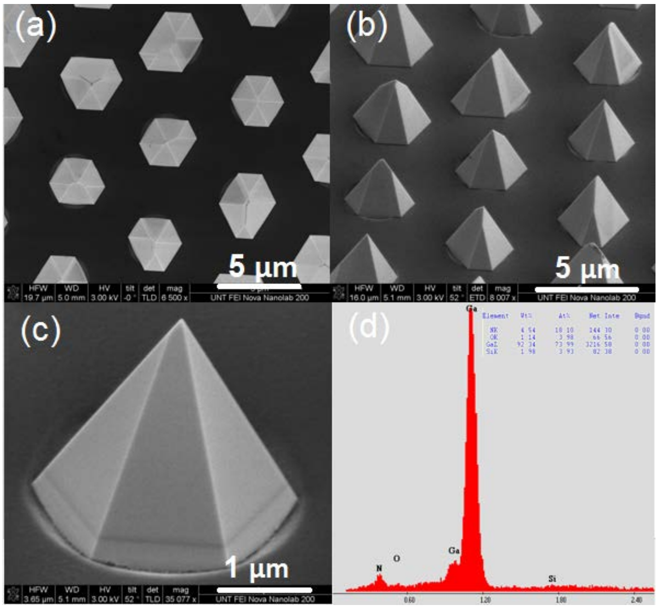

Element	Wt%	At%	Net Inte	Bgnd
NK	4.54	18.10	144.30	0.00
OK	1.14	3.98	66.56	0.00
GaL	92.34	73.99	3216.58	0.00
SiK	1.98	3.93	82.38	0.00

Figure 3.3. SEM images of 3 µm sized GaN micro-pyramids grown on sapphire using selective lateral overgrowth. a) Top view of an array of GaN micro-pyramids, b) tilted view of an array of GaN micro-pyramids, c) tilted view of a single pyramid and d) EDX spectrum from a point on the single pyramid. Lower intensity of N peak is due to the limitations of the collection optics before detector.

Figure 3.2 shows the morphology of the larger pyramids. Individual pyramids have a base diameter and height of approximately 15 µm creating an aspect ratio of 1. The angle formed between the facet and SiO_2 mask is ~ 62 degrees. From figure 2d, the sharp apex of the pyramid can be seen; the black line at the tip measures 210 nm. Occasionally, the convergence of the facets at apices of the pyramids are skewed forming a ridge due to the self-limited facet growth mechanism[38].

Figure 3.3 shows the morphology of the smaller pyramids. The base diameter and height of an individual pyramid is approximately 3 µm. Compared to the larger ones, the symmetry of the shape of the smaller pyramids are less uniform. This could have resulted from the fluctuations in temperature or in the flow rate of the ingredients during the short growth period. Growth mechanism of smaller pyramids were thoroughly studied by Anders Lundskog et al[37,38] and has established the optimum conditions for the growth of homogenous and symmetrical pyramids with a dimension of 3 µm for future work. Figure 3.3c shows a symmetrical pyramid. At the base of the pyramid, one can see the mask opening through which the GaN pyramid was grown. The 15 µm pyramids, on the other hand, were overgrown laterally for several microns in width over the buffer regions facilitated by 5 µm mask windows.

GaN materials grown using ELO method have a high impurity concentration towards the bottom of the pyramidal volume due to the SiO_2 mask. Detailed structural analysis[39,40] of similar GaN pyramids mostly saw threading dislocations towards the center core of the base. Figure 3.4, reproduced from references 38 and 39 is used here to provide an understanding of the growth related structural defects introduced in the GaN pyramids. Figure 3.4 represents schematics and the transmission electron microscopy (TEM) images taken from a 15 µm pyramid that was grown under similar conditions on a silicon carbide substrate. Nearly defect free regions were observed in the lateral grown regions away from the mask openings[39]. Use of Sapphire substrate would lower the dislocation density because of better lattice parameter match compared to SiC.

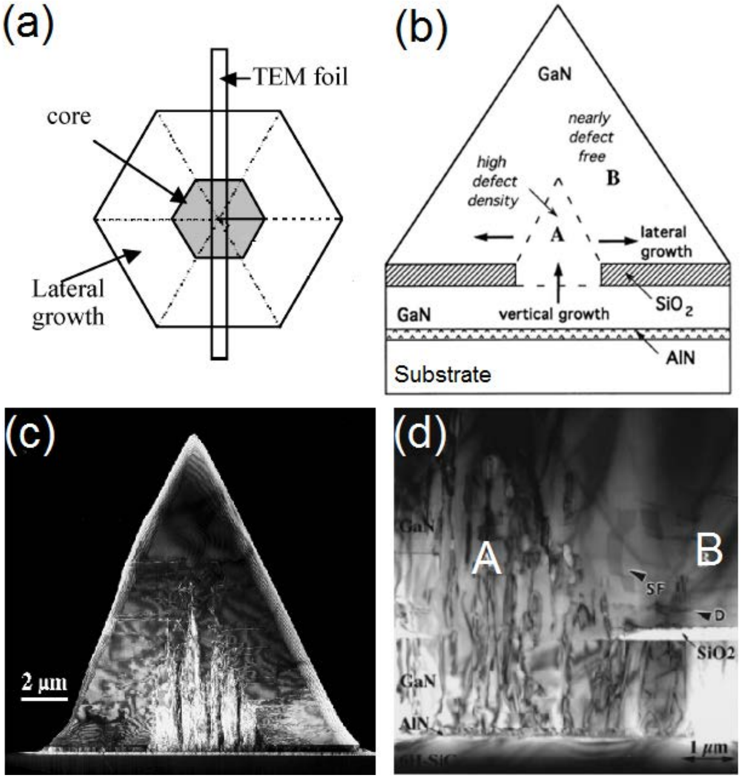

Figure 3.4. Microstructure of SA-ELO GaN micro-pyramid. Schematics representing (a) a top view showing the cross-sectional cut for TEM and (b) a cross section of the pyramid. TEM images of (c) the cross-section specimen of the pyramid at low magnification and (d) core region of the cross-section at a higher magnification [Schematics and images are adapted from references 38 and 39].

The SA-ELO method consists of two main steps. 1) vertical growth and 2) lateral growth. During the first step, the deposited GaN grows selectively on the GaN layer (which acts as seeds) exposed by the mask window openings. Growth at this region is relatively rapid than the growth over the surrounding SiO_2 mask region due to the larger sticking coefficient, *s*, of the Ga adatoms on the GaN seed layer. Due to the lower s value on SiO_2 masked region, the Ga adatoms would either evaporate or diffuse along the surface towards the opening in the mask. During the second step, simultaneous growth of GaN in the vertical and lateral direction occur over the mask from the material which emerges over the windows. The laterally grown GaN is bonded to the underlying SiO_2 mas strongly that it does not break away on cooling. The lateral overgrowth occurs without competing nucleation on the masked areas, thus propagation of dislocations from the seeding layer is partially blocked by the mask. However, lateral cracking within the SiO_2 is likely to occur as a result of thermal stresses generated on cooling. Studies indicate that SA-ELO of GaN micro-structures grown on a buffer layer considerably reduces the dislocation density by four to six orders of magnitude[41–43].

As shown in figure 3.4, the microstructure of each pyramid can be classified into two regions denoted by A and B (see figure 3.4 b and d). Region A, the core of the pyramid is located just above the unmasked window area where vertical growth of GaN happens contains dislocations at a density similar to that of the underlying GaN seed layer that propagates perpendicularly for ~ 3 um height into the core of the pyramid from the GaN/GaN interface (figure 3.4d). The defects in the underlying GaN seed layer are threading dislocations present in the AlN and GaN layers caused by the mismatch in lattice parameters at these interfaces and coefficients of thermal expansion among these phases. The dislocation density is mainly confined in the lower one third of the pyramid height especially in the core region A and diminishes into the bulk of the pyramid. Region B contains very few dislocations lying parallel to the interface plane in the outer part of the pyramid core (figure 3.4d) and a low concentration of overlapping stacking faults (SF) close to the GaN/SiO2 interface. Nearly defect free regions were observed at greater distances away from the core of the pyramid.

3.3.2 Light Generation from GaN Micro-Pyramids

Light generation resulting from first, second and third order susceptibility from both GaN micro-pyramid structures were studied and is presented in the following sub-sections. In order to provide the readers with a clear discussion on the origin of nonlinear effects in a GaN micro-pyramid, I will use the data obtained from the larger samples.

3.3.2.1 Linear Light Interaction in GaN Micro-Pyramids

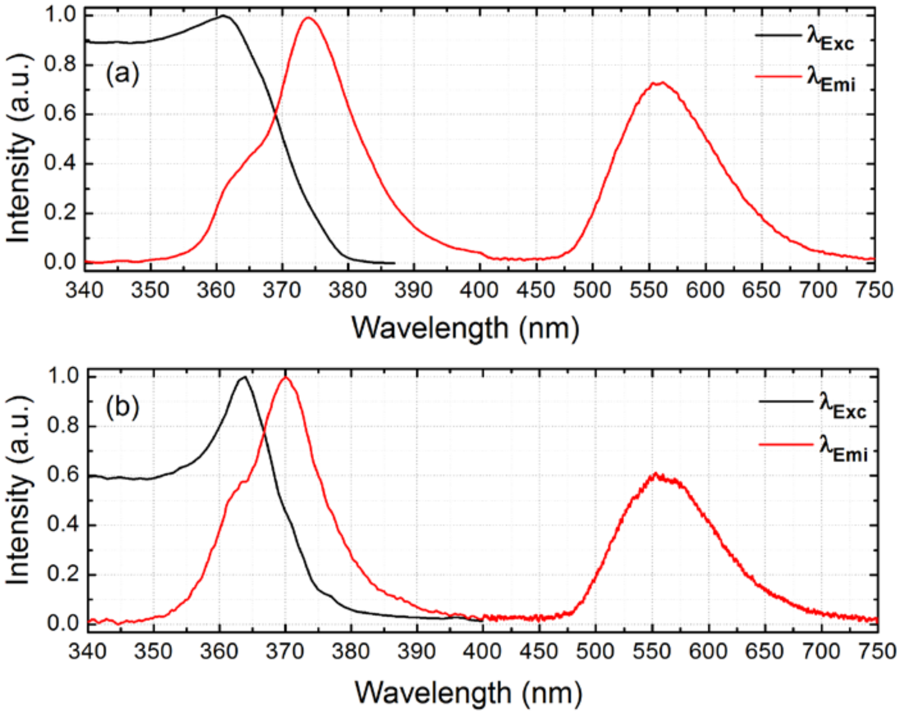

Figure 3.5. Photoluminescence and photoluminescence excitation spectra from 15 µm micro-pyramid from a) larger samples b) smaller samples. Red solid line shows the photoluminescence spectra for above band gap excitation and black solid line shows the steady state excitation spectra for yellow luminescence peak.

Optical properties of GaN micro-pyramids were studied using single photon excitation to understand the light emission from these structures before proceeding with nonlinear optical studies. Figure 3.5 represents the photoluminescence excitation (PLE) spectra (black line) and photoluminescence from both the GaN pyramid samples. The PLE spectra was taken by scanning for the excitation energies for a fixed emission energy at 560 nm. PLE spectra helps to understand the absorption edge of the GaN pyramid samples. Details of the PLE measurement is given in chapter 2. The absorption edge of both samples were estimated to be approximately at 360 nm. Excitation wavelengths closer to 360 nm gave the brightest yellow emission intensity from the GaN samples.

Single photon excitation above bandgap was achieved using the 325 nm (3.81 eV) wavelength from a continuous wave (CW) helium-cadmium laser. The ambient temperature CW photoluminescence (PL) spectra of both the GaN micro-pyramids are shown by the red solid lines in figures 3.4 a and b. The carrier densities were estimated using[44]

$$N_0 = (1 - R_n) f (\frac{\propto}{h\vartheta}) \qquad (3.1)$$

where $R_n = 0.2$ is the normal incidence reflectivity $h\vartheta$ is the incident pump energy in Joules, $\propto$ is the linear absorption co-efficient at 325 nm equal to 1.0 x 10^5 cm^{-1} (45) and $f = 1.3$ x $(\frac{E}{\pi \omega_0^2})$ is the effective incident pump fluence, where E = 10 mJ is the energy per pulse just before sample and ω_0 = 50 µm is the focused Gaussian beam radius. The carrier densities were estimated to be 2 x 10^{21} cm^{-3} for 325 nm excitation which is greater than the equilibrium density (n = 5 x 10^{18})[46].

The light emitted shows an asymmetric peak centered at 374 nm (3.32 eV) with a shoulder at 362 nm (3.43 eV) for larger pyramids. In case of smaller pyramids, the asymmetric peak was centered at 370 nm (3.35 eV) with a shoulder at 364 nm (3.41 eV). Similar observation was made from the sidewalls of the pyramid observed by X. Li et al[47]. This shoulder peak at ~365 nm is attributed to band-to-band recombination at room temperature, whereas the peak at ~374 nm may be caused by electro-hole plasma (EHP) emission[46,48–50]. A broad visible band centered at

560 nm (2.21 eV), commonly referred to as the yellow luminescence band is also observed and is due to recombination involving shallow donors and deep acceptors most likely due to Ga vacancies[51]. The slight red shift in UV peak in larger pyramid samples from 3.35 eV in smaller pyramids can be attributed to variation in strain present[52] or geometrical size affecting cavity modes[47] or a combination of both.

3.3.2.2 Nonlinear Optical Light Generation Larger GaN Micro-Pyramids

Figure 3.6 represents the spectra of nonlinear light generated by the larger GaN pyramids pumped by a femtosecond near IR laser at 720 nm, 770 nm, 840 nm and 900 nm (1.72 eV, 1.61 eV, 1.48 eV and 1.38 eV) wavelengths from the same spot at the apex of the pyramid at constant power. The multi-photon emission generated by all the excitation wavelengths contain the same UVL and YL peaks at ~ 375 nm and 560 nm, respectively similar to the linearly excited PL. A relatively less intense peak was observed at 440 nm which is attributed to the presence of Zn impurity. This occurs due the contamination of MOCVD chamber with minor amounts of Zn contents. As the energies of the excitation photons are well below the bandgap of GaN, the observed luminescence bands are due to multi-photon excitation which involves the simultaneous interaction of two or three identical photons with the material producing an absorption event equivalent to that of a single photon having twice or thrice the energy. Since the luminescence peak positions are same as that of a single photon excitation, we believe that the same recombination mechanism is involved in the emission process. The UVL and YL peaks can be classified as incoherent radiation process, while the narrow SHG peak is a coherent radiation process.

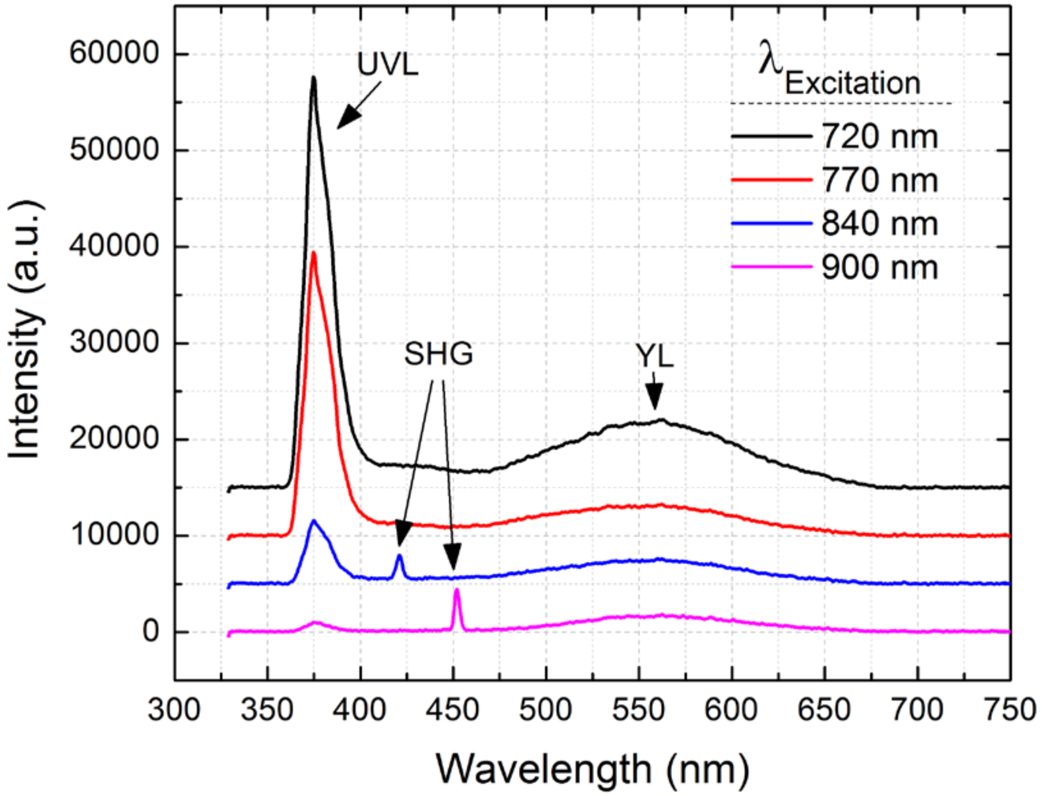

Figure 3.6. Multiphoton induced nonlinear light generation spectra excited by a femtosecond laser at 720 nm (black), 770 nm (red), 840nm (blue) and 900 nm (majenta) at constant power from the apex of a micro-pyramid. The average excitation power used for all excitations were same at 30 mW. All spectra were measured at ambient temperature.

During the measurement of NLO spectra from these samples, a variation in the radiation spectral profile was observed depending on the spatial excitation along the symmetric axis of the micro-pyramids. In the bottom one-third of the pyramid, the SHG peak was comparatively brighter than the MPL peaks. It was determined that the pyramid geometrical shape influences the NLO light generation and can be used to control the NLO processes contributing to the overall light generation as discussed in later sections.

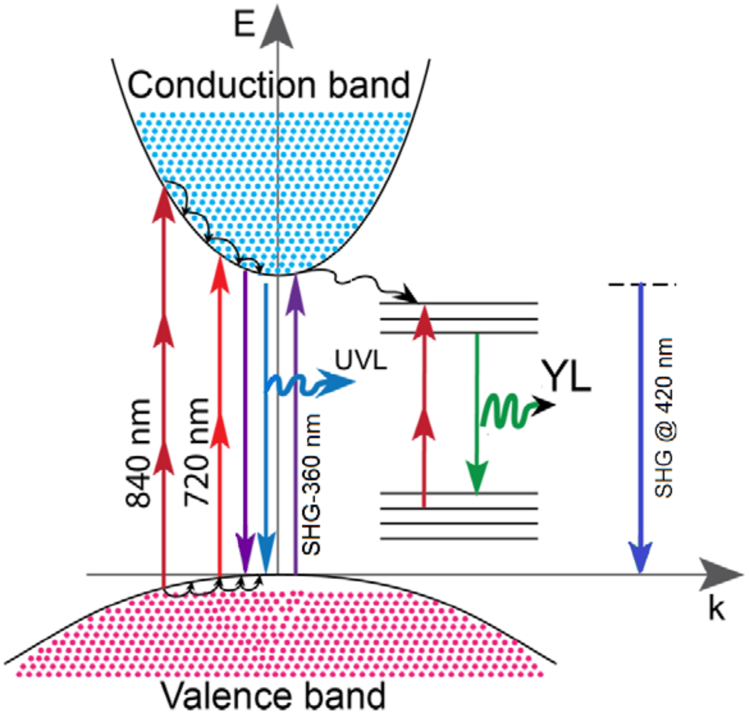

Figure 3.7. Schematic of a simplified band diagram depicting the nonlinear carrier transition processes observed in the bandgap of GaN resulting in incoherent ultraviolet and yellow emission as well as coherent second harmonic generation. Red arrows represent laser excitations, violet arrow represents SHG, blue arrow represents UV luminescence and green arrow represents yellow luminescence.

Figure 3.7 depicts the simplified energy-space diagram representing the nonlinear light generation processes. Comparing the UV emission peak wavelength to the near IR laser excitation wavelengths, one can notice that 720 nm excitation is less than twice the wavelength of the peak whereas excitations at 770 nm, 840 nm and 900 nm are more than twice but less than three times of the UV peak wavelength. From this comparison, we can conclude that the UV emission originates from a 2P absorption process for 720 nm excitation and from a 3P absorption process for 770 nm, 840 nm and 900 nm excitations. In the case of a 2P or 3P absorption process, an electron in the valence band absorbs two photons through states within the bandgap of the material, producing an absorption event equivalent to that of a single photon having twice or thrice the energy. The electron that was absorbed into the conduction band undergoes thermal relaxation via optical phonon scattering and generates spontaneous emission through radiative recombination with the holes in the valence band resulting in UVL in GaN pyramids. The efficiency of a 2PA process is higher than a 3PA process, which consequently results in a higher emission intensity of the UV luminescence due to 720 nm compared to 770 nm, 840 nm or 900 nm wavelength excitation as observed in figure 3.6. Moreover, the third-order interband nonlinearity is also maximum when the excitation wavelength is resonant to the bandgap of the GaN semiconductor. For excitations with wavelengths greater than 840 nm, we also observed a narrow peak at half the excitation wavelength (twice the incident frequency) indicating SHG process. The full width at half maximum (FWHM) of SHG peaks for excitations at 840 nm and 900 nm are measured to be 3.8 nm and 4.1 nm respectively, which is approximately equal to $(1/\sqrt{2})$ of FWHM of the transform limited band width of fundamental beam. It must be mentioned that that when the excitation energy is closer to half band gap energy of GaN, as seen in figure 3.6, a sharp peak becomes observable at ~375 nm in the UV peak especially for higher pump intensities.

The origin of multi-photon transition at various excitation wavelengths is investigated by power dependent measurements. The intensity of the nonlinear process on the incident pump density follows a power law;

$$I_{MPL} = I_P^n \tag{3.2}$$

where n is the number of photons required to induce the effect, I_{MPL} and I_p are intensities of emission and excitation, respectively. Therefore, to determine the photon contribution involved, intensity dependence of the UVL, SHG and YL as a function of incident power of the pump laser

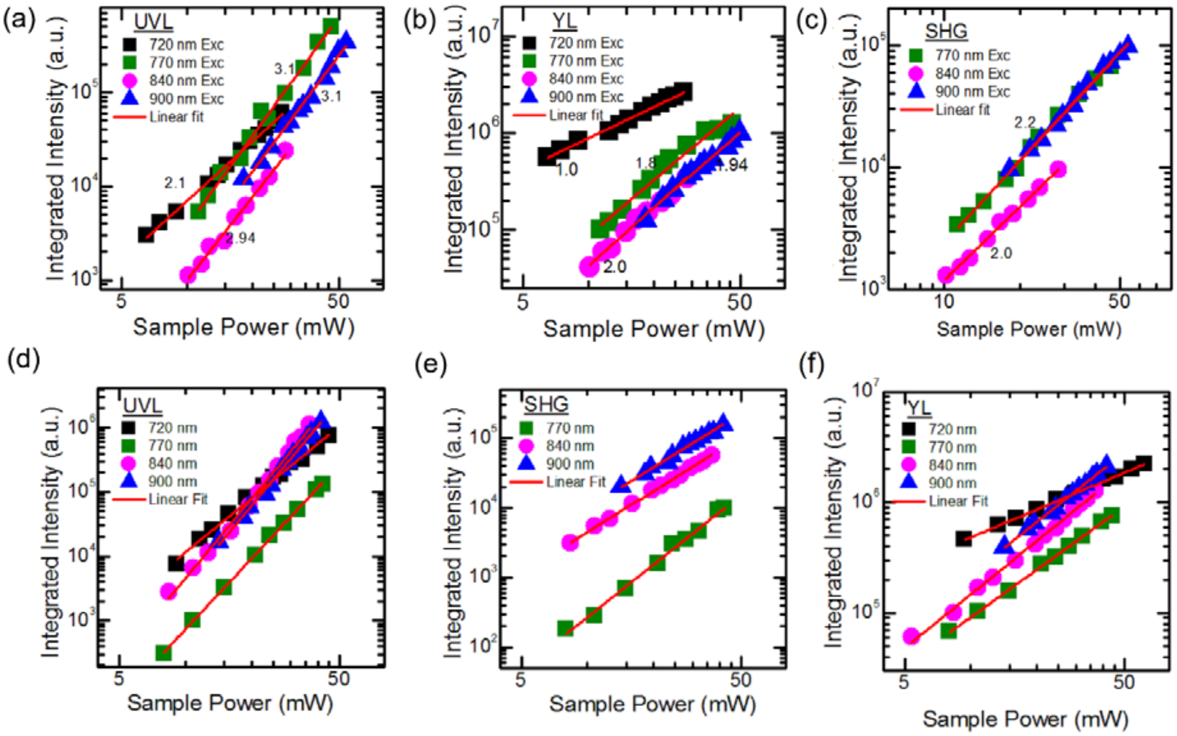

Figure 3.8. Excitation intensity dependence on SHG and multiphoton luminescence at the center (top row) and apex (bottom row). a and d) Ultra-violet luminescence peak dependence on 720, 770, 840, and 900 nm, b and e) yellow luminescence peak dependence on 720, 770, 840, and 900 nm, c) SHG dependence on 770, 840 and 900nm.

was measured and is plotted on a log-log scale in figures 3.8. As mentioned earlier, a spectral dependence on the geometrical cross section of excitation was observed. Hence, intensity dependent measurements were carried out at two excitation positions along the symmetric axis of the pyramid. The two luminescence bands exhibit different exponents for above and below $E_g/2$ excitation. It was observed that the power law exponent for the luminescence peaks showed a difference towards the apex position of the pyramid. To draw reliable conclusions, power dependent studies were performed over multiple days on at least six different individual pyramids and the results are deduced and is presented in figure 3.9.

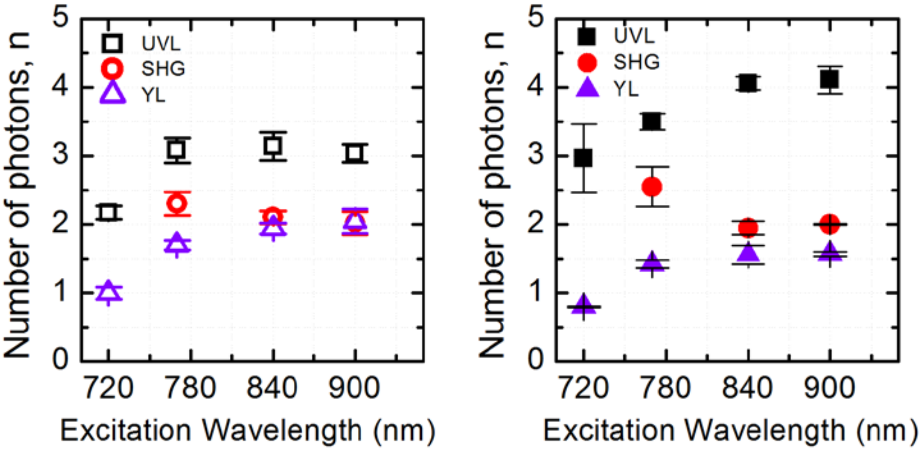

Figure 3.9. Power law exponent as a function of excitation wavelength. a) Number of photons involved in the transition as a function of excitation wavelength for UVL (black square), YL (purple diamond) and SHG (red circle) at the center of the symmetric axis averaged over six single pyramids, b) Number of photons in-volved in the transition as a function of excitation wavelength at the apex of the pyramid averaged over six single pyramids.

Figure 3.8 shows the NLO peak intensity dependence on the excitation power. This figure represents the intensity dependence from the bulk of the pyramid. For 720 nm excitation ($E > E_g/2$), power law exponent n ~ 2 indicates that the UVL band is induced by a two photon process; whereas, for 770 nm, 840nm and 900 nm, UVL band is induced by a three photon process as n ~ 3. Theoretical values of the exponent are 2 and 3 for 2PA and 3PA. This is reasonable considering the high power density achieved by tight focusing of the incident beam increasing the possibility of inter-band transitions to be excited via two or three photon absorption. Meanwhile, power law exponent shows that YL band is a consequence of a single photon process for 720 nm excitation and a gradual increase to two photon process for 900 nm excitation. This suggests a direct transition within the yellow band for 720 nm excitation and a two photon process 900 nm excitations contributing to luminescence as shown in figure 3.6. Broad band nature of YL reveals that phonon assisted carriers can increase the possibility of such transitions despite excitation with photons below the YL energy. Y. Toda et al[32] observed a similar behavior for YL from free standing bulk GaN with a thickness of 420 µm. For 720 nm excitation, they found n = 1.5, which was attributed to a combination of two processes; 1) a two photon excitation into the conduction band, where the excited carriers relax to the YL band emitting luminescence 2) a linear transition within the yellow band contributing to YL. In our case, the exponent value of n=1 suggests the presence of the latter case. This is believed to be caused by the linear (violet line in figure 3.7) absorption of the second harmonic signal (λ_{SHG} = 360 nm) created by the 720 nm excitation. PLE measurements for YL detection energy also shows the absorption edge to be around 360 nm. However, for excitation at 900 nm, YL band is purely due to a two photon process. For the excitation wavelengths in between 720 nm and 900 nm, a value of n ~1.7 show a complex process with dominant two photon contribution to YL. Efficient TPA in the YL band was observed in previous studies[15,32] because of the presence of deep level states at around ~1.3 eV above the valence band. Presence of such mid-gap states can enhance the probability of 2 photon absorption in the YL band. When the excitation wavelength is ≤ 720 nm, shallow levels can be directly populated by electrons in the valence band by means of linear absorption from SHG photons with a wavelength close to the absorption edge of GaN pyramids. When the excitation wavelengths much greater than 720 nm, the shallow levels can be directly populated by electrons in the valence band by means of coherent 2PA. For excitations at 770 and 840 nm, a combination of dominant 2PA in the YL band and the re-absorption of photons emitted due to the interband transition by the defect level states is likely to yield the observed exponents of 1.7 and 1.8 respectively.

The intensity dependence of the NLO radiation from the apex of the pyramid is presented in figure 3.8 and 3.9. Measurements at the apex were measured within 2 µm distance from the apex of the pyramid. The dimension of the apex of the pyramid as seen from figure 3.2d, is much smaller compared to the excitation wavelengths. The value of n for UVL was of an exponent higher than the value observed towards the center of the pyramid. The increase in power exponent could be a result of transition from EHP to stimulated emission, which is reasonable because the carrier densities created by the multi-photon excitation energies are of the order of 10^{22} to 10^{23} cm^{-3}. Pumping with a high intense laser beam can photo-induce carrier densities that can easily exceed the Mott density ($n = 1 \times 10^{19}$ cm^{-3}) in GaN at 300K[45]. As seen in figure 3.6, a narrow peak at the 375 nm UV peak is easily noticeable especially at the higher pump intensities used. A detailed observation and analysis of the said peak was limited by the resolution of the spectrometer. Also, localization of electric fields created by the tapered geometry of the pyramid at the apex can increase the nonlinearly induced dipole moments enhancing the nonlinear light emission[53]. As the exponent value increased for UVL, a reduction in the power exponent to YL peak was also observed due to a saturation of absorption in the YL band. A decrease in power exponent for YL at the apex for off resonant excitation energies confirms the presence of a complex emission process in the YL band. A significant deviation in the exponent for SHG at 770 nm, which is amplified at the apex could be due to resonant coupling of UVL and SHG. Phenomena such as resonant enhancement of SHG[54] has been reported in ZnO nanowires, where the strength of the frequency-doubled component is found to enhance while the two-photon absorption wavelength is tuned towards the exciton wavelength of the nanowire. Because of the overlap in UV emission and SHG peaks, errors in de-convoluting the SHG peak from UVL can contribute to uncertainty in the determined values of n.

3.3.3 Spatial Mapping Of Optical Nonlinearity In GaN Micro-Pyramids

Spatially resolved NLO spectral measurements and multi-photon imaging were performed to determine how dimensionality and crystal quality affects the MPL and SHG. Both SHG and MPL processes critically depend on the interaction/absorption cross-section of the medium. As the excitation volume changes from a few hundred nanometers at the apex to ~15 microns at the base of the pyramid, the light matter interaction is significantly modified by the shape and size of the GaN pyramid. The nonlinear optical signal generated from a single pyramid is therefore collected over the entire height of the pyramid to characterize the effect of the changes in structural composition and symmetry of the structure on the NLO processes within the GaN pyramid. Spatial measurements were made in the direction of the optic axis which was in the direction if the symmetric axis of the pyramid. Figure 3.10 represents the spatial measurements using 720 nm, 750 nm, 770 nm, 840 nm and 900 nm excitation wavelengths with same input power density.

The spatial measurements show significantly different profiles for resonant and off-resonant excitations. The integration times used for collecting spectra for 720 nm, 840 nm and 900 nm were kept constant; however, it must be noted that the integration times used for 750 nm and 770 nm were different from other wavelengths. Therefore, one must not try to compare the emission intensities between the spatial graphs. The results show significant UVL and YL throughout the pyramidal volume for resonant excitation at 720 nm with UVL being maximum at the apex of the pyramid. The YL intensity holds a uniform intensity profile throughout the pyramidal volume except for a small increase at the base. The increase in the structural defects at the base is the likely cause of the increased YL emission. Structural defects enhance second order nonlinearity[55] increasing the probability of second harmonic generation. With 720nm excitation, second harmonic signal is generated with a wavelength of 360nm, which results in linear absorption due to shallow donor-deep acceptor states explaining the increase in YL towards the base. Due to the complete absorption of SHG, it is not observable in the spatial spectrum. Furthermore, figure 3.9 c-d showing spatial mapping of NLO for excitations 750 nm and 770 nm confirms the presence of SHG in the lower one-third of the pyramid. Figures 3.10 c-f shows that as the excitation wavelengths is detuned from the resonance condition, the SHG generated is also detuned from the absorption edge of GaN and therefore the YL emission is created by a dominant 2PA process. Unlike 720 nm excitation, for excitations at 770 nm, 840nm and 900 nm, both second order and third order nonlinear effects can be observed at the apex of the pyramid (see figure 3.10 d-f). With 770 nm excitation, the SHG can be differentiated from the UVL at the apex. It is likely that SHG is present at the apex for 750 nm excitation; however, due to the overlap between SHG and UVL, it is not distinguishable. The intensity of both emission bands are higher at the apex and decreases towards the base of the pyramid. Second harmonic signal is also present at the apex; however, maximum intensity is observed towards the base. However, in the case of 770 nm excitation, figure 3.10d shows significant intensity for second harmonic signal likely due to resonance enhancement. For excitation powers below a threshold power of 10 mW, only SHG is generated in the bottom half of the pyramid structure for 840 nm and 900 nm excitation. From figure 3.10, it is clear that the second order nonlinearity is higher

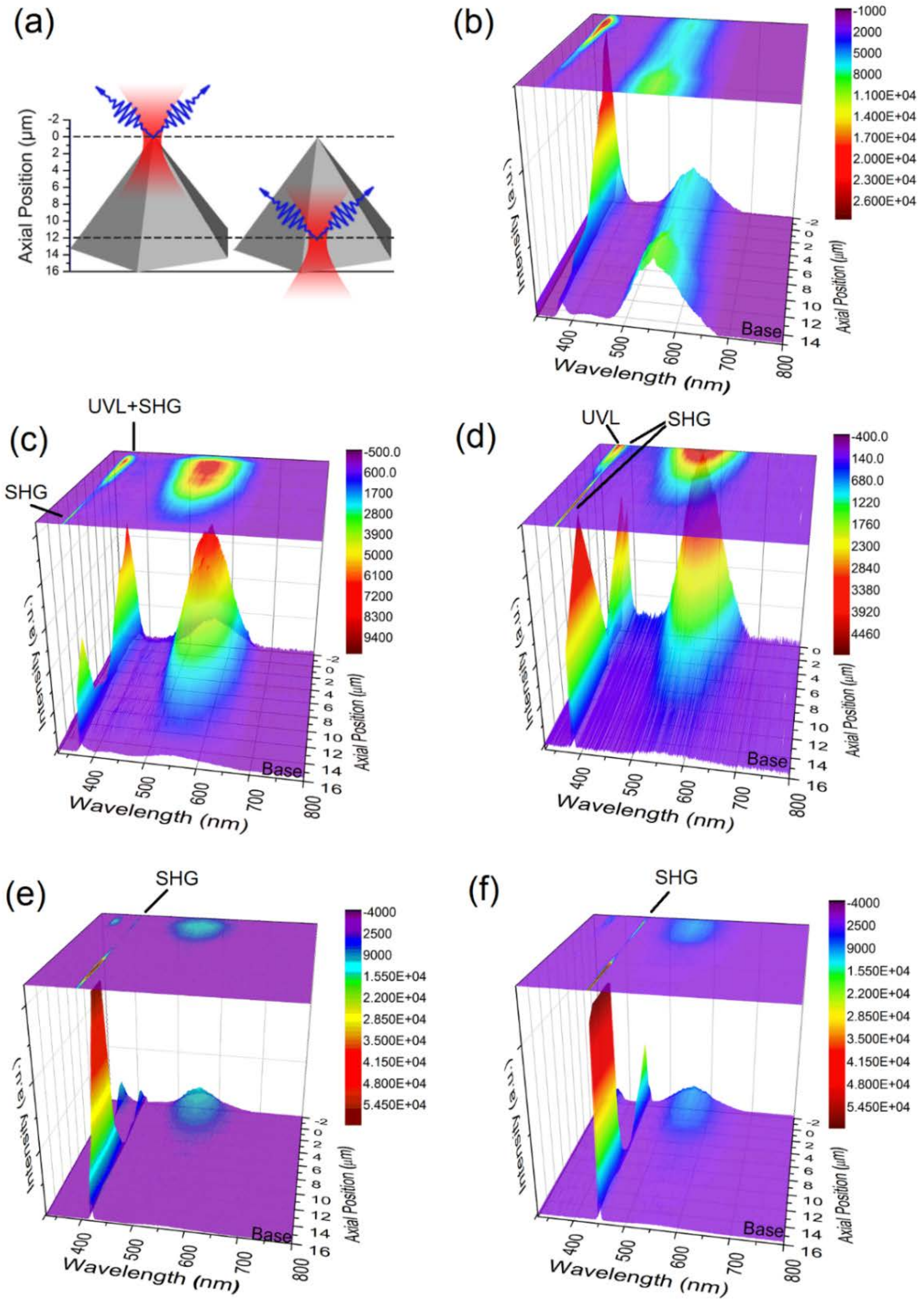

Figure 3.10. Three dimensional plots of line scan of MPL and SHG as a function of pyramid's symmetric axis. a) Two representative laser excitation positions along symmetric axis of the pyramid. Spatially dependent light generation from pyramid using wavelengths of b) 720 nm c) 750 nm d)770 nm e) 840 nm and f) 900 nm.

at a position 4-5 µm above the base, whereas third order nonlinearity is higher towards the apex. As seen from figure 3.2c, the dimension of the apex of the pyramid is of the order or less compared to the excitation wavelength. Also, GaN crystal quality is expected to be higher towards the apex of the pyramid than the base[25]. A combination of the geometrical effects increasing nonlinearly induced dipole moments, increased crystal quality and high carrier concentration are likely to enhance the emission signals at the apex. Detailed structural studies indicate that ELO grown GaN pyramids have comparatively lower defect densities; mostly, threading dislocations towards center core of the base; specifically, in the lower one third of the pyramidal height of the pyramidal volume (see section 3.3.1). Nearly defect free regions were observed in the lateral grown regions away from the mask openings[39]. Increase in SHG intensity towards the base can be attributed to three reasons; 1) the length of the micro-pyramid is within a few coherence lengths (~ 3 µm for GaN for 840 nm), 2) increase in defect density resulting in symmetry breaking thus increasing the nonlinearity at the center core of GaN pyramid, and 3) the semipolar facets of the high refractive GaN pyramid (n = 2.4-2.56) facilitates total internal reflection (TIR) of the incident infrared light and is ideal to form cavity resonators with high optical nonlinearity. It is highly unlikely that the contribution from symmetry breaking due to defect density to the enhancement in SHG is significant. A comparison to nonlinear emission spectra of a 5 microns thick GaN epi-layer with sufficient defect density is performed to validate the significance of contribution to the SHG enhancement as shown in figure 3.11. Furthermore, NLO light generation was observed for lower input powers such as 2-5 mW, whereas no NLO light generation was observed from the GaN epilayer between the micro-pyramids. Therefore, the increase in SHG intensity is believed to be caused by the formation of a TIR assisted quasi phase matching inside the micro-pyramid cavity.

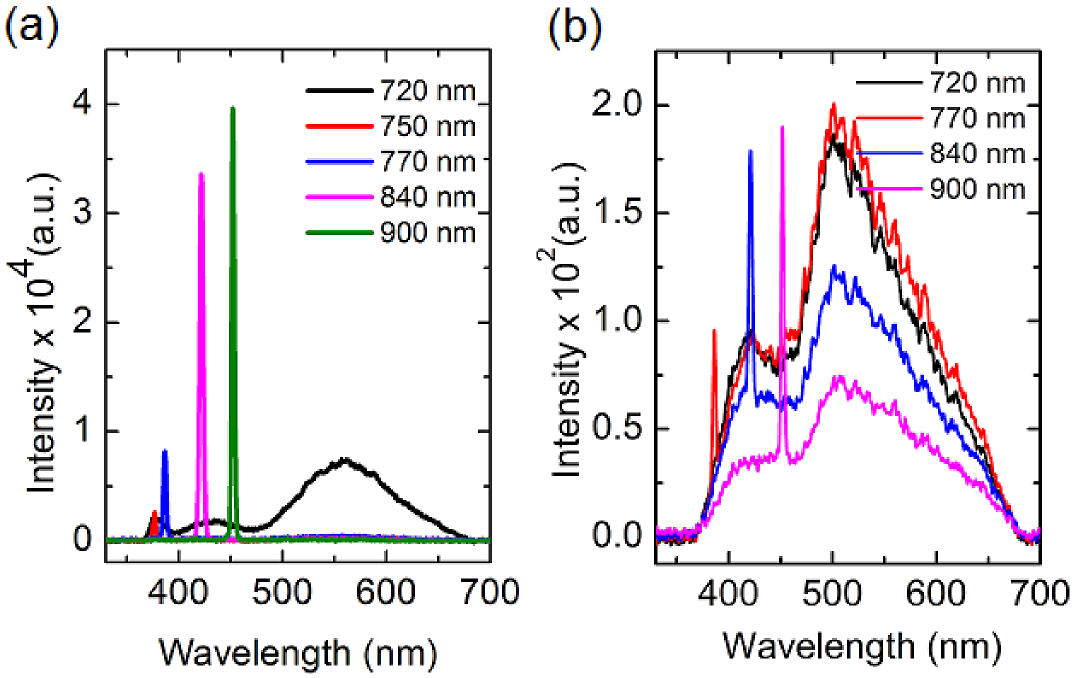

Figure 3.11. Comparison of the nonlinear spectra from (a) micro-pyramids and (b) GaN epi-layer excited with various laser excitations wavelengths at 25 mW power.

3.3.4 GaN Micro-Pyramid as a Hexagonal Micro-Cavity for Nonlinear Light Generation

Selectively grown GaN micro-pyramids with extremely smooth semipolar facets can function as tunable micro-cavities for the control of nonlinear optical (NLO) radiation. Optical microcavities such as photonic crystal cavities[56], ring resonators[57], toroidal microcavities[58] and crystalline whispering gallery mode (WGM) cavities[59] facilitate the study of new and interesting linear and nonlinear properties of light matter interaction. Cavities made of wide band gap crystalline semiconductors would be ideal for frequency conversion of communication wavelengths because of their low absorption loss in this color regime. Such cavities generally possess high refractive index and creates total internal reflection (TIR) at the facets. These cavities are called open resonators because the contrast in refractive index at the facet-air boundary is relatively less as compared to a metallic coated cavity. When the cavity is a perfect circle, ideally WGM modes are excited. When the cavity shape deviates from circle to polygon, quasi-WGMs are excited[60]. Crystalline semiconductors with high refractive index support so-called Quasi-WGM modes that exhibit an ultrahigh-Q[61]. In a hexagonal cavity, light propagates in a circular direction while being totally internally reflected by the crystal facets. The hexagonal cross-sections of ZnO and GaN rods have shown to confine micro-cavity modes for light trapped under appropriate conditions[62,63]. These hexagonal micro-cavities have sustained the formation of whispering gallery modes (WGM) due to total internal reflection (TIR) from the facets[64] as well as Fabry Perot modes in the longitudinal plane between the top and bottom facets[60]. Figure 12 shows the schematic of optical paths within a hexagonal microcavity. The hexagonal micro-cavity favors modes with 60^{o} angle of incidence within the cavity and reduces the mode degeneracy that can also result in non-WG modes such as the six bounce modes[65]. The modes confined in a hexagonal micro-cavity are localized close to the facet surface of the resonator; hence possess small volumes. The high Q-factor and small interaction volume yields very high nonlinear conversion efficiency in hexagonal resonators[66].

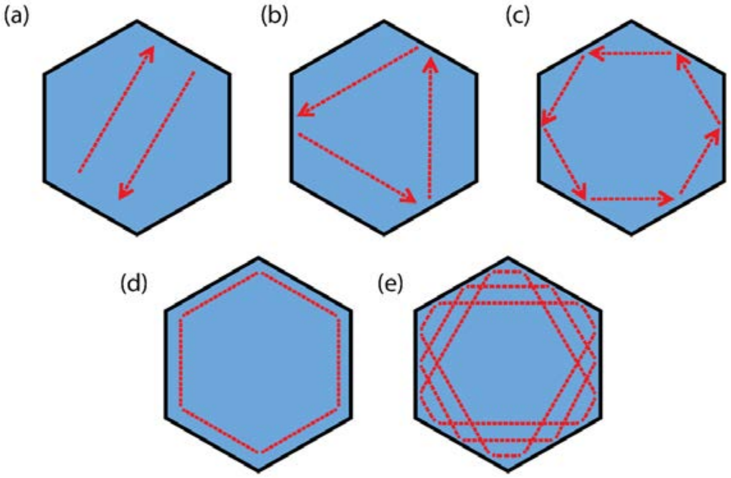

Figure 3.12. Illustrations of optical rays showing possible resonant cavity modes in a hexagonal geometry. (a) Fabry-Pérot modes. (b) Quasi-WGM (c) WGM (d) Perturbed WGM (e) Higher-order quasi-WGM [Figure adapted from ref 59].

GaN being a wide band gap semiconductor with high refractive index (n ~ 2.52), the pyramid shaped GaN crystals create micro-cavities that are ideal for TIR between the $\{1\bar{1}01\}$ facets. For GaN, the smallest critical angle of TIR is ~ 30^0. The $\{1\bar{1}01\}$ facets are about 62^0 with the substrate; therefore, TIR can be easily achieved. The extremely smooth surface morphology of the structure is essential for the wave guiding performance without large losses from the surfaces. The mode selection rules or the phase matching conditions in hexagonal resonators are significantly more relaxed compared to free space[67]. Hence, it results in a wider tunability of the fundamental mode at the SHG frequency in the hexagonal resonator that is not feasible in bulk crystals. Hexagonal semiconductor cavities with varying diameters allows confinement of different WGM[64,68,69] modes. This tells us that the shape and size of these wide bandgap nano- and micro-structures are very critical in realizing cavity modes. Tapering of the cavity size enables the modulation of the wavelength of the cavity modes and the order of resonance to be modulated[64]. The apex of GaN pyramids scales down to a few nanometers and the multiphoton transition induced band-to-band excitons can be strongly confined at these tips. The spatial inhomogeneity of GaN pyramid in the axial dimension compared to the hexagonal rods and disks provides intrinsic variation of cavity cross section which makes them ideal candidates for observing cavity modes in a broad band range. Although, open resonators generally belong to low Q cavities, their value cannot be underestimated as cavity engineering and advanced growth techniques can produce moderate quality emitters that find quite usefulness in many photonic applications.

Multi-photon imaging of the nonlinear light generation process from the micro-pyramid is presented in figures 3.13 and 3.14. Figure 3.13 shows a montage of images taken from various axial cross-sections showing the MPL and SHG as a function of excitation along the symmetric axis of the pyramid at two different pump powers. The excitation wavelength used was 840 nm. By comparing figures 3.10e and 3.13, it can be observed that MPE induced spontaneous UVL and YL dominates the emission from the apex of the GaN pyramid. For excitation depths at around 2-3 microns into the pyramid, the effective emission is dominated by YL. At higher pump intensity (Figure 3.13 b), the UVL intensity increases relatively to the YL intensity and results in a relatively cool-white emission at the apex. A variation in the axial excitation cross section accompanies a variation in the diameter of the hexagonal cross section due to the geometry of the pyramid. While the spontaneous emission due to UVL decreases within the cross-section of the pyramid with larger radius, one can observe formation of stable modes at the mid-point of the $\{1\bar{1}01\}$ facets of GaN. At about 4-5 μm above the base, one can see the formation of cavity modes with a six-dot pattern. The SHG modes appear to be confined tightly in a small mode volume close

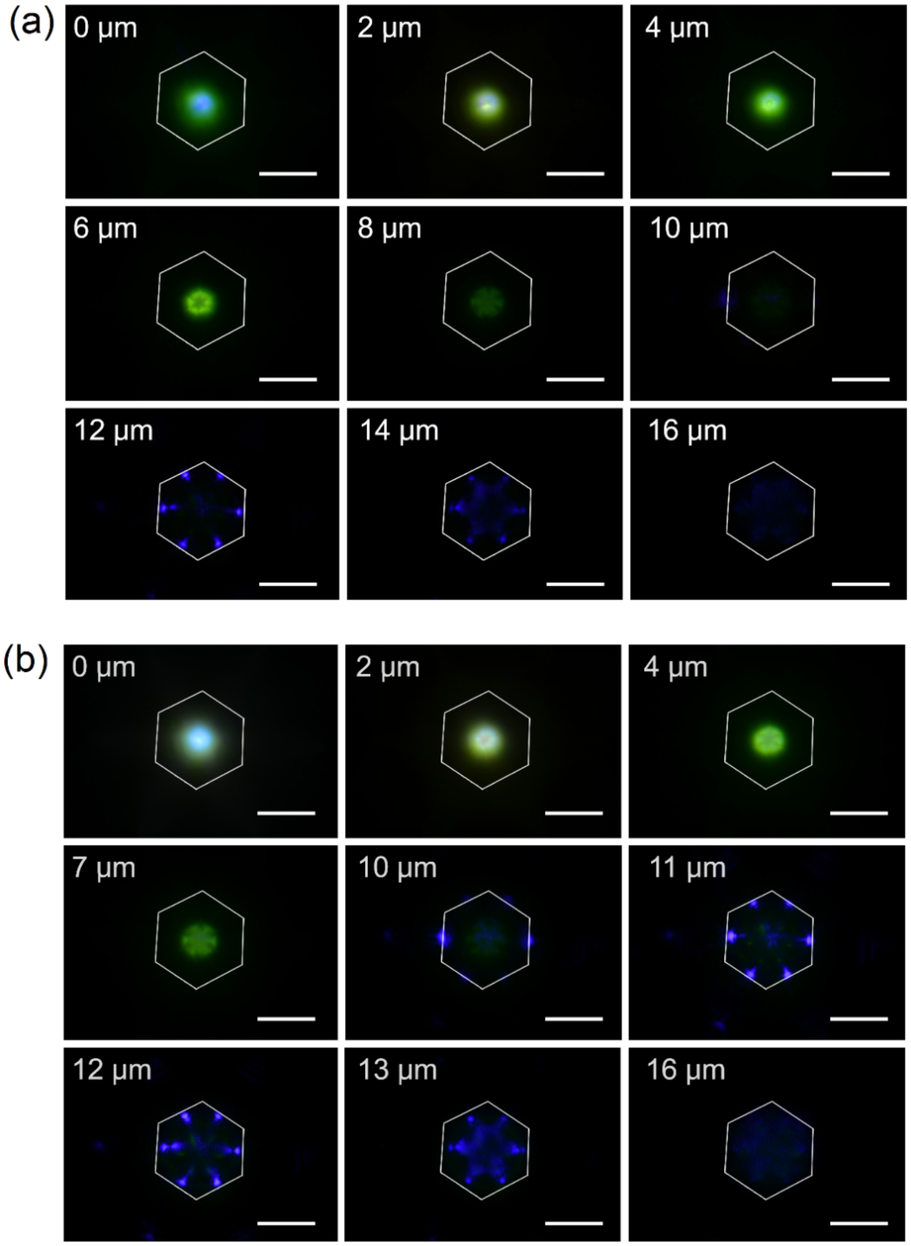

Figure 3.13. Images of light emission from a GaN micro-pyramid with excitation at 840 nm from the same pyramid (a) 15 mW power at the sample. (b) 30 mW power at the sample. 0 μm is apex, 16 μm is base. Image labeled 11 μm in 13 b generates a spectrum that similar to the majenta curve in figure 11a. White hexagon outlines the pyramid base. Scale bar represents 10 μm.

to the facet of the pyramid at a depth of 11-14 μm from the apex, where the SHG intensity is observed to be maximum. It happens that this axial position corresponds to four times the coherence length of GaN at 840 nm pump beam. Therefore, TIR assisted quasi phase matching is probably contributing to stable SHG modes. Because the refractive index of GaN is larger than air, the generated SHG at 420 nm is confined within the pyramid by TIR, where the relative refractive index is defined as $\tilde{n} = n/n_0 > 1$. The mode of frequencies trapped in the pyramid are similar to the quasi-WGM modes. It can be observed in all the images of the GaN pyramid (Figures 3.13a and b).

For depths exceeding 10 microns, the generated second harmonic signal have 6 reflections with identical path length ($S_6 = 3\sqrt{3}Rn$) and with a 60° angle of incidence to the facet normal. Sharp six-dot mode formation was confined into an axial cross-section of roughly 3 µm. The number of modes at the second harmonic frequency confined within the cavity decreases away from the optimal position in the axial direction. Any dissipation due to excitonic or the band gap states destroy the cavity mode confinement. As mentioned earlier, the phase matching condition in hexagonal structures are relatively more relaxed. A closer observation of the confined modes at high pump intensities shows additional modes with varying radius. The SHG modes appear to be confined inside the cavity, while the modes from the multiphoton process extend outwards (see bottom row of figure 3.14). In a hexagonal resonator, the contribution due to geometrical dispersion results is a negative Δn, where $\Delta n = \tilde{n} - n$. The optical field concentrated inside the hexagonal resonator is usually located at some distance away from the facet due to dispersion. The optical path length is shorter than $3\sqrt{3}Rn$ due to this geometrical dispersion ($d\Delta n(\lambda)/d\lambda < 0$). Therefore, at longer wavelengths more of the optical power is carried by the evanescent field outside the resonator and thereby reducing the effective refractive index. Consequently, the effective radius of the SHG mode is smaller than the UVL mode, which forms closer to the facet. However, as we move closer to the substrate the SHG intensity is reduced due to weaker confinement of the cavity mode as the electromagnetic waves are evanescently leaked out into the GaN/SiO2 interface layers at the base. Also at the apex of the pyramid, the sharp edges of the hexagonal faces result in leaky modes and reduces the confinement of the SHG signal confined within the cavity. However, it was observed that the SHG intensity is higher at the apex relative to the SHG intensity at the center possibly due to the tip enhancement effect.

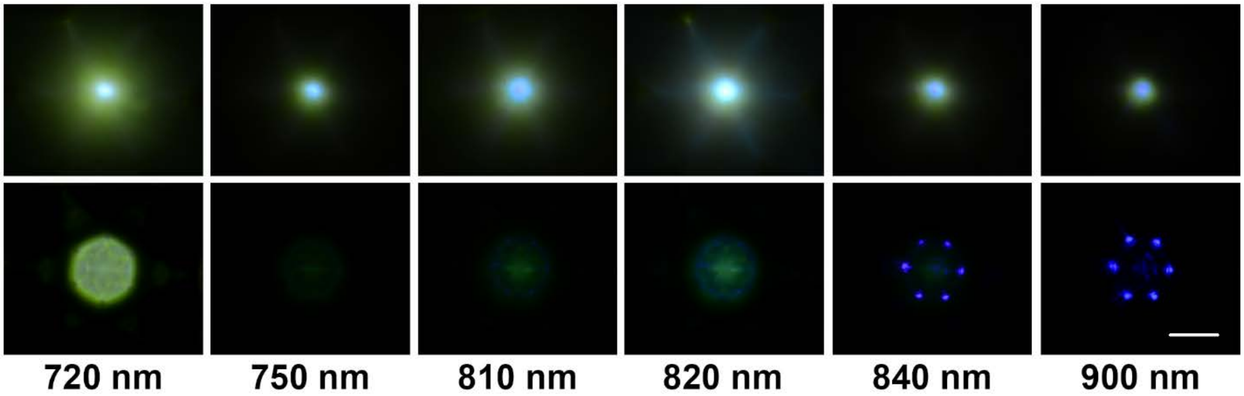

Figure 3.14. Images taken from a GaN micro-pyramid at various excitation wavelengths at ~ 0 µm (top row) and ~11 µm position (bottom row) shows apex and bulk emission. Please note that the pump density used were roughly twice for 810 nm and 820 nm. Pumping density for the rest of the excitaion wavelengths was kept constant at 30 mW.

Figure 3.14 shows the images taken from a GaN micro-pyramid at various excitation wavelengths from the apex and ~ 11 µm into the bulk of the pyramid. The optical nonlinearity is maximum at the resonance when the fundamental or the generated frequencies are tuned to the bandedge or the excitonic level of the semiconductor. Although non-resonant optical nonlinearity is relatively small for second harmonic waves below the bandgap or the excitonic states; they undergo very small attenuation. The less attenuated modes of the hexagonal resonators provide the photons confined in the cavity a better probability to interact without being absorbed or dispersed. Although SHG was observed for pump wavelengths slightly deviated from the resonance levels of GaN band gap, the six-dot pattern was observed only for off-resonant pump wavelengths longer than 810 nm (see Figure 3.14 b). The SHG orbiting around the perimeter of the hexagonal cross section can be clearly seen for 810 and 820 nm excitations (see bottom row of figure 3.14).

Fast Fourier transform of the spatial frequency distribution from the images was performed and analyzed to understand the degree of coherence of the confined modes within the micro-pyramid. Figure 3.15a presents the FFT spectrum as a function of the pyramid's symmetry axis for 840 nm excitation wavelength. It can be seen that for axial positions corresponding to an incoherent process, a relatively broad peak is observed, whereas, interference pattern was observed for axial positions with coherent radiation. It shows that the micro-pyramid cavity confines cavity modes at the axial positions where the six-dot pattern at the facets are observed. These quasi-WGM modes exhibit an ultrahigh-Q ($Q = \frac{\lambda}{\delta\lambda}$) as observed from the FFT analysis and contributes to enhanced SHG within the pyramid. Such an effect can be attributed to the pyramidal shape of the GaN micro-structure as no mode confinement due to cavity modes are observed in the reference GaN micro-pillars under our experimental condition. Figure 6 shows that the SHG efficiency is relatively higher for a fundamental excitation wavelength of 900 nm compared to 840 nm. A closer analysis of the mode confinement as represented by figure 15c shows that the number of second harmonic modes confined due to excitation at 900 nm is more than at 840 nm for the same pump power.

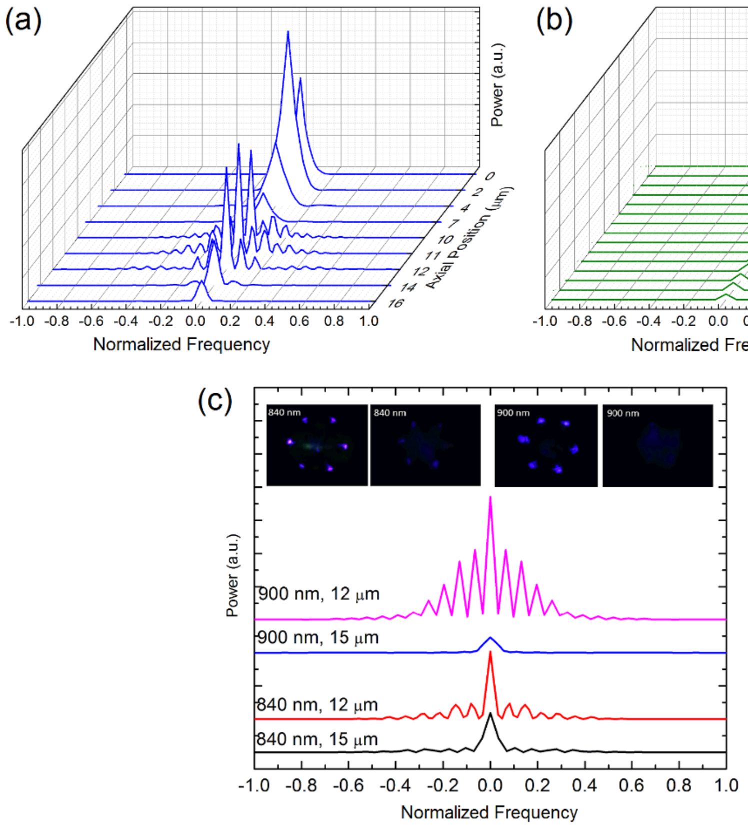

Figure 3.15. Interference pattern in the axial direction of the GaN micro-pyramid for excitation at a) 840 nm and b) 720 nm, c) Two representative positions at 840 nm and 900 nm. Six-dot pattern corresponds to 12 µm axial position. X and y ordinates show normalized frequency and power, respectively.

3.3.5 Micro-Pyramid Size Effects on Cavity

As mentioned in section 3.2, GaN micro-pyramids with 3 µm height and diameter, respectively was also studied. The inhomogeneity in dimension of this sample contributed to some technical difficulties as in positioning the pump laser beam on the symmetric axis. Nevertheless, NLO light intensity along the optic axis/ symmetric axis of the micro-pyramid was measured and two-dimensional plots of the same is presented in figure 3.16. Multi-photon induced luminescence peaks at the UV and YL region were observed similar to the larger pyramids. UVL was observed to be maximum at the apex of the pyramid. The intensity of YL peak was relatively higher in the smaller pyramids. The overall axial luminescence intensities seemed similar to the larger pyramids, except for the omnipresent YL. In the case of larger pyramids, axial variation along with optimum pump wavelength and power could completely turn off the YL in the bulk of the pyramid. However, in the smaller pyramids, for off-resonant excitation, significant YL although appears to be higher towards the apex is present throughout the pyramid volume. The axial position of maximum SHG in the backward direction was not successfully determined because of the inhomogeneity in the convergence of facet edges at the apex (see figure 3.3b), resulting in slight deviations in the positioning of pump beam producing varying results.

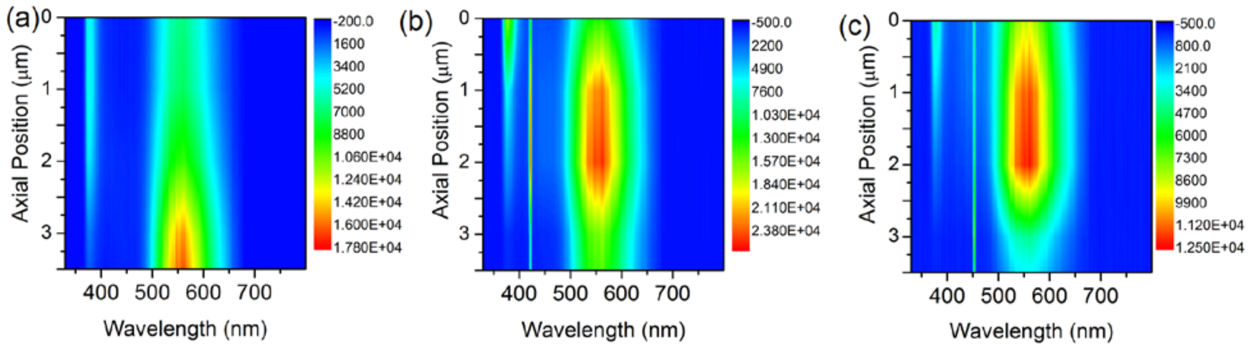

Figure 3.16. Two dimensional plots of line scan of multi-photon induced luminescence and second harmonic genera-tion as a function of pyramid’s symmetric axis. a) 720 nm excita-tion, b) 840 nm excitation and c) 900 nm excitation.

Imaging of the nonlinear light generation process from the smaller micro-pyramid is presented in figure 3.17. Images are taken from various axial cross-sections showing MPL and SHG as a function of excitation along the symmetric axis of the pyramid at two different pump powers. By varying the dimensions of the micro-cavity emitters, highly directional SHG light can be redirected from the generated emitter to surrounding ones. This can be visualized in image labeled 2 µm in figure 3.17 b.

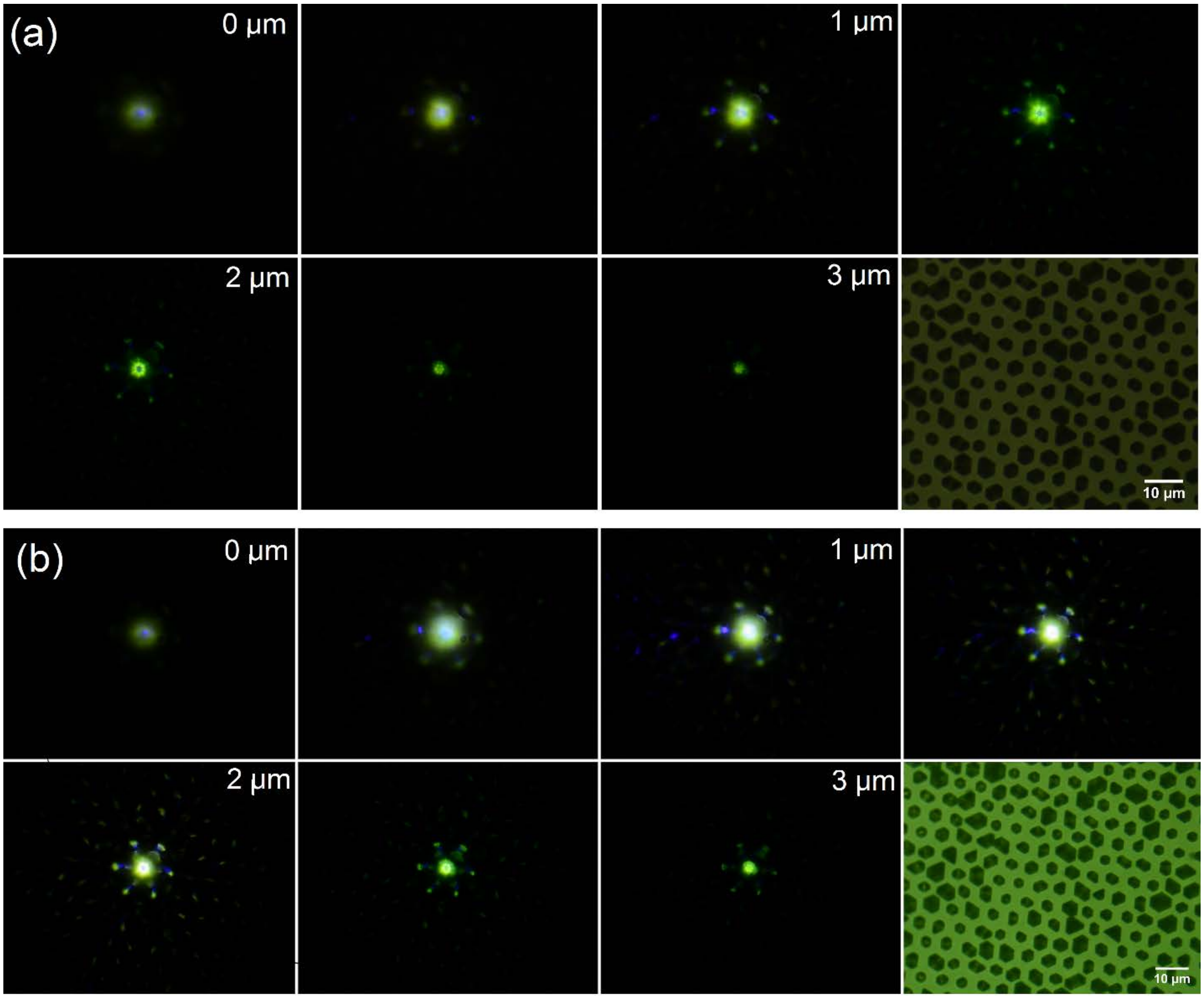

Figure 3.17. Images of nonlinear light generation from a 3 µm GaN pyramid with excitation at 840 nm from the same pyramid (a) 15 mW power at the sample. (b) 30 mW power at the sample. Images are taken at 0.5 µm increments in the axial direction. 0 µm is apex, 3 µm is base. Unlabeled images are in 0.5 increments. Scale bar represents 10 µm.

From figure 3.18, it can be seen that the 15 µm confines the quasi-WGM modes whereas in the smaller pyramids the modes are not confined. The SHG created in the bulk of the smaller pyramid leaks out of the facets and propagates out via the surrounding pyramid scatterers. In the case of 15 µm pyramid, the six modes are created about 30% length above the base of the pyramid.

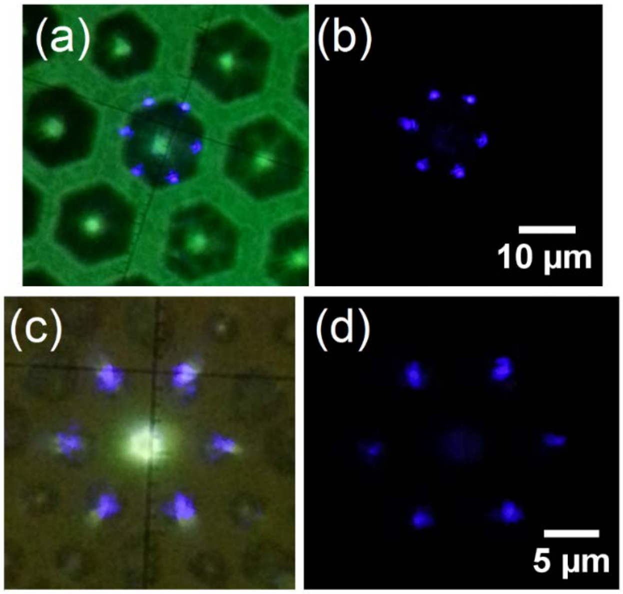

Figure 3.18. Optical images of nonlinear light generation from the 15 µm and 3 µm GaN pyramids. (a) and (c) are the bright field images, (b) and (d) are the dark field images of the filtered SHG.

3.3.6 SHG Efficiency

The average powers of incident and SHG fields were measured and the experimental second harmonic conversion efficiency of the 15 µm pyramid was estimated. The SHG power was measured as a function of the incident pump power at the 12 µm position on the symmetric axis of the pyramid, where maximum intensity of the SHG signal was observed. The measurements were made at an incident fundamental wavelength of 840 nm. The MPL contribution was filtered using a 420 nm interference filter with a band width of 10 nm. Figure 3.19 depicts the efficiency of the SHG process, η, as a function of the incident pump power. The SHG efficiency is estimated as $\eta = P_{2\omega} / P_{\omega}$ where $P_{2\omega}$ and P_{ω} are the measured average powers of the SHG and incident pump beams. The scattering of fundamental and SHG beams were not included in this estimation. Figure 3.19 shows that the SHG efficiency scales linearly with the incident pump power. A conversion efficiency of 1.1×10^{-7} was obtained towards the base of the pyramid for a pump power of 24 mW compared to 1.4×10^{-5} (at 21 mW) obtained from ZnO nanorods10, 1.8×10^{-9}

(at 3 mW) from Au coated silica nanoparticles[70], and 2.4 x 10^{-9} (7 mW) for a GaN two dimensional photonic crystal[12].

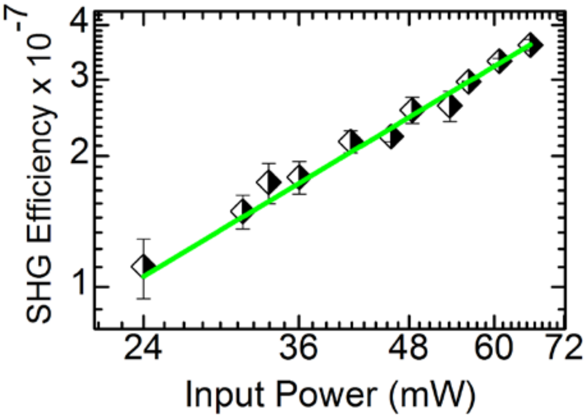

Figure 3.19. SHG efficiency, η, of 15 um GaN pyramid at 420 nm as a function of incident pump power at 840 nm.

3.4 Conclusions

GaN micro-pyramidal structures of two different dimensions with $\{1\bar{1}01\}$ facets were formed on patterned substrates by MOCVD using ELO growth technique. NLO light generation was observed in pyramids for excitation wavelengths 720 nm to 900 nm, which was limited by the pump laser. Multiphoton transition induced by tightly focused femto-second NIR radiation results in UVL due to EHP and defect level mediated YL from GaN micro-pyramids. Band edge UV luminescence and yellow luminescence from GaN micro-pyramids were observed under femtosecond IR radiation with energies below and above the half bandgap energy. SHG was also observed from these pyramids for excitation below the band gap energy. The MPL due to 2PA is stronger at the interband resonance when the energy of incident field corresponds to half the bandgap energy of GaN. The pump intensity dependence on PL shows nonlinear behavior in the absorption process and the number of photons involved in the transition depends on the excitation energy and geometrical position on the micro-pyramid. A quadratic dependence was observed confirming SHG process, which was observed to have maximum intensity at about 4-5 µm above the base of the 15 µm pyramid. The results indicate that GaN micro-pyramids have large optical nonlinearity due to dimensional effects, crystalline quality and cavity formation. However, for 3 µm pyramids, the six bounce modes observed was not confined within a pyramid. In the case of 15 µm, second order nonlinearity is larger where the cavity modes are confined. Maximum SHG generation in the 3 µm pyramid was unable to determine due to the inhomogeneity of the structures. The larger GaN micro-pyramids allows the control of color temperature and coherence of the light generation by selective onset of the nonlinear process by varying axial excitation of the pyramidal cross-section. In the case of smaller pyramids, no discrete control of the second and third order processes were observed. The NLO light generation is controllable by controlling the incident laser energy and intensity in the case of both pyramids. Quasi-WGM like modes in 15 µm pyramid were observed only for off-resonant excitations. The axial inhomogeneity in the micro-pyramid provides hexagonal cross-section slices with varying diameters offering flexible WGM conditions for a range of wavelengths. Any WGM modes formed in a hexagonal cavity is confined in the horizontal plane of the cross-section and is unlikely to be detected in the c-direction of the crystal. The pyramidal shape with inclined facets allows the detection of such modes. Ideally confined WGM modes require a coupled waveguide to extract the light out. Cavity formation along with NLO light generation and controlled growth of GaN based micro-pyramids shows potential for all optic circuitry applications. Also the efficiency dependence of UVL on the pyramid geometry were found to follow the same trend for both pyramids. The efficiency of SHG signal on the axial position was hard to determine as the directionality of SHG highly depended on positioning the pump beam on the symmetric axis of the pyramid; hence the change in collection efficiency made it difficult to correctly estimate the spatial position for maximum SHG intensity. In addition, light generation from the smaller pyramid array created interesting optical scattering patterns that could potentially be used for further studies to manipulate the NLO processes for photonic applications.

3.5 References

(1) Hong, Y. J.; Jeon, J.-M.; Kim, M.; Jeon, S.-R.; Ho Park, K.; Yi, G.-C. Structural and Optical Characteristics of GaN/ZnO Coaxial Nanotube Heterostructure Arrays for Light-Emitting Device Applications. *New J. Phys.* **2009**, *11* (12), 125021.

(2) Lundskog, A.; Hsu, C.-W.; Fredrik Karlsson, K.; Amloy, S.; Nilsson, D.; Forsberg, U.; Olof Holtz, P.; Janzén, E. Direct Generation of Linearly Polarized Photon Emission with Designated Orientations from Site-Controlled InGaN Quantum Dots. *Light Sci. Appl.* **2014**, *3* (1), e139.

(3) Consonni, V.; Sarigiannidou, E.; Appert, E.; Bocheux, A.; Guillemin, S.; Donatini, F.; Robin, I.-C.; Kioseoglou, J.; Robaut, F. Selective Area Growth of Well-Ordered ZnO Nanowire Arrays with Controllable Polarity. *ACS Nano* **2014**, *8* (5), 4761–4770.

(4) Hersee, S. D.; Sun, X.; Wang, X. The Controlled Growth of GaN Nanowires. *Nano Lett.* **2006**, *6* (8), 1808–1811.

(5) Li, S.; Waag, A. GaN Based Nanorods for Solid State Lighting. *J. Appl. Phys.* **2012**, *111* (7), 71101.

(6) Nakayama, Y.; Pauzauskie, P. J.; Radenovic, A.; Onorato, R. M.; Saykally, R. J.; Liphardt, J.; Yang, P. Tunable Nanowire Nonlinear Optical Probe. *Nature* **2007**, *447* (7148), 1098–1101.

(7) Long, J. P.; Simpkins, B. S.; Rowenhorst, D. J.; Pehrsson, P. E. Far-Field Imaging of Optical Second-Harmonic Generation in Single GaN Nanowires. *Nano Lett.* **2007**, *7* (3), 831–836.

(8) He, H.; Zhang, X.; Yan, X.; Huang, L.; Gu, C.; Hu, M.; Zhang, X.; Ren, X. min; Wang, C. Broadband Second Harmonic Generation in GaAs Nanowires by Femtosecond Laser Sources. *Appl. Phys. Lett.* **2013**, *103* (14), 143110.

(9) Liu, W.; Wang, K.; Liu, Z.; Shen, G.; Lu, P. Laterally Emitted Surface Second Harmonic Generation in a Single ZnTe Nanowire. *Nano Lett.* **2013**, *13* (9), 4224–4229.

(10) Liu, W.; Wang, K.; Long, H.; Chu, S.; Wang, B.; Lu, P. Near-Resonant Second-Order Nonlinear Susceptibility in c-Axis Oriented ZnO Nanorods. *Appl. Phys. Lett.* **2014**, *105* (7), 71906.

(11) Mariani, S.; Andronico, A.; Lemaître, A.; Favero, I.; Ducci, S.; Leo, G. Second-Harmonic Generation in AlGaAs Microdisks in the Telecom Range. *Opt. Lett.* **2014**, *39* (10), 3062.

(12) Zeng, Y.; Roland, I.; Checoury, X.; Han, Z.; Kurdi, M. E.; Sauvage, S.; Gayral, B.; Brimont, C.; Guillet, T.; Mexis, M.; Semond, F.; Boucaud, P. Resonant Second Harmonic Generation in a Gallium Nitride Two-Dimensional Photonic Crystal on Silicon. *Appl. Phys. Lett.* **2015**, *106* (8), 81105.

(13) Miragliotta, J.; Wickenden, D. K.; Kistenmacher, T. J.; Bryden, W. A. Linear- and Nonlinear-Optical Properties of GaN Thin Films. *J. Opt. Soc. Am. B* **1993**, *10* (8), 1447–1456.

(14) Angerer, W. E.; Yang, N.; Yodh, A. G.; Khan, M. A.; Sun, C. J. Ultrafast Second-Harmonic Generation Spectroscopy of GaN Thin Films on Sapphire. *Phys. Rev. B* **1999**, *59* (4), 2932–2946.

(15) Kim, D.; Libon, I. H.; Voelkmann, C.; Shen, Y. R.; Petrova-Koch, V. Multiphoton Photoluminescence from GaN with Tunable Picosecond Pulses. *Phys. Rev. B* **1997**, *55* (8), R4907–R4909.

(16) Johnson, J. C.; Yan, H.; Schaller, R. D.; Petersen, P. B.; Yang, P.; Saykally, R. J. Near-Field Imaging of Nonlinear Optical Mixing in Single Zinc Oxide Nanowires. *Nano Lett.* **2002**, *2* (4), 279–283.

(17) Abe, M.; Awata, N.; Matsushita, T.; Hakamata, M.; Ozawa, K.; Murakami, R.; Shoji, I.; Kondo, T. Accurate Measurement of Quadratic Nonlinear-Optical Coefficients of Zinc Oxide. *J. Opt. Soc. Am. B* **2012**, *29* (9), 2392.

(18) Ebothé, J.; Kityk, I. V.; Fuks-Janczarek, I. Two-Photon Absorption Study of the Large-Sized Nanocrystallites. *Appl. Surf. Sci.* **2006**, *252* (16), 5763–5767.

(19) Mascheck, M.; Schmidt, S.; Silies, M.; Yatsui, T.; Kitamura, K.; Ohtsu, M.; Leipold, D.; Runge, E.; Lienau, C. Observing the Localization of Light in Space and Time by Ultrafast Second-Harmonic Microscopy. *Nat. Photonics* **2012**, *6* (5), 293–298.

(20) Urban, B. E.; Neogi, P. B.; Butler, S. J.; Fujita, Y.; Neogi, A. Second Harmonic Imaging of Plants Tissues and Cell Implosion Using Two-Photon Process in ZnO Nanoparticles. *J. Biophotonics* **2012**, *5* (3), 283–291.

(21) Dai, J.; Zeng, J.-H.; Lan, S.; Wan, X.; Tie, S.-L. Competition between Second Harmonic Generation and Two-Photon-Induced Luminescence in Single, Double and Multiple ZnO Nanorods. *Opt. Express* **2013**, *21* (8), 10025.

(22) Ambacher, O. Growth and Applications of Group III-Nitrides. *J. Phys. Appl. Phys.* **1998**, *31* (20), 2653–2710.

(23) Ponce, F. A.; Bour, D. P. Nitride-Based Semiconductors for Blue and Green Light-Emitting Devices. *Nature* **1997**, *386* (6623), 351–359.

(24) Carts-Powell, Yvonne. NOVEL STRUCTURES: GaN pyramids prove promising for microcavities http://www.laserfocusworld.com/articles/print/volume-35/issue-11/world-news/novel-structures-gan-pyramids-prove-promising-for-microcavities.html (accessed Sep 26, 2016).

(25) Zeng, K. C.; Lin, J. Y.; Jiang, H. X.; Yang, W. Optical Properties of GaN Pyramids. *Appl. Phys. Lett.* **1999**, *74* (9), 1227–1229.

(26) Jiang, H. X.; Lin, J. Y.; Zeng, K. C.; Yang, W. Optical Resonance Modes in GaN Pyramid Microcavities. *Appl. Phys. Lett.* **1999**, *75* (6), 763–765.

(27) Bidnyk, S.; Little, B. D.; Cho, Y. H.; Krasinski, J.; Song, J. J.; Yang, W.; McPherson, S. A. Laser Action in GaN Pyramids Grown on (111) Silicon by Selective Lateral Overgrowth. *Appl. Phys. Lett.* **1998**, *73* (16), 2242–2244.

(28) Chen, W.; Hu, G.; Jiang, J.; Liu, M.; Yang, Y.; Xiang, P.; Hu, G.; Lin, Y.; Wu, Z.; Liu, Y.; Zhang, B. Electrically Driven Single Pyramid InGaN/GaN Micro Light-Emitting Diode Grown on Silicon Substrate. *J. Disp. Technol.* **2015**, *11* (3), 285–291.

(29) Handbook of Nanoscale Optics and Electronics, 1st Edition | Gary Wiederrecht | ISBN 9780123751782 http://store.elsevier.com/Handbook-of-Nanoscale-Optics-and-Electronics/isbn-9780123751782/ (accessed Aug 24, 2016).

(30) Sun, C.-K.; Liang, J.-C.; Wang, J.-C.; Kao, F.-J.; Keller, S.; Mack, M. P.; Mishra, U.; DenBaars, S. P. Two-Photon Absorption Study of GaN. *Appl. Phys. Lett.* **2000**, *76* (4), 439–441.

(31) Chao, L. C.; Steckl, A. J. CW Blue-Green Light Emission from GaN and SiC by Sum-Frequency Generation and Second Harmonic Generation. *J. Electron. Mater. 29* (9), 1059–1062.

(32) Toda, Y.; Matsubara, T.; Morita, R.; Yamashita, M.; Hoshino, K.; Someya, T.; Arakawa, Y. Two-Photon Absorption and Multiphoton-Induced Photoluminescence of Bulk GaN Excited below the Middle of the Band Gap. *Appl. Phys. Lett.* **2003**, *82* (26), 4714–4716.

(33) Abe, M.; Sato, H.; Shoji, I.; Suda, J.; Yoshimura, M.; Kitaoka, Y.; Mori, Y.; Kondo, T. Accurate Measurement of Quadratic Nonlinear-Optical Coefficients of Gallium Nitride. *J. Opt. Soc. Am. B* **2010**, *27* (10), 2026–2034.

(34) Coquillat, D.; Vecchi, G.; Comaschi, C.; Malvezzi, A. M.; Torres, J.; d'Yerville, M. L. V. Enhanced Second- and Third-Harmonic Generation and Induced Photoluminescence in a Two-Dimensional GaN Photonic Crystal. *Appl. Phys. Lett.* **2005**, *87* (10), 101106.

(35) Soya, T.; Inose, Y.; Kunugita, H.; Ema, K.; Yamano, K.; Kikuchi, A.; Kishino, K. Second Harmonic Generation from Photonic Structured GaN Nanowalls. *J. Phys. Conf. Ser.* **2009**, *193* (1), 12056.

(36) Kitamura, S.; Hiramatsu, K.; Sawaki, N. Fabrication of GaN Hexagonal Pyramids on Dot-Patterned GaN/Sapphire Substrates via Selective Metalorganic Vapor Phase Epitaxy. *Jpn. J. Appl. Phys.* **1995**, *34* (Part 2, No. 9B), L1184–L1186.

(37) Lundskog, A.; Forsberg, U.; Holtz, P. O.; Janzén, E. Morphology Control of Hot-Wall MOCVD Selective Area Grown Hexagonal GaN Pyramids. *Cryst. Growth Des.* **2012**, *12* (11), 5491–5496.

(38) Lundskog, A.; Hsu, C. W.; Nilsson, D.; Karlsson, K. F.; Forsberg, U.; Holtz, P. O.; Janzén, E. Controlled Growth of Hexagonal GaN Pyramids by Hot-Wall MOCVD. *J. Cryst. Growth* **2013**, *363*, 287–293.

(39) Zheleva, T. S.; Nam, O.-H.; Bremser, M. D.; Davis, R. F. Dislocation Density Reduction via Lateral Epitaxy in Selectively Grown GaN Structures. *Appl. Phys. Lett.* **1997**, *71* (17), 2472–2474.

(40) Farrer, J. K.; Carter, C. B. Defect Structure in GaN Pyramids. *J. Mater. Sci.* **2006**, *41* (3), 779–792.

(41) Nam, O.-H.; Zheleva, T. S.; Bremser, M. D.; Davis, R. F. Lateral Epitaxial Overgrowth of GaN Films on SiO2 Areas via Metalorganic Vapor Phase Epitaxy. *J. Electron. Mater. 27* (4), 233–237.

(42) Moran, B.; Wu, F.; Romanov, A. E.; Mishra, U. K.; Denbaars, S. P.; Speck, J. S. Structural and Morphological Evolution of GaN Grown by Metalorganic Chemical Vapor Deposition on SiC Substrates Using an AlN Initial Layer. *J. Cryst. Growth* **2004**, *273* (1–2), 38–47.

(43) Miyake, H.; Takeuchi, R.; Hiramatsu, K.; Naoi, H.; Iyechika, Y.; Maeda, T.; Riemann, T.; Bertram, F.; Christen, J. High Quality GaN Grown by Facet-Controlled ELO (FACELO) Technique. *Phys. Status Solidi A* **2002**, *194* (2), 545–549.

(44) Guo, B.; Qiu, Z. R.; Lin, J. Y.; Jiang, H. X.; Wong, K. S. Deep Bandtail States Picosecond Intensity-Dependent Carrier Dynamics of GaN Epilayer under High Excitation. *Appl. Phys. B* **2005**, *80* (4–5), 521–526.

(45) Binet, F.; Duboz, J. Y.; Off, J.; Scholz, F. High-Excitation Photoluminescence in GaN: Hot-Carrier Effects and the Mott Transition. *Phys. Rev. B* **1999**, *60* (7), 4715–4722.

(46) Cingolani, R.; Ferrara, M.; Lugarà, M. Electron-Hole Plasma Generation in Gallium Nitride. *Solid State Commun.* **1986**, *60* (9), 705–708.

(47) Li, X.; Bohn, P. W.; Kim, J.; White, J. O.; Coleman, J. J. Spatially Resolved Band-Edge Emission from Partially Coalesced GaN Pyramids Prepared by Epitaxial Lateral Overgrowth. *Appl. Phys. Lett.* **2000**, *76* (21), 3031–3033.

(48) Tekkozyan, V. A.; Li, K.; Babajanyan, A. Z.; Nerkararyan, K. V. Formation of Excitons in Semiconductor Nanostructures in the Presence of Electron-Hole Plasma. *J. Contemp. Phys. Armen. Acad. Sci.* **2014**, *49* (3), 123–126.

(49) Krotkus, S.; Miasojedovas, S.; Juršėnas, S. Threshold of Stimulated Emission in GaN Layers Grown by Various Techniques. *Phys. B Condens. Matter* **2014**, *450*, 16–20.

(50) Cachoncinlle, C.; Millon, E.; Petit, A. High-Resolution Emission Spectroscopy of Random Lasing in GaN Films Pumped by UV-Pulsed Laser. *Opt. Commun.* **2016**, *368*, 49–53.

(51) Reshchikov, M. A.; Morkoç, H. Luminescence Properties of Defects in GaN. *J. Appl. Phys.* **2005**, *97* (6), 61301.

(52) Liu, Q. K. K.; Hoffmann, A.; Siegle, H.; Kaschner, A.; Thomsen, C.; Christen, J.; Bertram, F. Stress Analysis of Selective Epitaxial Growth of GaN. *Appl. Phys. Lett.* **1999**, *74* (21), 3122.

(53) Reichenbach, P.; Eng, L. M.; Georgi, U.; Voit, B. 3D-Steering and Superfocusing of Second-Harmonic Radiation through Plasmonic Nano Antenna Arrays. *J. Laser Appl.* **2012**, *24* (4), 42005.

(54) Prasanth, R.; Vugt, L. K. van; Vanmaekelbergh, D. a. M.; Gerritsen, H. C. Resonance Enhancement of Optical Second Harmonic Generation in a ZnO Nanowire. *Appl. Phys. Lett.* **2006**, *88* (18), 181501.

(55) Kityk, I. V.; Marciniak, B.; Mefleh, A. Photoinduced Second Harmonic Generation in Molecular Crystals Caused by Defects. *J. Phys. Appl. Phys.* **2001**, *34* (1), 1.

(56) Tanabe, T.; Notomi, M.; Kuramochi, E.; Shinya, A.; Taniyama, H. Trapping and Delaying Photons for One Nanosecond in an Ultrasmall High-Q Photonic-Crystal Nanocavity. *Nat. Photonics* **2007**, *1* (1), 49–52.

(57) Almeida, V. R.; Barrios, C. A.; Panepucci, R. R.; Lipson, M. All-Optical Control of Light on a Silicon Chip. *Nature* **2004**, *431* (7012), 1081–1084.

(58) Del'Haye, P.; Schliesser, A.; Arcizet, O.; Wilken, T.; Holzwarth, R.; Kippenberg, T. J. Optical Frequency Comb Generation from a Monolithic Microresonator. *Nature* **2007**, *450* (7173), 1214–1217.

(59) Grudinin, I. S.; Matsko, A. B.; Savchenkov, A. A.; Strekalov, D.; Ilchenko, V. S.; Maleki, L. Ultra High Q Crystalline Microcavities. *Opt. Commun.* **2006**, *265* (1), 33–38.

(60) Kudo, H. Whispering Gallery Modes in Hexagonal Microcavities. *Phys. Rev. A* **2013**, *88* (2).

(61) Grudinin, I. S. Crystalline Whispering Gallery Mode Resonators for Quantum and Nonlinear Optics. Doctoral Dissertation, California Institute of Technology, 2008.

(62) Czekalla, C.; Nobis, T.; Rahm, A.; Cao, B.; Zúñiga-Pérez, J.; Sturm, C.; Schmidt-Grund, R.; Lorenz, M.; Grundmann, M. Whispering Gallery Modes in Zinc Oxide Micro- and Nanowires. *Phys. Status Solidi B* **2010**, *247* (6), 1282–1293.

(63) Lu, J.; Xu, C.; Dai, J.; Li, J.; Wang, Y.; Lin, Y.; Li, P. Plasmon-Enhanced Whispering Gallery Mode Lasing from Hexagonal Al/ZnO Microcavity. *ACS Photonics* **2015**, *2* (1), 73–77.

(64) Dong, H.; Chen, Z.; Sun, L.; Lu, J.; Xie, W.; Tan, H. H.; Jagadish, C.; Shen, X. Whispering Gallery Modes in Indium Oxide Hexagonal Microcavities. *Appl. Phys. Lett.* **2009**, *94* (17), 173115.

(65) Sono, T. J. The Study of Surface SHG and Polygonal Microcavity Design for Nonlinear Applications on LiNbO3. phd, University of Southampton, 2009.

(66) Ilchenko, V. S.; Savchenkov, A. A.; Matsko, A. B.; Maleki, L. Nonlinear Optics and Crystalline Whispering Gallery Mode Cavities. *Phys. Rev. Lett.* **2004**, *92* (4), 43903.

(67) Strekalov, D. V.; Marquardt, C.; Matsko, A. B.; Schwefel, H. G. L.; Leuchs, G. Nonlinear and Quantum Optics with Whispering Gallery Resonators. *ArXiv160507972 Phys. Physicsquant-Ph* **2016**.

(68) Nobis, T.; Kaidashev, E. M.; Rahm, A.; Lorenz, M.; Grundmann, M. Whispering Gallery Modes in Nanosized Dielectric Resonators with Hexagonal Cross Section. *Phys. Rev. Lett.* **2004**, *93* (10), 103903.

(69) Zhang, Y.; Zhou, H.; Liu, S. W.; Tian, Z. R.; Xiao, M. Second-Harmonic Whispering-Gallery Modes in ZnO Nanotetrapod. *Nano Lett.* **2009**, *9* (5), 2109–2112.

(70) Zhang, Y.; Grady, N. K.; Ayala-Orozco, C.; Halas, N. J. Three-Dimensional Nanostructures as Highly Efficient Generators of Second Harmonic Light. *Nano Lett.* **2011**, *11* (12), 5519–5523.

CHAPTER 4

SECOND HARMONIC GENERATION AND MULTI-PHOTON LUMINESCENCE IN NON POLAR INGAN/GAN COAXIAL QUANTUM WELLS ON GAN PYRAMIDS

4.1 Introduction

GaN based optical devices have been of continuous interest over several years because of their transparency over a wide spectrum of frequencies ranging from UV to mid infra-red[1]. Alloys of GaN, especially InGaN are highly important from a technological application point of view because of their use as the active region in blue to green light emitting diodes and lasers[2,3]. Motivated by the reduction in piezoelectric fields[4,5], a great deal of interest has been invested in nonpolar and semipolar InGaN/GaN quantum wells (QWs). InGaN QWs grown on micro- and nano- structures like semipolar pyramids[6,7], stripes[8,9], nonpolar rods[10–13] and tubes[14,15] have been investigated for the linear optical properties.

High thermal conductivity and non-vanishing second order susceptibility makes InGaN a potential candidate for nonlinear optical devices. Nonlinear optical investigations of planar InGaN/GaN quantum wells[16] and quantum dots[17,18] were reported. SHG and two photon luminescence from InGaN/GaN c-planar structures have been published[19]. H. Schmidt et al found a second order susceptibility value of 1.3×10^{-10} m/V for narrow wells in c-planar InGaN/GaN[19]. S. Krishnamurthy et al[20] predicted an increase in the two photon absorption coefficient with an increase in indium content in the order of 25 cm/GW for 25% indium content at 600 nm in c-planar structures. These reports show the nonlinear nature of InGaN/GaN MQWs structures and can have potential applications in nonlinear optics. In the context of finding nonlinear semiconductor micro-nano semiconductor structures with controlled growth, nonlinear optical properties of selectively grown two-dimensional coaxial InGaN/GaN MQW submicron hetero-structures are investigated.

In this chapter, we report the structural and optical studies of epitaxial grown co-axial InGaN/GaN MQW submicron tubes (SMTs). Co-axial InGaN/GaN MQW hetero-structures were fabricated by depositing InGaN/GaN layers on the side walls of GaN submicron tubes on top of GaN micro-pyramids. STEM measurements along with HAADF confirms the presence of InGaN/GaN MQW layers with low In incorporation. Experimental results of linear and nonlinear optical response from single and an ensemble of InGaN/GaN MQW SMTs at room temperature are presented. Nonlinear optical properties of coaxial InGaN/GaN multiple quantum well (MQWs) submicron hetero-structures were investigated using a tunable femtosecond laser at room temperature. Time resolved PL measurements were done to confirm the absence of piezoelectric fields in nonpolar InGaN MQWs. Nonlinear light generation processes such as SHG and MPL were observed. Tunability of SHG was tested for a range of excitation wavelengths.

4.2 Experimental

4.2.1 Sample Preparation

InGaN/GaN co-axial multi quantum well layers were grown on c-axis sapphire using a multi-layer growth process as established in previous studies[21–23,15] and is schematically represented in figure 4.1. Facets of ZnO SMRs were used as templates to grow co-axial GaN and InGaN layers. In the first step, GaN pyramids were grown using epitaxial lateral overgrowth in a low pressure MOCVD system with a lithographically patterned SiO_2 mask of 3 µm opening on a GaN buffered c-plane sapphire substrate. Secondly, ZnO SMRs of 200 - 700 nm diameter and 2-3 µm heights were grown on the top of GaN pyramids using vapor transport method, where the different surface planes of patterned GaN-pyramids provided growth selectivity. By controlling the growth kinematics, plateaus can be formed at the apex of GaN pyramids, which provides selective growth on the top of the pyramid apices compared to facets. After the synthesis of ZnO SMRs, GaN and InGaN layers were epitaxially grown around the ZnO SMRs by using metal organic chemical vapor deposition method in order to fabricate coaxial hetero-structures.

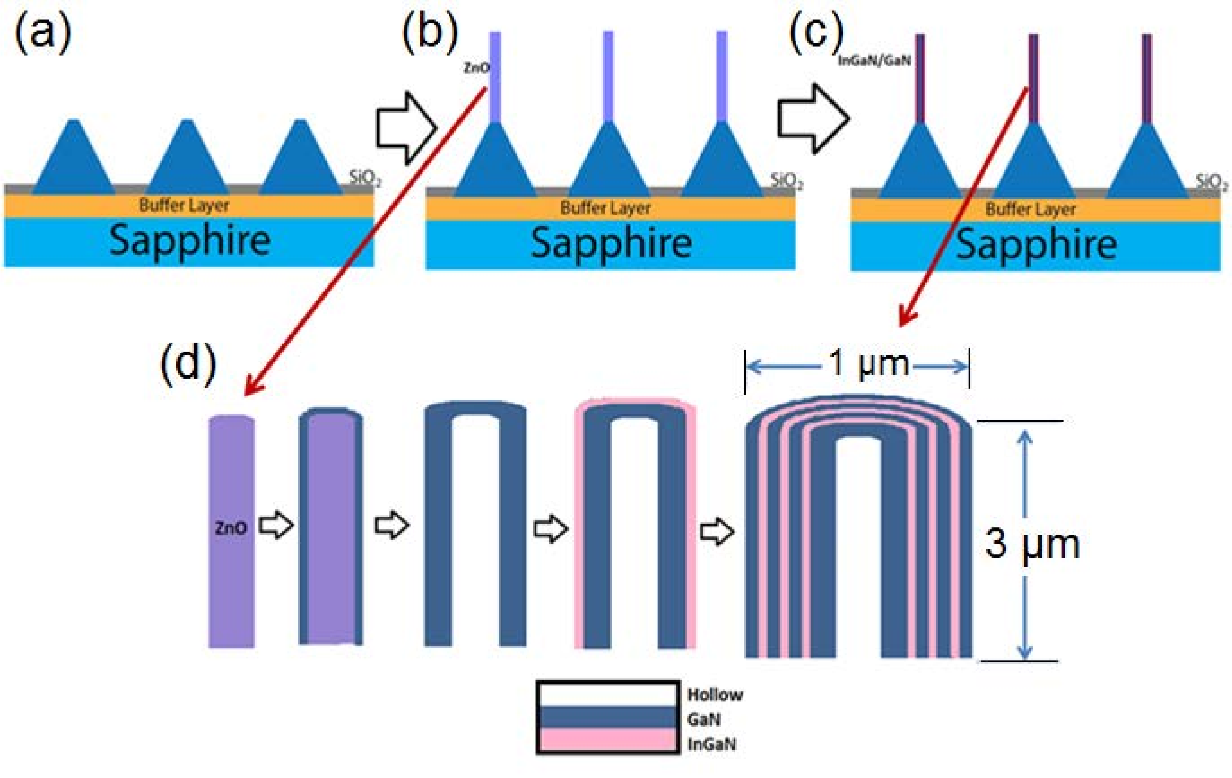

Figure 4.1. Schematic of the growth process of co-axial InGaN/GaN submicron tubes around ZnO submicron rods on micro-pyramid structure. Figures (a-c) represents each step of the multi-layer growth process and (d) shows a closer look at the layer overgrowth process resulting in InGaN/GaN co-axial tube structures. The hexagonal micro-pyramids are approximately 3 µm in base diameter and 3 µm in height. InGaN/GaN tubes are approximately 1 µm in diameter and 3-4 µm in height.

Trimethylgallium (TMGa) and ammonia (NH3) were used for the deposition of GaN layers around ZnO pillars, whereas trimethylindium (TMIn) and triethylgallium (TEGa) were used for the deposition of the quantum wells and the barriers. The first GaN barrier layer around ZnO SMR was grown at two temperature steps, the first one at 550 ^{0}C lower than the ZnO sublimation temperature (≥ 600 ^{0}C [24,25]). The carrier gas used was N_2. This protects the ZnO from being etched at the onset of the growth process so that it can provide a sturdy template for subsequent growth layers. The growth temperature was gradually increased in order to improve the quality of GaN. With the temperature at 1050 ^{0}C and H_2 as carrier gas, hollow GaN tubes were achieved, since the ZnO in the core decomposes during growth at high temperature. After the deposition of the final epi-layer of the first barrier GaN layer, the temperature was reduced for the deposition of three coaxial thin InGaN/GaN layers and barriers, respectively. For these layers, growth conditions optimized for c-plane GaN resulting in well/ barrier thicknesses of 4 and 8 nm, respectively were used.

4.2.2 Sample Characterization

Scanning electron microscopy (SEM) was used to investigate the morphology of samples during each step of the growth process. InGaN/GaN MQW formation and thickness were investigated using TEM, where as In incorporation was measured using STEM in the HAADF mode. The co-axial SMTs were sectioned from the original sample using focused Ga ion beam (FIB) and were transferred to a TEM grid using a lift-out process with a micro-manipulator. The SMTs were then prepared into thin slices using FIB milling technique. TEM sample preparation was carried out such that the axial (longitudinal) cross section of the SMT could be imaged.

The linear and nonlinear optical properties of an ensemble and single InGaN MQW SMTs were studied using far-field and micro-photoluminescence set up. Single photon optical excitation was achieved using the 325 nm line from a continuous wave Helium- Cadmium laser of 25 mW. Two-photon excitation was achieved using a femto second tunable Ti: Sapphire laser (Mai Tai, Spectra Physics) with emission wavelength ranging from 700 nm-1000 nm, pulse width of 80 fs and repetition rate of 80 MHz. The excitation wavelength for multi-photon experiments were chosen to be in the range of 720nm to 900nm to achieve above, below and InGaN QW resonance excitation energies. A variable attenuator was used to control the input power to the sample. An ensemble of structures was excited by a 100 µm diameter excitation spot size with the incident beam at a 45^0 angle from the normal of the sample. Single SMT measurements were made using multi-photon microscopy setup using a spot size of ~ 600 nm with a 0.9 NA objective lens. Single photon excited PL was measured using a 350-650 nm interference band pass filter and a 0.32m spectrometer with a back thinned CCD detector; whereas nonlinear light generation was measured using a fiber coupled thermo-electric cooled CCD detector to the microscope.

4.3 Results and Discussion

4.3.1 Structural Morphology

Figure 4.2 shows the major steps in the co-axial SMT growth process as measured by SEM. An array of selectively grown InGaN/GaN co-axial SMTs oriented in the c-direction with QWs on the m-plane facets is displayed in the SEM image shown in figure 4.2d. Although the ZnO SMR represented by figure 4.2a shows nanometer dimension in the radial direction, a significant deviation was observed in ZnO SMR diameters ranging from 300 nm to 700 nm. This deviation

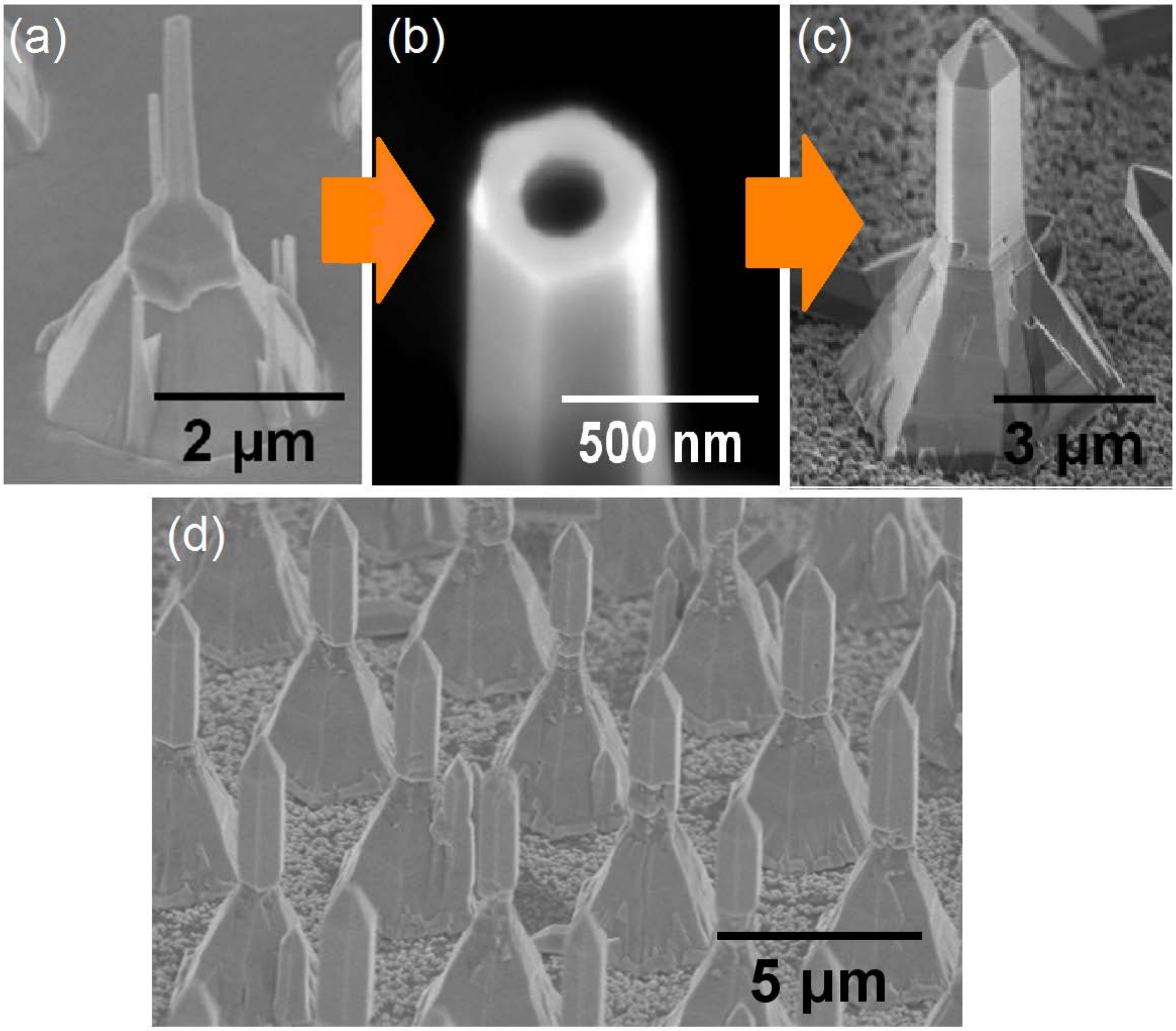

Figure 4.2. SEM Images of structures formed during multi-layer growth process. (a) Image showing ZnO rod on GaN pyramid, Images of a single (b) Hollow GaN tube on GaN pyramid, (c) InGaN/GaN SMTs on GaN pyramid after the growth of 3 InGaN and GaN layers. Image (d) shows an array of InGaN/GaN MQWs on GaN micro-pyramid.

was a resultant of the variation in the diameters of c-plane plateau on the pyramid apex. Figure 4.2b shows the image of a GaN tube grown on GaN pyramid prior to the InGaN QW growth. The estimated diameter of the bare hollow GaN tube is ~ 400 nm with a wall thickness of ~ 110 nm. Figure 4.2c shows a single co-axial SMT structure on the GaN pyramid after the layered growth process of InGaN quantum well and GaN barrier layers. The InGaN/GaN multiple quantum well structures as shown in figures 4.2 c and d shows an increase in diameter to about 1 to 1.5 µm due to growth of InGaN and GaN layers. The resultant SMTs were 3 – 4 µm in height. It can be noticed that submicron sized tubes are also occasionally grown on the a-plane facets of the GaN pyramids. The top part of the tube is converged to form a pyramid like cap as a result of the GaN barrier layer grown at reduced temperature during the epitaxial layer overgrowth process[15]. As seen in figure 4.2 c-d, the MQWs on the m-plane facets are generally smooth except at the interface of pyramid apex and the tube, where some roughness is observed.

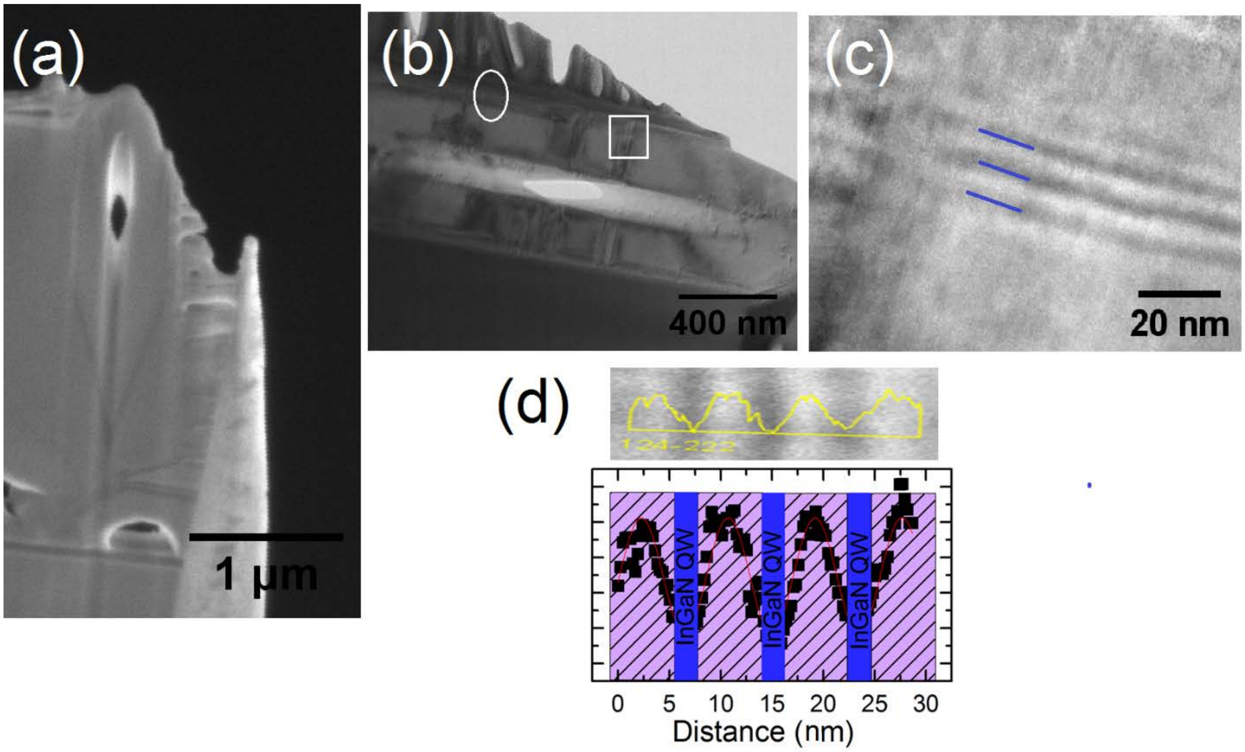

Figure 4.3. Electron microscopy measurements of InGaN/GaN MQWs. (a) SEM image of FIB milled sample prepared for TEM, (b) Brightfield TEM image of InGaN/GaN co-axial SMT cross section, (c) Bright field image showing 3 InGaN QWs (blue lines) and (d) Histogram representing approximate QW and barrier widths of 3 nm and 8 nm respectively.

Figure 4.3 describes the MQW structure. Figure 4.3a represents the FIB milled cross section of the InGaN/GaN MQW SMT. It clearly shows the hollow inner part of the GaN tube confirming the sublimation of ZnO pillar template. The image also shows platinum deposition around the

SMT; a step performed before milling the specimen out of the original sample. Figure 4.3 b and c represents the bright field TEM images of InGaN/GaN MQWs using a 200 keV beam. Figure 4.3b shows the presence of MQWs around the outside of the GaN SMT cross-section. There are defects present along the transverse axis of the SMT, which seemed to have originated at the first GaN barrier layer and propagated in the growth direction. These radially propagating defects may have stemmed from the slight lattice mismatch of ZnO SMR template. Figure 4.3c is a zoomed in area of the inside of the white square marked in figure 4.3b. Three QWs can be clearly noticed in this image. The cylindrical shape of the SMT makes the TEM imaging challenging as it caused the transmitted electrons to deflect from its normal course creating aberrations which results in poor resolution. Contrast intensity profile as plotted in figure 4.3d was used to estimate the QW and barrier thickness and was determined to be approximately 3 nm and 8 nm respectively.

MQW structure was examined by scanning transmission electron microscopy (STEM) in different modes. STEM measurements under multiple imaging modes were performed to investigate the atomic incorporation of In and Zn. Figure 4.4 shows the STEM images in different imaging modes. Bright and dark field STEM images as shown in figure 4.4a and b indicates QWs. Poor contrast is mainly caused by the thickness of the TEM specimen. Figures 4.4c and d represents the images captured using high angle annular dark field detector in the STEM-scope. Atomic number contrast as seen in figure 4.4c slightly illustrates QWs; however, the atomic contrast is very less compared

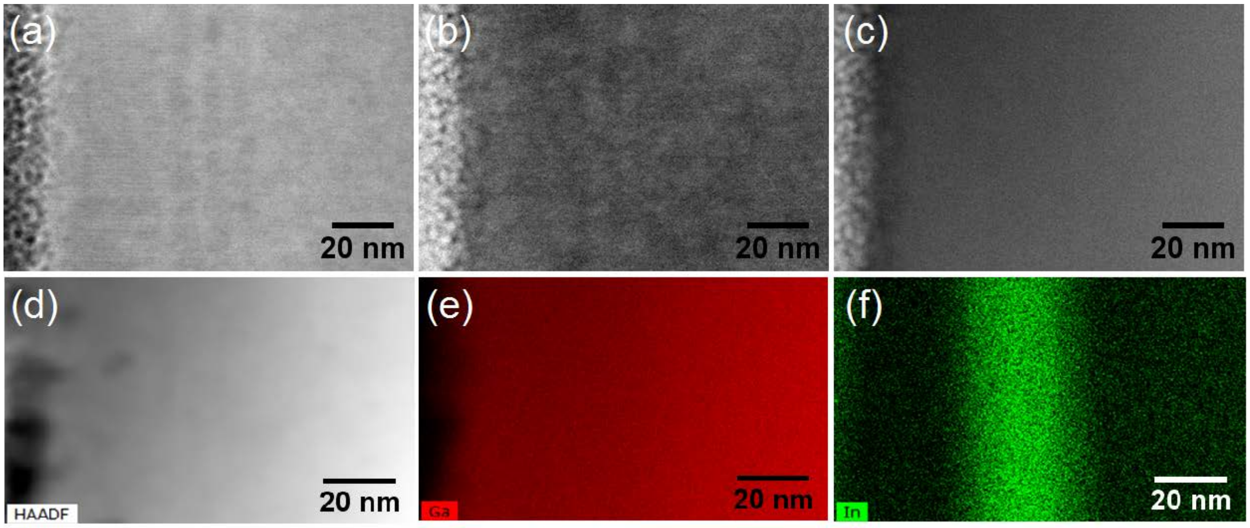

Figure 4.4. STEM micrographs of InGaN/GaN MQWs under different imaging modes. (a) Bright field STEM image of 3 layer InGaN MQW. (b) Dark field mode (c) HAADF in Z-contrast mode, (d) HAADF mode (e) EDX map of Ga atoms and (f) EDX map of In atoms.

to the diffraction contrast in figures 4.4 a-b. The atomic fractions of Ga and In atoms were measured by energy dispersive x-ray spectroscopy. Figures 4.4 e and f describes the EDX maps of these Ga and In atoms respectively. As seen in image (f), the In concentration is spread over the three QWs. Spreading of In concentration across MQWs is caused by the curved symmetry of the specimen. Presence of Zn atoms were not observed in the area where STEM measurements were performed. Overall atomic concentration of In was quantified to be 1.2 at% from STEM-EDX measurements.

4.3.2 Light Emission from Nonpolar InGaN MQWs

4.3.2.1 Linear Optical Interactions in MQWs

Single photon excitation of InGaN/GaN SMT structures were achieved using 325 nm continuous laser excitation, which corresponds to an excitation energy above the bandgap of both QW and barrier layers. Photoluminescence measurements were performed after each step of growth steps (a) through (c) in figure 4.2. The results of these measurements on ZnO SMRs, GaN SMTs and InGaN/GaN MQW SMTs are shown in figure 4.5. All the photoluminescence measurements are mostly performed at 300 K unless otherwise stated.

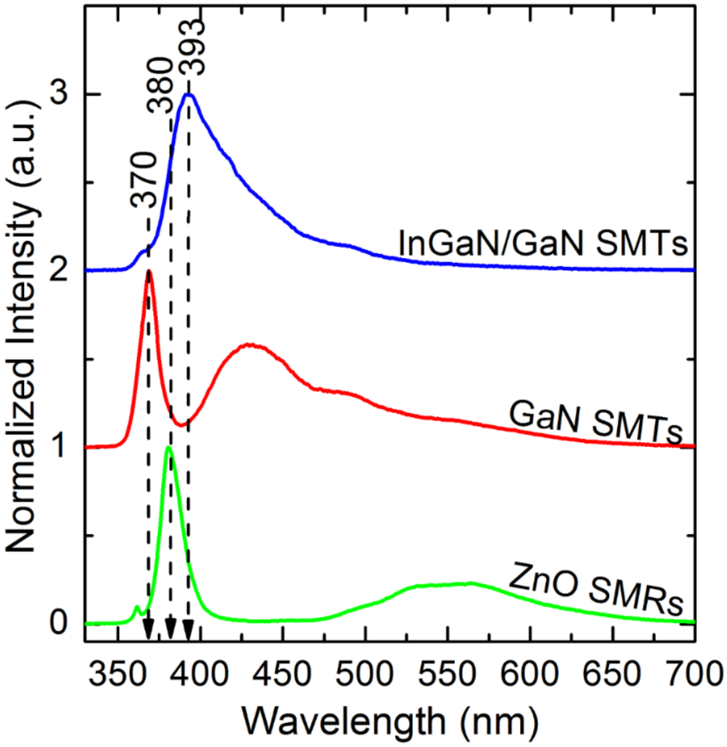

Figure 4.5. Photoluminescence spectra of samples during major steps of InGaN/GaN co-axial MQW SMT growth. Green curve depicts the light generation from ZnO submicron rods, red curve depicts the luminescence from GaN submicron tubes and blue curve represents light generation after deposition of InGaN/GaN MQW layers to form co-axial submicron tubes.

It can be clearly seen that the peak positions in each step differs and is a signature of the difference in the material composition. The first two steps in the growth process, corresponding to green and red curves resembles well accepted peak positions of bandedge emission in ZnO and GaN at room temperature respectively. Photoluminescence from bare GaN SMTs shows absence of ZnO confirming the complete sublimation of ZnO. Several defected related peaks are present in GaN SMTs. Photoluminescence measured post InGaN/GaN MQW growth is represented by the blue line. The UV peak at 393 nm is attributed to the QW emission. The broad nature of this peak can be due to phonon assisted transitions or inhomogeneity in the QW thickness in the ensemble of SMTs.

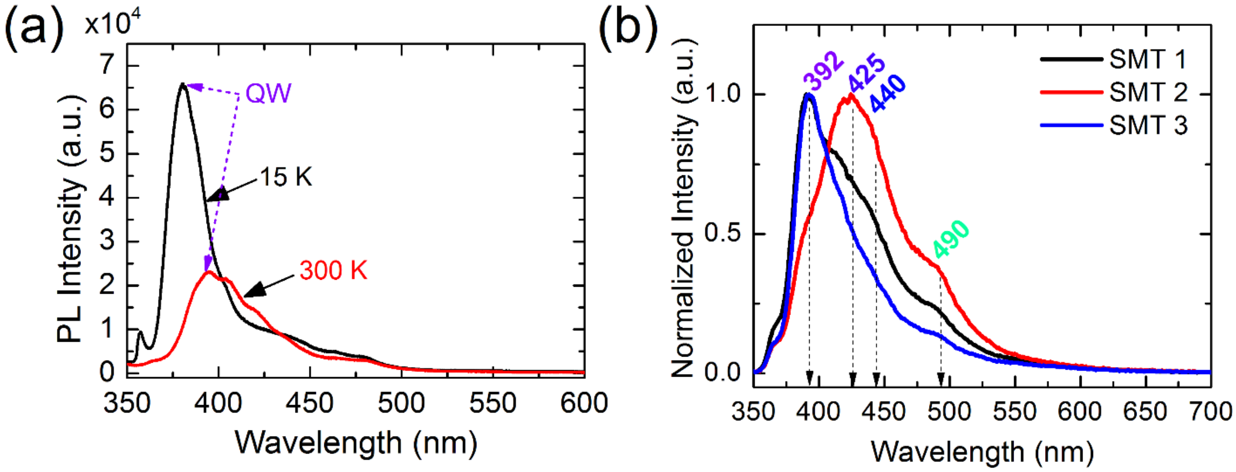

Figure 4.6. Photoluminescence from InGaN/GaN MQW SMTs under single photon excitation above GaN bandgap. (a) Far-field PL from InGaN MQW SMTs. Black line represents PL at 15 K, whereas red line represents PL at 300 K. (b) Micro-PL from three different InGaN MQW SMTs at 300 K.

Figure 4.6a shows the single photon luminescence from an ensemble of InGaN/GaN MQW SMT structures taken at low temperature (15 K) and 300 K. The low intensity peak at around 357 nm originates from the bound exciton transition in GaN. The high intensity peak at 380 nm at 15 K is attributed to the InGaN/GaN quantum well emission. The shorter emission peak wavelength from the InGaN/GaN MQW SMT sample agrees well with recently published works[10–12,26]. Indium incorporation on non-polar planes should result in shorter emission wavelength despite the In composition as opposed to its c-plane counterpart[27]. Shorter emission wavelength can also be expected because of the absence of piezo fields[4]. The broadening of the quantum well emission can be attributed to phonon assisted non-radiative relaxation as well as fluctuations in the QW thickness along the tube facets. At room temperature the QW peak is shifted to ~392 nm due to thermalized carrier distribution and broadening of density of states. Using equation 2.3 and substituting 0.7 eV, 3.42 eV for bandgap energies of InN and GaN, and 1.42 for bowing parameter, an In composition of 3% was calculated. Figure 4.6b also shows that certain SMTs have higher blue emission than the UV emission. In addition to the 392 nm peak, peaks at 425 nm, 440 nm and 490 nm were also observed. Optical microscopy imaging showed blue emission to be mostly generated in the top part of the SMT. This can be attributed to increased indium incorporation in the QWs grown at the semi-polar walls of nano-pyramid tip of the SMTs. Longer emission wavelength has been observed between the edges of nonpolar facets of the co-axial SMTs and the semipolar facets of the hexagonal pyramid tips[11,12]. A red shift in emission wavelength from the bottom sidewall to the apex has be reported previously[11]. Also, unintentional Zn incorporation into the first GaN barrier layer during sublimation process can create Zn acceptors in GaN resulting in blue emission as evidenced by the PL spectra of GaN SMT in figure 4.5.

Time resolved single photon PL was studied to understand the recombination dynamics in the InGaN MQW SMTs. The TRPL results are shown in figure 4.7. Because of the absence of piezo electric fields in the nonpolar QWs, the decay time of PL is expected to be faster owing to the increased overlap of electron-hole wavefunctions[4]. Hence a comparison of TRPL measurements between nonpolar InGaN MQWs and polar InGaN MQWs was done to estimate the PL decay time differences. TRPL measurements were carried out at a temperature of 4 K. An excitation wavelength of 266 nm with 80 MHz repetition rate was used. This restricted the maximum decay time that can be measured to 12 ns. The time integrated spectrum over a 10 ns window is presented in figure 4.7 b and e. These correspond to nonpolar and polar InGaN MQWs respectively. As the accumulation time of photons (integration time) used to collect data varied between the two samples, a direct intensity comparison between the streak images is not possible. However, this does not affect the decay time estimation. The polar MQW sample contains 13 wells with a well width of 3 nm and barrier width of 7.5 nm.

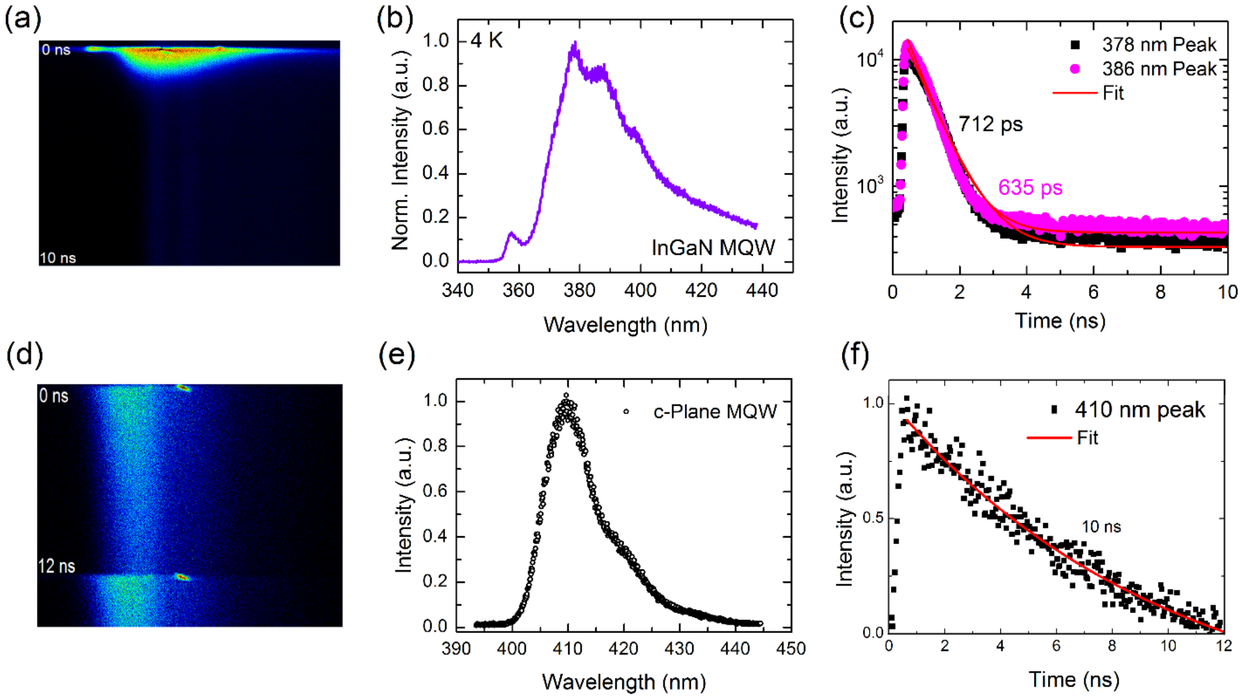

Figure 4.7. Time resolved photoluminescence from InGaN MQW grown in nonpolar and polar directions. Top row represents data from nonpolar MQW and bottom row represents data from polar MQW. (a) and (d) shows the time resolved streak image, (b) and (e) shows the spectrum, (c) and (f) shows the decay of PL. TRPL measurements were at 4 K temperature.

A time window size of 4 nm x 10 ns centered at the peak maximum was used to extract PL decay time information and is shown in figures 4.7 c and f. The nonpolar MQWs has a shorter emission wavelength of 380 nm compared to the 410 nm emission from polar MQWs. The corresponding recombination time of carriers are 712 ps and 10 ns respectively. Clearly, the recombination time from the nonpolar MQWs are few orders faster than the recombination time in polar ones. This confirms that the MQWs grown on nonpolar planes reduces the built in electric fields resulting in faster recombination times. PL decay times ranging from 100 ps to 950 ps for nonpolar InGaN MQWs has been reported previously[28–30]. The large variation in reported decay times stem from the differences in QW widths, number of QWs and also optical pump density used.

4.3.2.2 Nonlinear Optical Interactions in MQWs

The nonlinear response spectra of a single InGaN/GaN MQW SMT at different excitation wavelengths are presented in figure 4.8. The up-converted spectra from InGaN/GaN MQWs show co-existence of two signature peaks. An average power of 10 mW at the sample was maintained for all excitation wavelengths using an attenuator. The narrow peaks pointed out by black arrows in figure 4.8a can be attributed to second harmonic generation from an InGaN/GaN MQW SMT as the position of these narrow peaks depends on the frequency of the excitation, and is exactly half the frequency of the incident beam. In other words, half the wavelength compared to the excitation wavelength. The full width half maximum (FWHM) of the SHG peaks was estimated to be half of $\frac{1}{\sqrt{2}}$ of the band width of the excitation pulse, which is a good indication that these narrow peaks are indeed SHG peaks.

The broad band emission peak at 392 nm does not shift in position when the excitation wavelength is changed from 720 nm to 750 nm. This is believed to be caused by the radiative recombination of carriers from the InGaN quantum well resulting in two photon induced luminescence. The broadening of this peak can be attributed to phonon assisted non-radiative relaxation as well as fluctuations in the QW thickness along the tube facets. The intensity of this

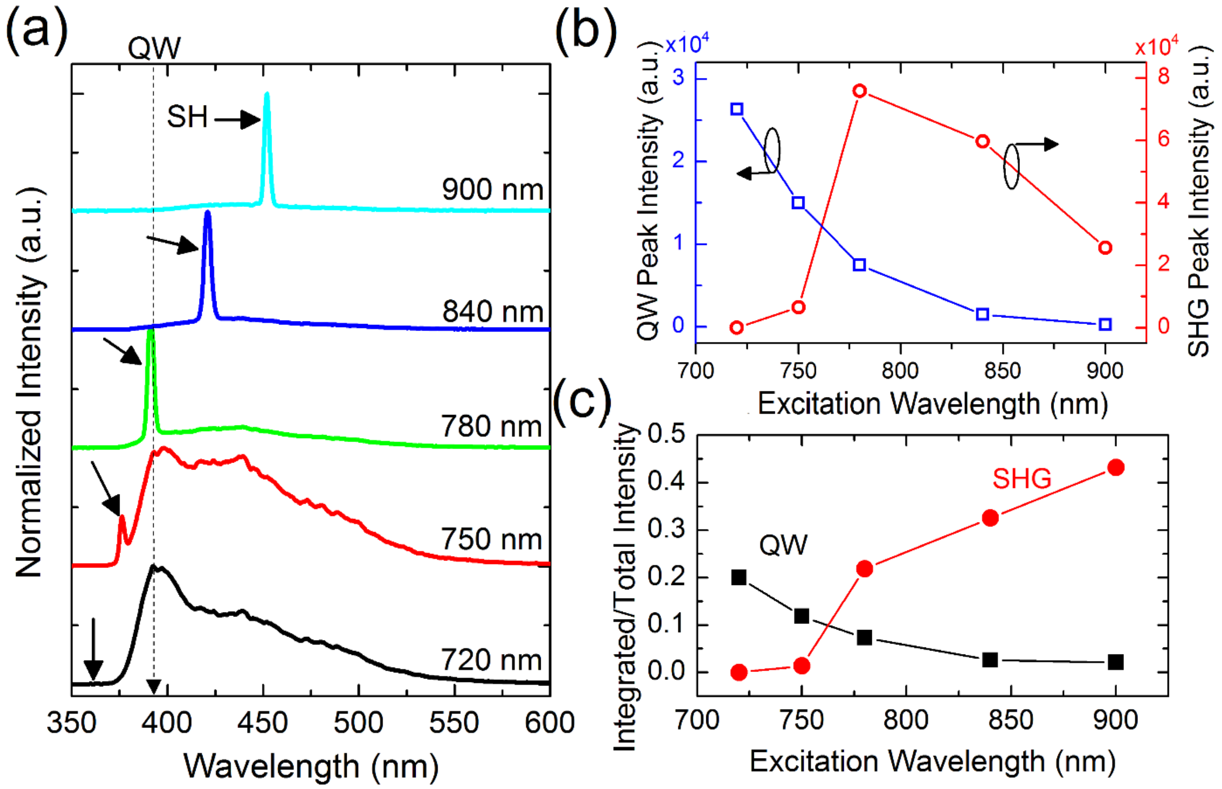

Figure 4.8. Nonlinear light generation from InGaN/GaN MQW SMTs at 300 K. (a) MPL and SHG for multiple excitation wavelengths, (b) SH and QW peak intensity comparison as a function of excitation wavelength and (c) Relative efficiency depicting competition between the two nonlinear processes.

peak becomes weaker as the excitation wavelength is increased (see figure 4.8a; blue curve). This is because as the excitation wavelength is increased the nonlinear absorption resulting in luminescence is caused by higher order odd nonlinearities, which suggests a need for increase in pump density. For 720 nm excitation, there is no SH peak at the arrow (see black curve in figure 4.8a). Any SH generated will be at 360 nm which will be trapped inside the SMT due to linear UV absorption at this frequency. However, as the generated SH peaks are farther away from the linear UV absorption lines, they are radiated out from the InGaN SMTs. The maximum intensity of SHG is observed close to 780 nm excitation wavelength as seen in figure 4.8b (red curve). Excitation wavelength at around 780 nm is closer to the resonance bandgap of the InGaN MQW.

Resonance enhanced SHG has been reported previously[31,32]. The vertical axis of figure 4.8c represents the ratio of integrated emission intensity to the total integrated intensity. This allows the separation of MPL and SHG contribution towards the total radiated intensity. As the excitation wavelength increases, second order nonlinearity becomes the dominant emission because it is directly proportional to the square of the intensity of the pump photons. Therefore, the probability of two photon annihilation to generate coherent SHG is higher which results in the sole contribution of SHG to the total radiation increasing the relative efficiency to unity. Although maximum absolute intensity of SHG is observed at 780 nm for the same pump power, MPL simultaneously exists at this excitation wavelength and therefore 5.8c plot shows reduced relative contribution of SHG at 780 nm excitation. Another factor to be considered in this calculation is the frequency dependent bandwidth of SHG. The higher the frequency, the lower the SHG bandwidth is.

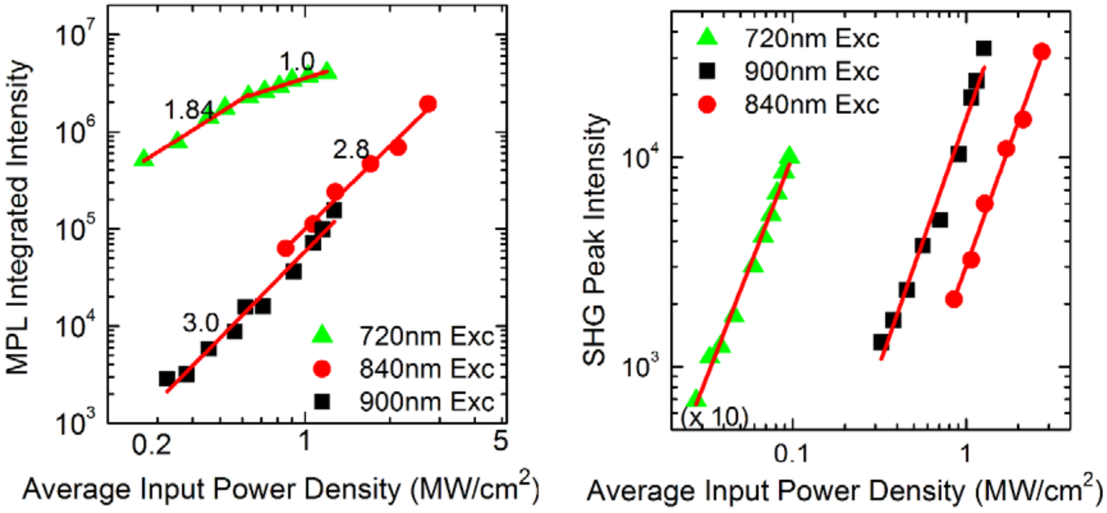

Figure 4.9. Pump power density dependence on nonlinear light generation in InGaN MQW SMTs. (a) Multi-photon luminescence intensity dependence and (b) Second harmonic intensity dependence on 720 nm, 840 nm and 900 nm excitation wavelengths.

Excitation intensity dependence on the intensity of radiation due to second and third order nonlinear processes was measured to understand the m-photon contribution to these radiation peaks. From figure 4.9a, it can be seen that the MPL generated with 720 nm excitation is caused by the simultaneous absorption of two photons as the estimated slope is 1.84. A saturation in the two photon absorption was observed at higher pump powers. The estimated slopes of 2.8 and 3 confirms that a simultaneous absorption of three photons contributed to the MPL at 840 nm and 900 nm excitations, respectively. The estimated values of slopes of SHG intensity as a function of pump intensity followed the quadratic intensity dependence as shown in figure 4.9b. In figure 4.9b, SHG at 720 nm was measured from an ensemble of SMTs; whereas, all other dependence was measured from individual SMTs. Due to linear UV absorption, SHG created by 720 nm is hard to detect from a single SMT. As can be seen in figure 4.9b, the intensity of SHG at 360 nm is exaggerated by an order of magnitude compared to other wavelengths.

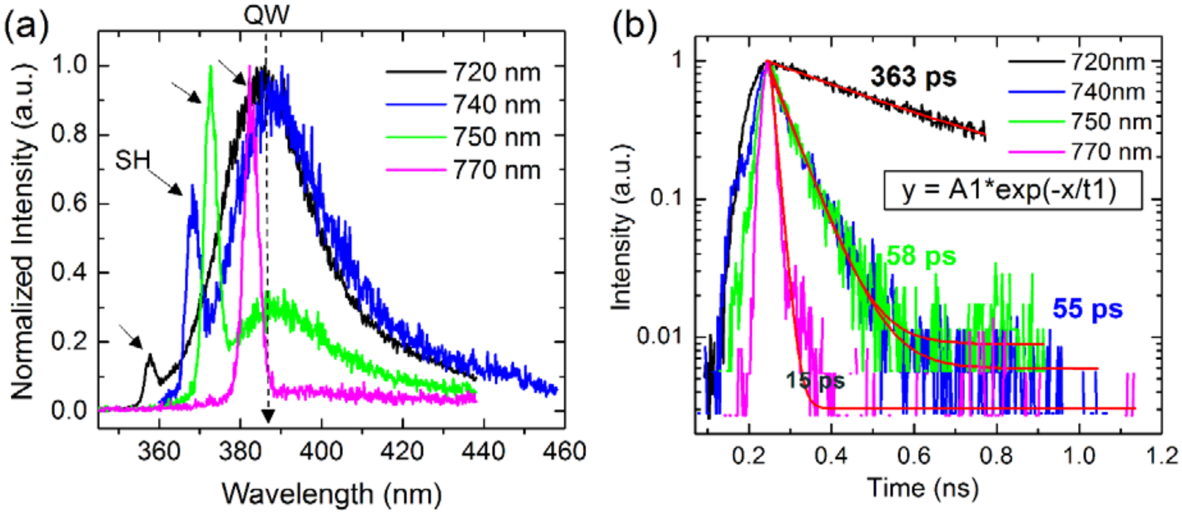

Figure 4.10. Time resolved measurements of InGaN MQW SMTs with below band gap excitation showing carrier dynamics of up converted luminescence. (a) MPL spectra for multiple excitation wavelengths and (b) MPL decay time. Time resolved MPL measurements were at 300 K temperature.

Time resolved multi-photon luminescence for multiple excitation wavelengths is depicted in figure 4.10. These measurements are taken using a far-field backscattered geometry and hence the collected signal is from an ensemble of InGaN MQW SMTs. The use of NIR excitation wavelengths provide larger penetration depths and hence contribution from non-radiative processes at the surface can be reduced. An ensemble of SMT MQWs showed SH signal even for 720 nm excitation wavelength. SHG starts to dominate at 750 nm excitation wavelength and the contribution from spontaneous luminescence decreases significantly. The higher intensity of SHG here compared to single InGaN SMT is due to the higher collection efficiency of the setup from several SMTs. A single exponential fitted MPL decay time of 363 ps suggests that radiative recombination is the dominant mechanism even at room temperature. The faster decay times for higher excitation wavelengths as shown in figure 4.10b suggests competition between the SHG and MPL. At 770 nm, the decay time of 15 ps is represents the transition time of SH signal which follows the timescale of the input laser.

4.4 Conclusions

Non-polar InGaN/GaN MQW sub-micron tubes were fabricated using SA-ELO by MOCVD. High resolution electron microscopy measurements demonstrates the growth of InGaN/GaN MQWs on the nonpolar and semi-polar facets of GaN SMTs despite the presence of radial defects. This allows the reduction or elimination of piezoelectric fields in these emitter structures. Linear and nonlinear optical properties of coaxial InGaN/GaN multiple quantum well submicron hetero-structures were investigated. Single photon luminescence was performed in the sample during each step of the multi-layer process, which distinctively identifies the luminescence of InGaN/GaN MQWs. It also confirmed the presence of InGaN/GaN quantum well emission in the

UV region. Both STEM and optical measurements shows a low indium incorporation in the QWs. Time resolved PL measurements show piezoelectric field free nonpolar QWs. A two photon excited photoluminescence was observed at room temperature from an individual InGaN/GaN QW structure at around 390 nm, independent of excitation wavelength and is attributed to QW emission. In addition, second harmonic signal of the excitation laser was also observed at half the wavelength of the fundamental wavelength. Wavelength dependent measurements shows the tunability range of SHG, which was limited by the excitation laser.

4.5 References

(1) Abe, M.; Sato, H.; Shoji, I.; Suda, J.; Yoshimura, M.; Kitaoka, Y.; Mori, Y.; Kondo, T. Accurate Measurement of Quadratic Nonlinear-Optical Coefficients of Gallium Nitride. *J. Opt. Soc. Am. B* **2010**, *27* (10), 2026–2034.

(2) Nakamura, S.; Senoh, M.; Mukai, T. High-power InGaN/GaN Double-heterostructure Violet Light Emitting Diodes. *Appl. Phys. Lett.* **1993**, *62* (19), 2390–2392.

(3) Funato, M.; Kaneta, A.; Kawakami, Y.; Enya, Y.; Nishizuka, K.; Ueno, M.; Nakamura, T. Weak Carrier/Exciton Localization in InGaN Quantum Wells for Green Laser Diodes Fabricated on Semi-Polar {20\bar21} GaN Substrates. *Appl. Phys. Express* **2010**, *3* (2), 21002.

(4) Waltereit, P.; Brandt, O.; Trampert, A.; Grahn, H. T.; Menniger, J.; Ramsteiner, M.; Reiche, M.; Ploog, K. H. Nitride Semiconductors Free of Electrostatic Fields for Efficient White Light-Emitting Diodes. *Nature* **2000**, *406* (6798), 865–868.

(5) Fujan, K. J.; Feneberg, M.; Neuschl, B.; Meisch, T.; Tischer, I.; Thonke, K.; Schwaiger, S.; Izadi, I.; Scholz, F.; Lechner, L.; Biskupek, J.; Kaiser, U. Cathodoluminescence of GaInN Quantum Wells Grown on Nonpolar a Plane GaN: Intense Emission from Pit Facets. *Appl. Phys. Lett.* **2010**, *97* (10), 101904.

(6) Wächter, C.; Meyer, A.; Metzner, S.; Jetter, M.; Bertram, F.; Christen, J.; Michler, P. High Wavelength Tunability of InGaN Quantum Wells Grown on Semipolar GaN Pyramid Facets. *Phys. Status Solidi B* **2011**, *248* (3), 605–610.

(7) Cho, C.-Y.; Park, I.-K.; Kwon, M.-K.; Kim, J.-Y.; Park, S.-J.; Jung, D.-R.; Kwon, K.-W. InGaN⁄GaN Multiple Quantum Wells Grown on Microfacets for White-Light Generation. *Appl. Phys. Lett.* **2008**, *93* (24), 241109.

(8) Kang, E.-S.; Ju, J.-W.; Kim, J. S.; Ahn, H.-K.; Lee, J. K.; Kim, J. H.; Shin, D.-C.; Lee, I.-H. Multi-Wavelength Emitting InGaN/GaN Quantum Well Grown on V-Shaped GaN(1101) Microfacet. *J. Nanosci. Nanotechnol.* **2007**, *7* (11), 4053–4056.

(9) Qian, F.; Li, Y.; Gradečak, S.; Park, H.-G.; Dong, Y.; Ding, Y.; Wang, Z. L.; Lieber, C. M. Multi-Quantum-Well Nanowire Heterostructures for Wavelength-Controlled Lasers. *Nat. Mater.* **2008**, *7* (9), 701–706.

(10) Koester, R.; Hwang, J.-S.; Salomon, D.; Chen, X.; Bougerol, C.; Barnes, J.-P.; Dang, D. L. S.; Rigutti, L.; de Luna Bugallo, A.; Jacopin, G.; Tchernycheva, M.; Durand, C.; Eymery, J. M-Plane Core–Shell InGaN/GaN Multiple-Quantum-Wells on GaN Wires for Electroluminescent Devices. *Nano Lett.* **2011**, *11* (11), 4839–4845.

(11) Chang, J.-R.; Chang, S.-P.; Li, Y.-J.; Cheng, Y.-J.; Sou, K.-P.; Huang, J.-K.; Kuo, H.-C.; Chang, C.-Y. Fabrication and Luminescent Properties of Core-Shell InGaN/GaN Multiple Quantum Wells on GaN Nanopillars. *Appl. Phys. Lett.* **2012**, *100* (26), 261103.

(12) Yeh, T.-W.; Lin, Y.-T.; Stewart, L. S.; Dapkus, P. D.; Sarkissian, R.; O'Brien, J. D.; Ahn, B.; Nutt, S. R. InGaN/GaN Multiple Quantum Wells Grown on Nonpolar Facets of Vertical GaN Nanorod Arrays. *Nano Lett.* **2012**, *12* (6), 3257–3262.

(13) Liao, C.-H.; Tu, C.-G.; Chang, W.-M.; Su, C.-Y.; Shih, P.-Y.; Chen, H.-T.; Yao, Y.-F.; Hsieh, C.; Chen, H.-S.; Lin, C.-H.; Yu, C.-K.; Kiang, Y.-W.; Yang, C. C. Dependencies of the Emission Behavior and Quantum Well Structure of a Regularly-Patterned, InGaN/GaN Quantum-Well Nanorod Array on Growth Condition. *Opt. Express* **2014**, *22* (14), 17303–17319.

(14) Fikry, M.; Madel, M.; Tischer, I.; Thonke, K.; Scholz, F. Luminescence Properties of Epitaxially Grown GaN and InGaN Layers around ZnO Nanopillars. *Phys. Status Solidi A* **2011**, *208* (7), 1582–1585.

(15) Fikry, M.; Ren, Z.; Madel, M.; Tischer, I.; Thonke, K.; Scholz, F. Coaxial InGaN Epitaxy around GaN Micro-Tubes: Tracing the Signs. *J. Cryst. Growth* **2013**, *370*, 319–322.

(16) Li, Q.; Xu, S. J.; Li, G. Q.; Dai, D. C.; Che, C. M. Two-Photon Photoluminescence and Excitation Spectra of InGaN⁄GaN Quantum Wells. *Appl. Phys. Lett.* **2006**, *89* (1), 11104.

(17) Jarjour, A. F.; Parker, T. J.; Taylor, R. A.; Martin, R. W.; Watson, I. M. Two-Photon Absorption in Single Site-Controlled InGaN/GaN Quantum Dots. *Phys. Status Solidi C* **2005**, *2* (11), 3843–3846.

(18) Bardoux, R.; Funato, M.; Kaneta, A.; Kawakami, Y.; Kikuchi, A.; Kishino, K. Two-Photon Absorption Induced Anti-Stokes Emission in Single InGaN/GAN Quantum-Dot-like Objects. *Phys. Status Solidi RRL – Rapid Res. Lett.* **2013**, *7* (5), 344–347.

(19) Schmidt, H.; Abare, A. C.; Bowers, J. E.; Denbaars, S. P.; Imamoğlu, A. Large Interband Second-Order Susceptibilities in InxGa1−xN/GaN Quantum Wells. *Appl. Phys. Lett.* **1999**, *75* (23), 3611–3613.

(20) Krishnamurthy, S.; Nashold, K.; Sher, A. Two-Photon Absorption in GaN, GaInN, and GaAlN Alloys. *Appl. Phys. Lett.* **2000**, *77* (3), 355–357.

(21) Thapa, S. B.; Hertkorn, J.; Wunderer, T.; Lipski, F.; Scholz, F.; Reiser, A.; Xie, Y.; Feneberg, M.; Thonke, K.; Sauer, R.; Dürrschnabel, M.; Yao, L. D.; Gerthsen, D.; Hochmuth, H.; Lorenz, M.; Grundmann, M. MOVPE Growth of GaN around ZnO Nanopillars. *J. Cryst. Growth* **2008**, *310* (23), 5139–5142.

(22) Hong, Y. J.; Jeon, J.-M.; Kim, M.; Jeon, S.-R.; Park, K. H.; Yi, G.-C. Structural and Optical Characteristics of GaN/ZnO Coaxial Nanotube Heterostructure Arrays for Light-Emitting Device Applications. *New J. Phys.* **2009**, *11* (12), 125021.

(23) Fikry, M.; Madel, M.; Tischer, I.; Thonke, K.; Scholz, F. Luminescence Properties of Epitaxially Grown GaN and InGaN Layers around ZnO Nanopillars. *Phys. Status Solidi A* **2011**, *208* (7), 1582–1585.

(24) Kohl, D.; Henzler, M.; Heiland, G. Low Temperature Sublimation Processes from Clean Cleaved Polar Surfaces of Zinc Oxide Crystals during First Heating. *Surf. Sci.* **1974**, *41* (2), 403–411.

(25) Wang, Z. L. Zinc Oxide Nanostructures: Growth, Properties and Applications. *J. Phys. Condens. Matter* **2004**, *16* (25), R829.

(26) Boulbar, E. D. L.; Gîrgel, I.; Lewins, C. J.; Edwards, P. R.; Martin, R. W.; Šatka, A.; Allsopp, D. W. E.; Shields, P. A. Facet Recovery and Light Emission from GaN/InGaN/GaN Core-Shell Structures Grown by Metal Organic Vapour Phase Epitaxy on Etched GaN Nanorod Arrays. *J. Appl. Phys.* **2013**, *114* (9), 94302.

(27) Durnev, M. V.; Omelchenko, A. V.; Yakovlev, E. V.; Evstratov, I. Y.; Karpov, S. Y. Indium Incorporation and Optical Transitions in InGaN Bulk Materials and Quantum Wells with Arbitrary Polarity. *Appl. Phys. Lett.* **2010**, *97* (5), 51904.

(28) Sari, E.; Nizamoglu, S.; Choi, J.-H.; Lee, S.-J.; Baik, K.-H.; Lee, I.-H.; Baek, J.-H.; Hwang, S.-M.; Demir, H. V. Opposite Carrier Dynamics and Optical Absorption Characteristics under External Electric Field in Nonpolar vs Polar InGaN/GaN Based Quantum Heterostructures. *Opt. Express* **2011**, *19* (6), 5442.

(29) Garrett, G. A.; Shen, H.; Wraback, M.; Tyagi, A.; Schmidt, M. C.; Speck, J. S.; DenBaars, S. P.; Nakamaura, S. Comparison of Time-Resolved Photoluminescence from InGaN Single Quantum Wells Grown on Nonpolar and Semipolar Bulk GaN Substrates. *Phys. Status Solidi C* **2009**, *6* (S2), S800–S803.

(30) Kim, J.-H.; Ko, Y.-H.; Gong, S.-H.; Ko, S.-M.; Cho, Y.-H. Ultrafast Single Photon Emitting Quantum Photonic Structures Based on a Nano-Obelisk. *Sci. Rep.* **2013**, *3*, 2150.

(31) Prasanth, R.; Vugt, L. K. van; Vanmaekelbergh, D. a. M.; Gerritsen, H. C. Resonance Enhancement of Optical Second Harmonic Generation in a ZnO Nanowire. *Appl. Phys. Lett.* **2006**, *88* (18), 181501.

(32) Zeng, K. C.; Dai, L.; Lin, J. Y.; Jiang, H. X. Optical Resonance Modes in InGaN/GaN Multiple-Quantum-Well Microring Cavities. *Appl. Phys. Lett.* **1999**, *75* (17), 2563–2565.

CHAPTER 5

NONLINEAR LIGHT GENERATION AND LOCALIZATION OF COHERENT SCATTERING IN ZNO SUBMICRON ANTENNAE

5.1 Introduction

Semiconductor structures in a micro-scale with efficient nonlinear optical properties can be used as active elements in photonic applications. Non-centrosymmetric semiconductors exhibiting (1) direct bandgaps, (2) wide bandgaps, and (3) high exciton binding energies, can potentially be utilized for higher-order optical nonlinear light generation. Semiconductors that fit these properties are mainly limited to GaN and its alloys (group III nitrides)[1–3] , ZnSe[4] and ZnO[5–7]. Among the semiconductor compounds with hexagonal crystal lattice structure, GaN is the reference material for solid state lighting applications and is used commercially owing to their wide optical transparency and relatively established growth processes. On the other hand, ZnO has gained a significant place in the solid state lighting research due to its optical properties being very similar to GaN. When the size of the semiconductor structure approaches the wavelength of light, the structure can confine photons realizing interesting optical phenomena.

SHG, a second order nonlinear process, converts two coherent photons with frequency ω to a coherent single photon with frequency 2ω. On the other hand, third order nonlinear processes such as two- and multi-photon transitions can result in photoluminescence and stimulated emission in direct-bandgap semiconductors under the influence of high optical excitation densities[4,8]. Probing nonlinear effects is a challenge due to high incident laser fluences needed to pump the optical medium. Consequently, nonlinear light generation in semiconductor structures has been limited mainly to SHG because second order nonlinearity is more efficient compared to third order nonlinearity. Semiconductor low dimensional structures can sustain much higher optical powers compared to plasmonic structures and hence provide higher nonlinear conversion efficiencies. In addition, nonlinear response from direct bandgap semiconductors is dominated by bulk nonlinearity, whereas indirect bandgap semiconductors and plasmonic structures offer only surface nonlinearities[9]. The application of nonlinear optical properties of semiconductors can technically grant access to a wider spectrum of coherent and non-coherent light generation, extending applications of semiconductor technology.

ZnO, a direct wide bandgap (3.3 eV) semiconductor with high excitonic binding energy of 60 meV at room temperature has shown great potential in previous nonlinear optical studies[7,10–13]. ZnO has a wurtzite crystal structure and belongs to the 6mm point group, which leads to three components of the second-order nonlinear susceptibility, d_{131}, d_{311}, and d_{333}[14].The large second-order nonlinear coefficients and wide transparency range make ZnO a good candidate for SHG from the infrared to the near-ultraviolet region[11,12].

In this chapter, the nonlinear response of vertically standing ZnO submicron rods (SMRs) that are grown on the apex of GaN micro-pyramids was investigated. Femtosecond pulsed near infra-red (NIR) light tightly focused through a high numerical aperture (NA) objective was used to achieve high resolutions with confocal sectioning. Nonlinear light generation processes such as SHG and MPL were observed. Tunability of SHG was tested for a range of excitation wavelengths near and below half the bandgap energy of ZnO. The intensity of SHG and multiphoton induced photoluminescence along the longitudinal axis of the ZnO on GaN pyramid structure is presented. The results show that the UV emission (UVL) due to multi-photon excitation is more efficient at 720 nm fundamental excitation, whereas the SHG in the backward direction is observed to be maximum at 780 nm fundamental excitation. The power dependence of the light generated/emitted from the pyramid was studied at various frequencies to analyze the origin of the nonlinear optical processes from ZnO SMRs. Dependence of nonlinear light intensity radiated was measured as a function of the polarization angle of fundamental excitation.

5.2 Experimental

5.2.1 Sample Preparation

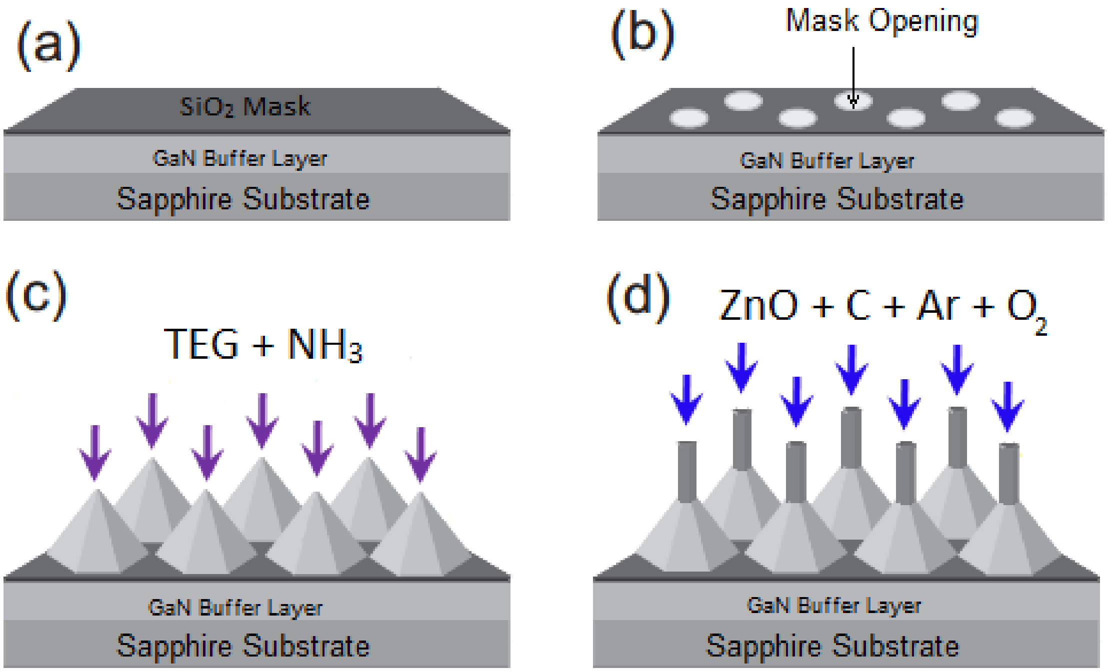

Figure 5.1. Schematics of the multi-step growth process of ZnO on GaN micro-pyramids. (a) Epitaxial growth of a 1 µm GaN buffer layer on Sapphire substrate with SiO2 mask layer, (b) Patterning of mask with circular openings for GaN overgrowth, (c) MOCVD growth of GaN micro-pyramids and (d) Selective growth of ZnO on the apex of GaN micro-pyramids [adapted from Hong et al., 2007 [15]].

Position controlled growth of ZnO SMRs are achieved via a hetero-epitaxial growth process. Because both ZnO and GaN have same crystal symmetry with a low lattice mismatch of 1.9%, hetero-epitaxial growth of ZnO on GaN and vice versa can be achieved. Therefore, ZnO rods with c-axis orientation can be grown on the c-plane (0001) of GaN. The multi-step hetero-epitaxial growth process used to prepare ZnO SMRs is presented in figure 5.1.

In the first step, the arrays of GaN micro pyramids were prepared using selective area epitaxial layer overgrowth (SA-ELO) as discussed in chapter 3 in a low pressure MOCVD system. In this fabrication process, a 1 µm GaN buffer layer was deposited on a c-plane sapphire substrate. A 200 nm silicon dioxide (SiO_2) masking layer was deposited on the GaN epilayer using plasma enhanced CVD process to serve as a growth mask for position controlled selective growth of GaN micro-pyramids. An array of circular windows with a diameter and pitch of 3 µm and 10 µm was fabricated by optical lithography and dry etching techniques. GaN micro pyramids were then selectively grown on the patterned substrate in a MOCVD chamber at 1050^{0} C with ammonia (NH_3) and triethylgallium (TEG) as reactants with hydrogen as carrier gas. By controlling the growth kinetics, plateaus can be formed at the apex of GaN pyramids, which provides selective growth on the top of the pyramid apices compared to facets. The plateaus formed have (0001) orientation. ZnO rods with c-axis orientation can be grown on c-plane (0001) of GaN. The smaller plateaus on the apex of GaN pyramid allow the growth of single ZnO rods[15] on the pyramid apex. In the second step, ZnO SMRs were grown on the top of GaN pyramids using vapor transport method, where the terminated top surface plane of patterned GaN pyramids provided growth selectivity. Single ZnO SMRs were grown with a ZnO/carbon mixture as source material together with oxygen and argon as carrier gas in a CVD process. The rods were grown in a tube furnace at 850 ^{0}C and a pressure of 950 hPa. The resultant selective growth of ZnO SMRs on GaN pyramids is critically dependent on the surface energy difference between the surfaces of the GaN pyramid and the surfaces of ZnO[15,16].

5.2.2 Sample Characterization

Field emission scanning electron microscopy (FESEM) was used to investigate the morphology of ZnO SMRs. The nonlinear optical properties of individual ZnO SMRs were studied using nonlinear microscopy. Multi-photon excitation was achieved using a femtosecond tunable Ti: Sapphire laser (Mai Tai, Spectra Physics) with emission wavelength ranging from 700 nm-1000 nm, pulse width of 100 fs and repetition rate of 80 MHz. The excitation wavelengths for multi-photon experiments were chosen to be in the range of 720nm to 900nm to achieve above, below and ZnO bandgap excitation energies. A variable attenuator was used to control the input power to the sample. Individual ZnO SMR measurements were made using multi-photon microscopy setup using a spot size of ~ 600 nm with a 0.9 NA objective lens. Nonlinear light generation was measured using a thermo-electric cooled CCD detector coupled to the microscope. Polarization dependence of nonlinear response was measured as a function of the linear polarization angle of the fundamental wave (FW). This was achieved by rotating the polarization of FW in the plane perpendicular to the propagation axis by a half wave plate. The nonlinear optical light generated from the ZnO/GaN structures was collected by the same objective and was isolated from the FW using a combination of dichroic mirror and 350 - 650 nm band pass filter.

5.3 Results and Discussion

Figure 5.2 (a) and (b) show the SEM micrographs showing the top and side view of an array of ZnO SMRs on GaN micro-pyramids. The ZnO SMRs shows excellent controlled growth on the apex of micro-pyramids. As seen from the SEM images, the diameters of ZnO SMRs vary from 300 nm to 900 nm. The larger deviation in the diameter of ZnO SMRs is due to the possible deviation in the sizes of plateaus on the apex of the GaN micro-pyramid. The heights of the ZnO SMRs are determined to be about 4.0 to 4.5 µm, whereas the heights of GaN micropyramids are determined to be 3 µm. The energy dispersive spectrum as displayed in figure 5.2 (c) confirms the presence of ZnO. This growth method demonstrates high selectivity of ZnO SMRs, while the density and size of ZnO SMRs can be controlled by changing the pitch and size of GaN micro-pyramids.

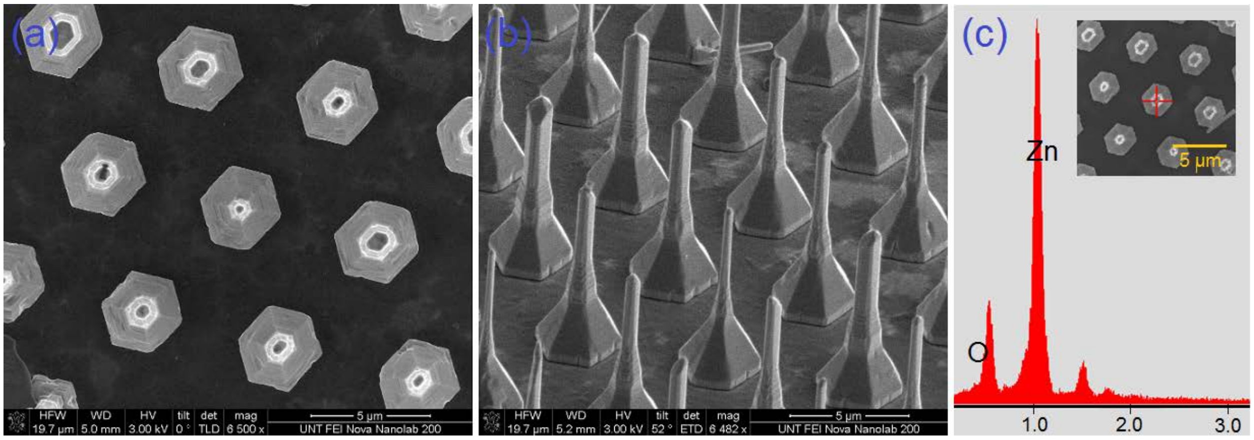

Figure 5.2. SEM images of ZnO submicron rods on GaN micro-pyramids grown on sapphire. a) Top view of an array of ZnO SMRs on GaN micro-pyramids, b) Tilted view of an array of GaN micro-pyramids and c) Energy Dispersive X-ray Spectroscopy of the ZnO SMR showing the presence of zinc and oxygen. The scale bar used in all images is 5 µm.

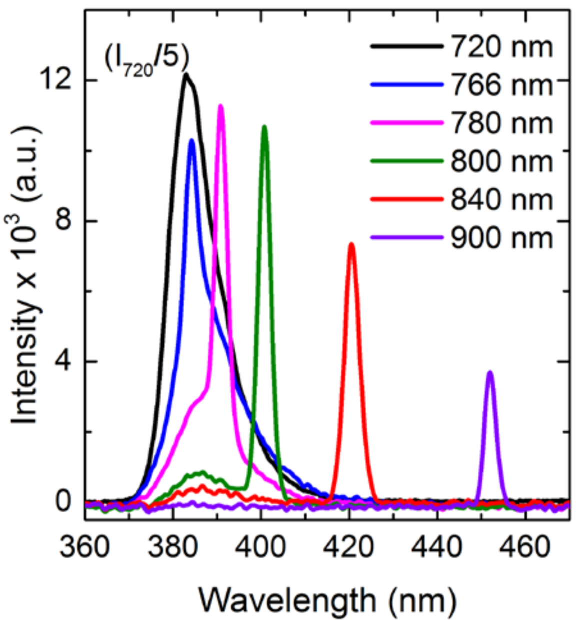

Figure 5.3. Nonlinear light emission from ZnO SMRs. Multiphoton induced photoluminescence spectra from a single ZnO SMR excited by a femtosecond laser at 720 nm (black), 766 nm (blue), 780 nm (pink), 800 nm (green) 840 nm (red) and 900 nm (violet) showing UV luminescence and second harmonic generation. The spectra were measured at 300 K at approximately a power of 10 mW.

The nonlinear light generated by individual ZnO SMRs are shown in figure 5.3 pumped by a femtosecond near IR laser at 720 nm, 766 nm, 780 nm, 800 nm, 840 nm and 900 nm (1.72 eV, 1.62 eV, 1.59 eV, 1.55 eV, 1.48 eV and 1.38 eV) wavelengths from the same ZnO rod at the apex of the pyramid at approximately the same power. Two major peaks were observed in the nonlinear spectra. The broader UV peak at 385 nm is attributed to the recombination of excitons through the exciton-exciton collision process[17,18], while the narrow peak represents the SHG peak. The measured UV peak intensity with 720 nm excitation is approximately five times larger compared to other excitations with energies near band gap. This is believed to be due to strong reabsorption of SHG generated above the band gap of ZnO. As the excitation wavelength is increased, the UV emission intensity decreases. This is because luminescence due to third order nonlinearity is larger near the resonance of the semiconductor crystal. On the other hand, SHG shows a maximum intensity for excitation wavelength at 780 nm. The SHG peak maximum wavelength varies between 376 nm to 405 nm[7,10,18,19] in ZnO nanowires compared to observed 390 nm in this work, which can be attributed to the size and crystalline quality of ZnO wires. The variation in SHG peak maximum may be attributed to the differences in orientation of ZnO crystal axes with respect to incident and polarization angles of excitation among the various studies. A visible luminescence peak centered at 550 nm with an intensity of an order lower than UV emission was observed for 720 nm to 760 nm excitations, which could be excited via the relaxation of the excitons due to the presence of deep center defects in the crystal.

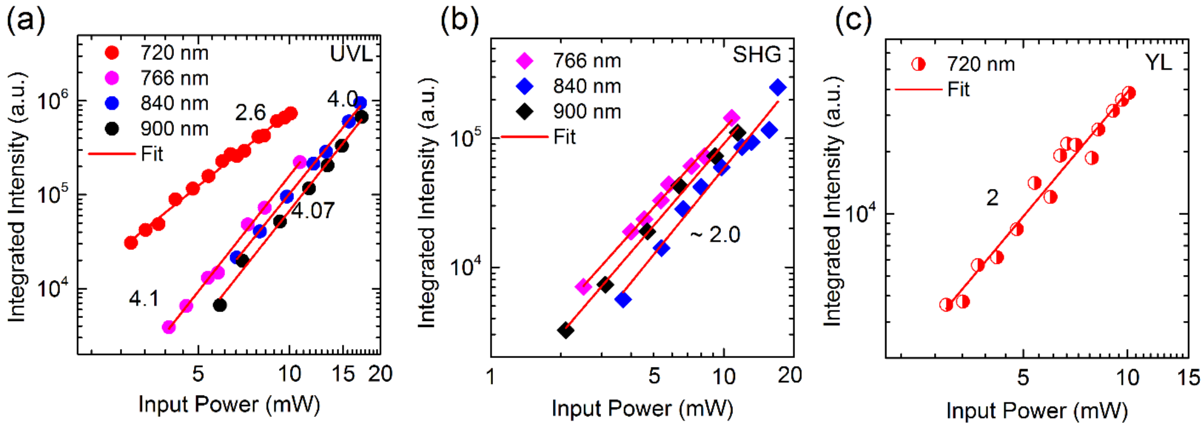

Figure 5.4. Excitation intensity dependence on multiphoton luminescence and SHG. a) Ultra-violet luminescence peak dependence on 720, 766, 840, and 900 nm, b) SHG dependence on 766, 840 and 900 nm and c) Yellow luminescence peak dependence on 720 nm excitation.

The integrated intensities of UV emission and SHG and yellow luminescence were measured as a function of the incident power of the fundamental wavelengths of pumping laser, respectively. Figure 5.4 represents the experimental results for multiple excitation wavelengths. The SHG intensity has a quadratic dependence on the incident power, which agrees well with the

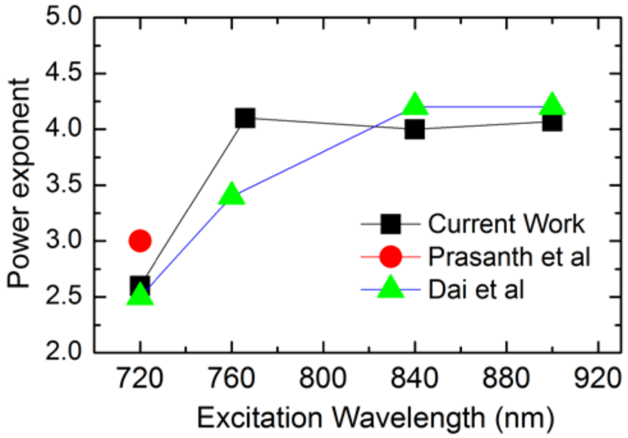

Figure 5.5. Comparison of the dependence of excitation power on the integrated intensity of UV emission to previous work. Black squares represent the power exponent value deduced from the power dependence study of this work, Red circles represent the value extracted from ref [19] and Green triangles represent the value extracted from ref [11].

theoretical dependence of SHG intensity to pump intensity, I_{pump}^2. The power dependence of exciton peak varies from 2.6 (see figure 5.4 a) for 720 nm excitation to 4.0 (see figure 5.4 a) for 766-900 nm excitation. This contradicts the expected quadratic or cubic dependence on pumping intensity for the range of pump wavelengths used. A power exponent of 2.6 at 720 nm pump wavelength could mean that the UV emission is induced by a co-existence of two- and three-photon transition; however, an exponent of 4.0 for 766-900 nm excitation suggests a four-photon transition of incident photons. Power exponent values contradictory to the theoretical power dependence on nonlinear emission was observed in a 1 mm thick ZnO single crystal[11] and a 100 nm thick, 10 µm long ZnO nanowire[19] as shown in figure 5.5. The deviation of the power exponent values in ref 11 (Dai et al) from the expected values was attributed to the contribution of the defect states inside the bandgap in the multiphoton transition. In this work, the yellow luminescence peak intensity dependence on excitation power at 720 nm excitation show a value of 2.0, which shows the presence of a two-photon transition process in the band gap, where the excited carriers can relax to the YL band emitting luminescence. This is a clear evidence that there is a two-photon process involved in the band gap at 720 nm excitation, which concurs with the coexistence of the two- and three- photon processes involved as observed by the power exponent for the UV emission peak at 720 nm excitation. The four-photon transition observed here for UV emission band for excitations in the 766 nm – 900 nm wavelength range needs further investigation.

A qualitative explanation for the deviation in power exponent is provided below. A simplified three-level model as shown in figure 5.6 is used to express the multi-photon transitions, non-radiative relaxations, UV emission and second harmonic generation from the ZnO SMRs. Selection rules as discussed in section 2.5.2 mentions that two-photon transitions are allowed between states with same parity. However, this holds true only for centrosymmetric crystals, whereas in noncentrosymmetric crystals parity selection rules are not valid. Therefore, exciton states allowed in single-photon transition can also be observed in two-photon transition; hence, a large number of possible excitonic states can be reached via two-photon transition. ZnO being a noncentrosymmetric crystal, parity rules cannot be used to explain what is expressed in figure 5.6.

An alternate explanation for the deviation in the power exponent value is discussed below. The nonlinear response in an optical medium is usually triggered with high intensity laser beam. Semiconductors excited under such conditions create many particles such as electron-hole pairs in high density; and the nonlinearities arise due to the interaction between these many particles. Such interactions include elastic and inelastic scattering between excitons, and between excitons and free carriers. Consequently, phenomena such as collision-broadening of the exciton

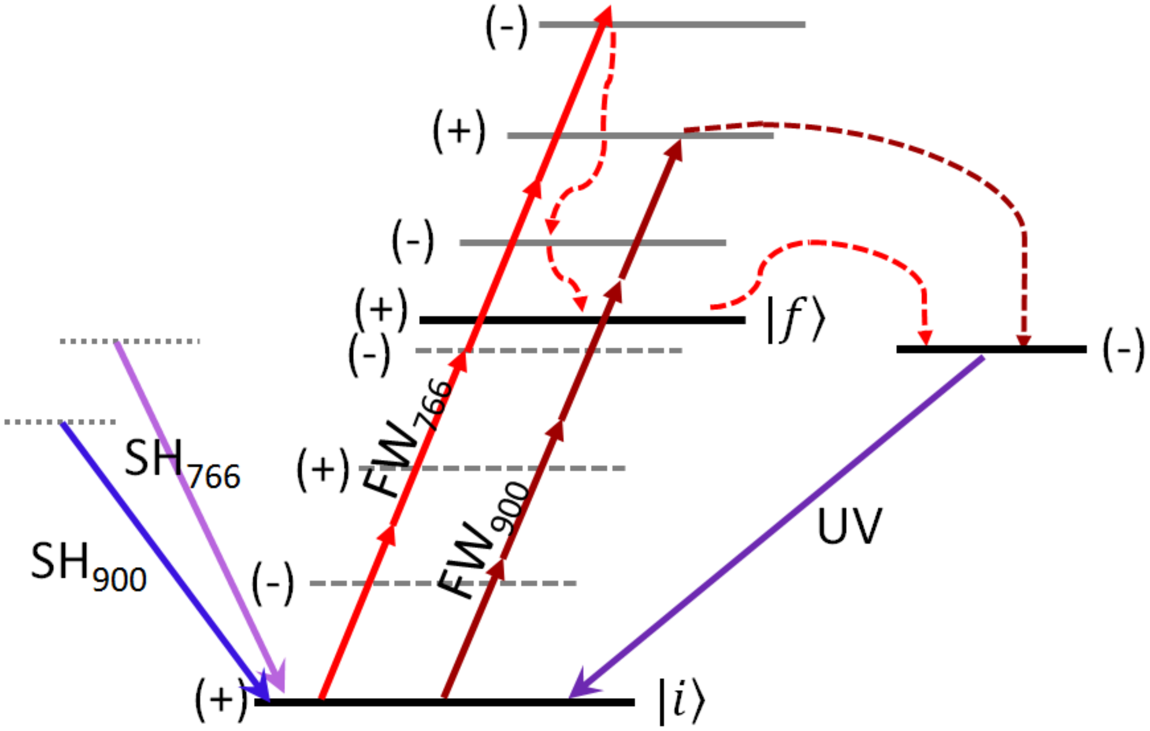

Figure 5.6. Schematic illustration of a three-level system displaying both multi-photon induced UV emission and second harmonic generation. Red shaded arrows represent an ultrafast laser excitation pulse with wavelengths 766 nm and 900 nm coupling the ground state |i> to an excited continuum by four-photon absorption through intermediate levels and relaxation to a final excited state |f> via phonons. Second harmonic radiation is emitted from state via two-photon transition of corresponding pump wavelengths. Excited carriers in state |f> return to the ground state radiating UV luminescence.

resonances, appearance of new luminescence bands, excitation induced increase of absorption, bleaching, two-photon absorption, optical amplification and biexcitons[20]. These effects fall under the intermediate density regime. Increasing the pump intensity would push the excited semiconductor material into the high density regime, where the excitons are in a collective phase known as electron-hole plasma resulting in changes of the optical properties. In this high density regime, phenomena such as Rabi flopping (coherent flipping of carrier population between ground and excited states during a laser pulse with only a few cycles of light), higher harmonic generation and generation of plasma at the surface or bulk[20]. The carrier densities created by the multi-photon excitation energies used in this study are of the order of 10^{22} to 10^{23} cm^{-3}. In ZnO, such carrier densities represent intermediate to high density regime. In contrast, micro-cavities using wide band gap materials like ZnO[21,22] were designed to study the strong coupling between excitons and photon modes at room temperature owing to the stable excitons at room temperature. Progress has been made in developing two-photon pumped stimulated emission from ZnO single crystals due to inelastic exciton-exciton scattering at a lower pump density compared to single-photon pumping[23]. Intense off-resonance femtosecond pulse excitation was found to result in the intense light-matter interaction that would result in strong two-photon Rabi oscillation which could effectively assist in the TPA process[18]. All these complex processes can result in a superlinear power dependence on excitation power density.

Cooperative emissions such as super-radiance and super-fluorescence are classified as coherent emissions, and arise when a collection of dipoles oscillating in phase radiate coherently. The coherence of the radiation is lost when the dipole dephasing sets in. The coherent radiation is proportional to the square of the number of dipoles per unit volume, N^2, while the incoherent emission (spontaneous emission) is proportional to N[24]. When the pump density increases, the value of N increases. For values of N>>1, the emission becomes coherent and is much stronger than its incoherent counterpart and is called super-radiation. Super-radiance is defined as the emission of a macroscopic dipole, which is formed by excitons in a correlated state; whereas, in super-fluorescence, there is no initial macroscopic dipole which causes a delay between the super-fluorescence emission peak and the excitation pulse[25]. Additionally, in semiconductors, the radiative decay rate of cooperative emissions is proportional to the number of excitons[26]. Under an intense ultrashort pulsed laser excitation, the correlation of excitons can complete the process of super-radiance before getting destroyed by the phonons and can be easily achieved in nanostructures. For super-radiance, the emission peak intensity I_{em} is exponentially proportional to the pump density I_p; whereas, the emission decay time decreases with higher pump density[26]. Perhaps, the higher exponent value observed suggests coherent radiation due to cooperative interaction of the electron-hole carriers created by the intense pulse laser pumping of the ZnO SMRs.

Spatial mapping of nonlinear optical response in the axial direction of a single ZnO SMR on GaN pyramid was performed to study the light-matter interaction and behavior of ZnO SMR as an antenna. Two-dimensional maps of multi-photon induced luminescence and second harmonic generation along the longitudinal axis of a single ZnO SMR with six excitation wavelengths are presented in figure 5.7. The nonlinear optical signal generated from a single ZnO SMR/GaN pyramid structure is collected in the backscattered geometry. The integration times used for collecting spectra were kept constant, and the excitation wavelengths were maintained at the same input power density. The spatial measurements show significantly different profiles for resonant and off-resonant excitations. For excitations with energies close to resonance energy of the band gap of ZnO, i.e. at 720 nm, strong UV emission due to the enhanced third order susceptibility is observed. One can also observe the presence of green luminesce in low intensity in figure 5.7 b. This defect peak was only observed for 720 nm excitation denoting an excitation requirement into the continuum of the conduction band. The intensity of the excitonic peak at 385 nm was observed to be maximum at the tip of the ZnO SMR for all excitation wavelengths. A less intense excitonic peak was observed towards the bottom of the ZnO SMR close to the

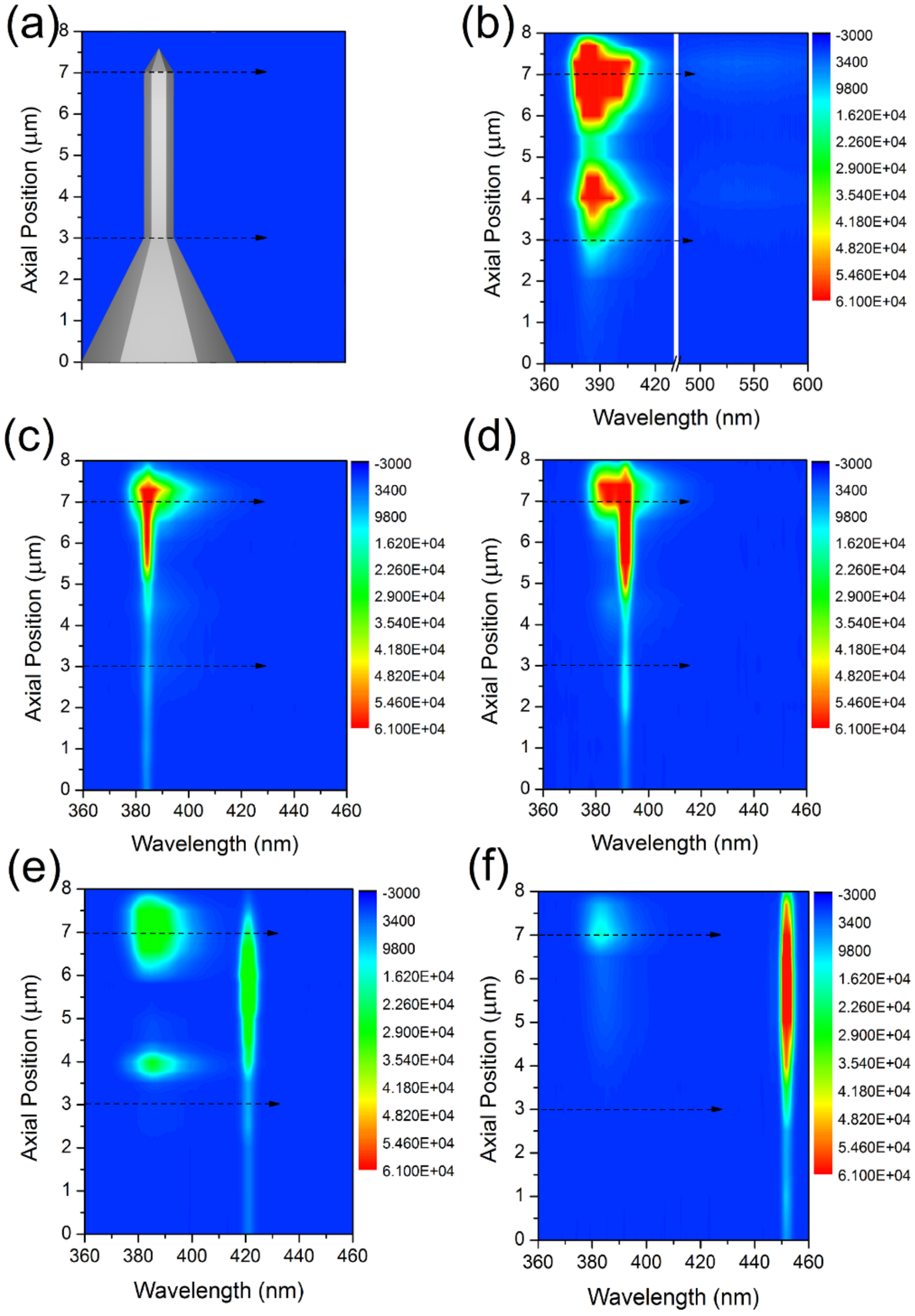

Figure 5.7. Two dimensional plots of line scan of multi-photon induced luminescence and second harmonic generation along the longitudinal axis of a single ZnO SMR. a) Two dimensional image of a ZnO SMR on a GaN micro-pyramid. The arrows show approximately the top and bottom of the ZnO SMR. Spatially dependent light generation from pyramid using b) 720 nm excitation, c) 766 nm excitation, d) 780 nm excitation, e) 840 nm excitation and f) 900 nm excitation. The spectral maps were measured at 300 K and a constant power of 15 mW. The intensity of image (f) is intentionally enhanced by five times in intensity for clarity.

ZnO/GaN interface. ZnO nano- and micro-rods have been demonstrated as laser resonator for guided modes[27,28] and as gain medium for stimulated emission[29,30]. While Fabry-Pérot resonance modes can occur in rod-like structures, it is unlikely to observe this phenomenon in the ZnO SMRs presented here due to non-flat rod ends. However, these ZnO SMRs can support guided modes along the axis of the rod and offer a larger overlap of the guided modes with the optical medium. The less intense UV emission mode observed at the ZnO SMR/GaN pyramid interface could either be due to the increased collection efficiency owing to the subtle change in refractive indices between the two materials resulting in losses at the interface. It could also be due to the tip enhanced effect from the embedded apex of the pyramid at the ZnO/GaN interface. The pyramid-like top surface of the ZnO SMRs may lead to large optical losses in these structures increasing the threshold for lasing. Nevertheless, it can be seen from the spatial maps that the generated UV light and SHG is guided through the axial dimension of the rod toward the tip.

The radiation pattern of the SH field depends on the mode that is excited by the nonlinear polarization induced by the fundamental mode[31]. This is easily achieved either by changing the polarization of the pump beam or the direction of propagation. SH field is known to have volume and surface components and is often determined by the dipole and quadrupole symmetries of the radiation[32]. Here, the nonlinear response of a single ZnO SMR was investigated by changing the pump polarization state to exploit the anisotropy of the ZnO crystal. Figure 5.8 b and c shows the nonlinear response of multiphoton luminescence and SH radiation as a function of the pump polarization along the axis of the ZnO/GaN structure similar to the one shown in figure 5.8 a. The incident Gaussian beam was propagating along the –z axis direction, and the electric field polarization was varied in the xy plane. The 0-degree angle in the polar plot corresponds to the

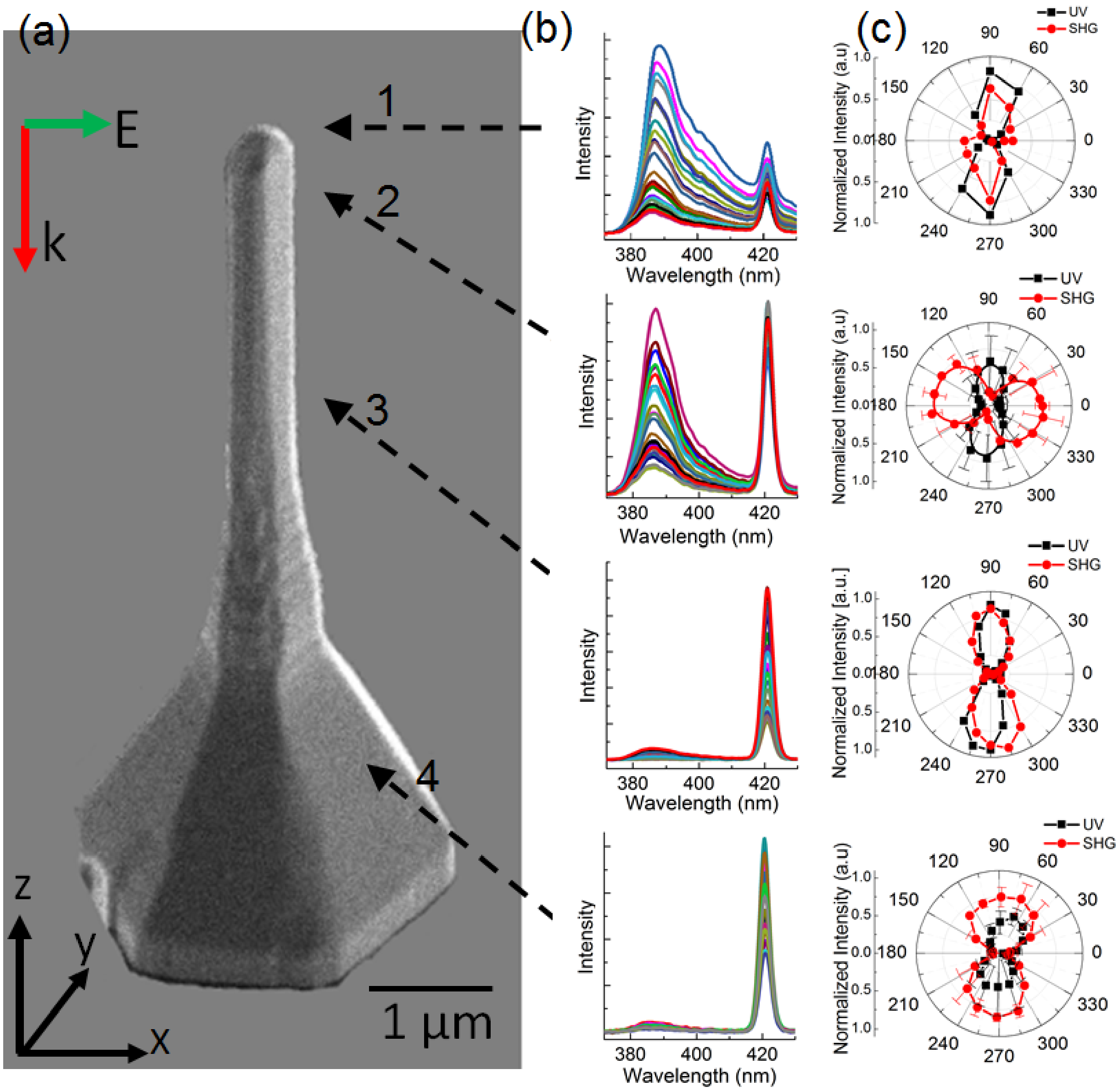

Figure 5.8. Radiation pattern of nonlinear light generation from ZnO SMRs on GaN micro-pyramids with λ_{pump} = 840 nm. (a) ZnO SMR structure, (b) Nonlinear light radiation spectra from the structure, (c) corresponding polar plots of UV emission and SHG on the angle of pump polarization.

pump polarization along the X axis as seen in figure 5.8 a. A pump wavelength of 840 nm was used for the measurements such that there is clear distinction between the MPL and SHG peaks. Here, MPL stands for the UV emission induced by the multiphoton absorption. The arrows in figure 5.8 shows the approximate axial position where the pump beam was focused and the output was collected. From figure 5.8, it can be observed that the UV emission and SHG are highly dependent on the pump polarization. The spatial measurements in figure 5.7 showing brighter UV emission at the tip of the ZnO rod was taken with excitation with circular polarization. In figure 5.8, a similar trend with strong UV emission is observed at the ZnO tip for linear pump polarization varying in xy plane. Position labeled ‘1’ is measured from the extreme tip of ZnO rod. Position labeled ‘2’ is measured from within the first 500 nm from the tip. Position labeled ‘3’ is measured from the inside of the ZnO rod and position labeled ‘4’ is obtained from the bulk of the GaN pyramid. The polar plots show that both UV emission and SHG have dipole symmetries; and is attributed to bulk nonlinearity from ZnO rod.

ZnO, being a member of 6 mm crystal group symmetry lacks inversion symmetry; hence, dipole dominant processes are dominant than higher order multipole processes such as electric quadrupole processes. The results presented in figure 5.8 concurrently shows dominant dipole radiation processes. The polar plots show the same directionality for both UV and SH fields for positions 1, 3 and 4, which shows they are polarized mostly in the y direction with respect to the lab frame as shown in figure 5.8 a. On the contrary, the polar plot showing UV and SH fields from position 2 although dipole in nature shows a “flip” in the symmetry of the dipole pattern. A significant trend in the co-existence of UV and SH radiation intensities can be observed from the emission wavelength vs intensity spectra profiles in 5.8 b. The data lines in the spectra graphs in figure 5.8 b, although not labeled, show the intensities of peaks collected as the FW linear polarization state was varied in the XY plane. Comparing the spectra for all four positions, it can be noticed that the intensity of the UV peak and the SHG peak has a drastic variation from a maximum to minimum corresponding to the angle variation, with one being clearly dominant over the other. However, in the case of position 2, this is not completely true. Although the UV emission peak shows a significant variation in intensity when the pump polarization is rotated from x to y direction, both peaks seem to be rather dominant. This means that nonlinear phenomena corresponding to third and second order nonlinearities are dominant. In other words, there is a competition between the two higher order nonlinear processes at this position due to localization of electric fields as evident from the spatial maps could be leading to the "flipping" of the dipole symmetry of SH radiation.

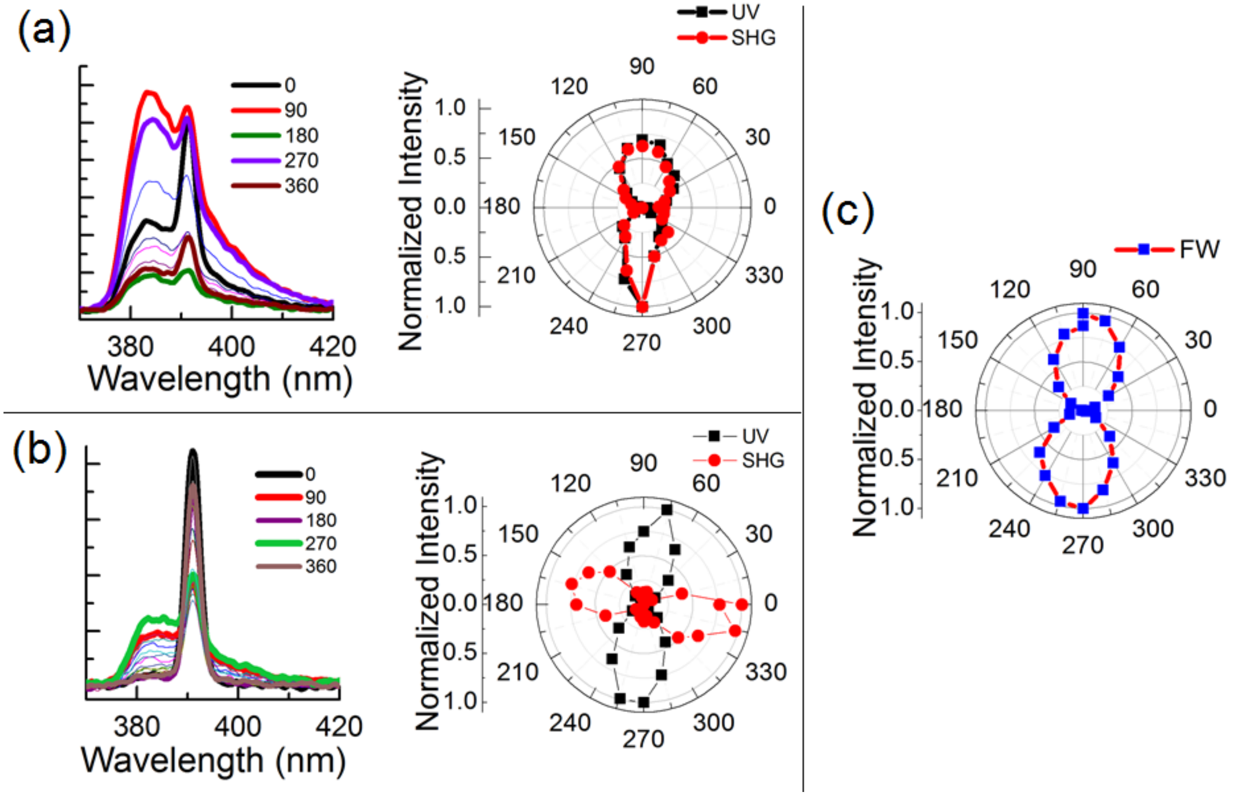

Figure 5.9. Nonlinear light radiation spectra from the ZnO SMR/GaN pyramid structure with 780 nm pump field. (a) Spectra collected from an axial position similar to position '1' in figure 5.8 and its corresponding polar plot of UV emission and SHG vs pump polarization, (b) Spectra collected from an axial position similar to position '2' in figure 5.8 and its corresponding polar plot of UV emission and SHG vs pump polarization, and (c) polar plot of scattered intensity of pump field from the ZnO rod as a function of pump polarization angle.

The polar plots were also measured for two other excitation wavelengths to study the dependence on excitation wavelength especially at the wavelength where maximum SHG was observed. The flipping of SHG dipole maximum was observed for excitations at 780 nm and 766 nm and therefore can be assumed to be independent of excitation wavelength. Figure 5.9 shows the nonlinear spectra and their corresponding polar plot for two axial positions for excitation wavelength at 780 nm. Figure 5.9 c shows the polar plot of the scattered pump intensity from the ZnO rod, while rotating the pump polarization in the XY plane. It appears that scattered pump field is preferentially aligned along the Y axis in the lab frame. A lower pump power (about one-half of the power used in figure 5.8) was used here to reduce the contribution of third order nonlinearity to the overall optical response as can be seen in figure 5.9 b. Nevertheless, the SHG polar response was phase shifted by 90 degrees. Therefore, the competition between the higher order processes may not be responsible for this phenomena.

The SHG response is extremely sensitive to the polarization angle of the pumping light with respect to the crystallographic orientation of materials[33]. This polarization dependence arises due to the nonlinear properties of the material that are determined by the second-order susceptibility tensor $\chi^{(2)}$. The elements of the $\chi^{(2)}$ tensor are defined by crystallographic point groups, and they are different for different crystal structures[34]. It has been shown that using second harmonic generation microscopy, crystallographic directions of a semiconductor crystal can be precisely measured[33,35]. A tilt in the c-axis of the crystal from the propagation axis was reported to offset the SHG polar phase previously[33]. Additionally, SHG polarimetry allows to make a distinction between multiple crystal phases[36]. Inadvertent changes in flux ratio or growth temperature during nano and micro-rod growth can result in a deviation of wurtzite crystal phase to zinc blende phase. ZnO SMRs in this study are oriented in the c axis direction, which is the dominant growth direction of a wurtzite crystal using vapor transport method. The variations in the shapes of the polar plots determine the transitions in the crystal structure of a material; for example, zinc blend crystal structure produces quadrupole shape and wurtzite crystals produce dipole symmetries. A slight deviation from pure wurtzite crystal structure to a mixture of wurtzite – zinc blende structure resulted in a rotation of the dipole by 45 degrees[36]. As seen from the SEM micrographs, the tips of the rod do not make a polar c-plane or a pyramid like top, which is a signature of wurtzite crystal growth. Also, it can be seen that the ZnO rods are not perfectly hexagonal in shape due to a minor onset of additional facets growth especially towards the top of the rod. The partial dome – pyramid like shape at the top of the ZnO rods in this study is a consequence of the VLS growth where a Ga terminated surface on the GaN pyramid apex was used to grow the ZnO rods. This could mean that either a blend of crystal structure or the asymmetry in the axial geometry may occur resulting in the "flipping" of SH radiation symmetry, and must be verified by high resolution TEM studies.

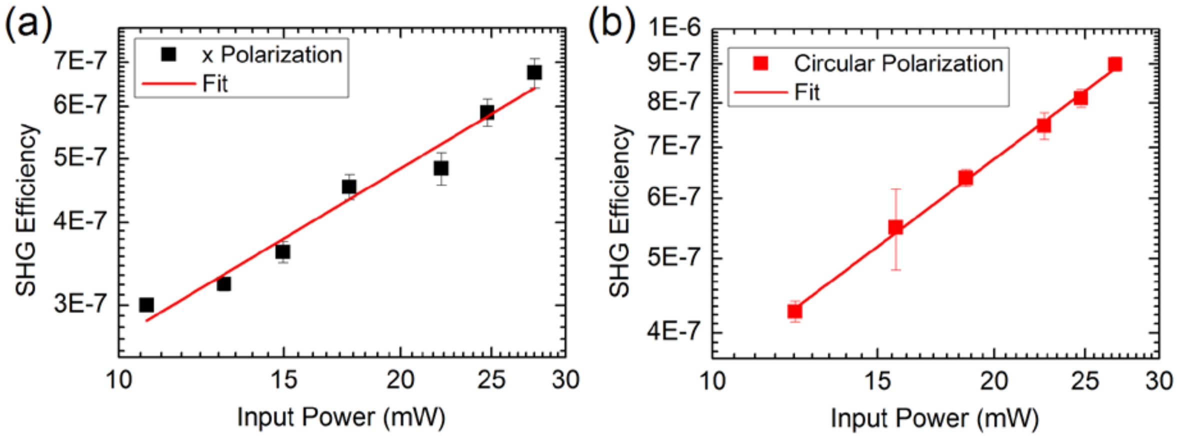

Figure 5.10. SHG efficiency of a ZnO SMR at 420 nm as a function of incident pump power at 840 nm

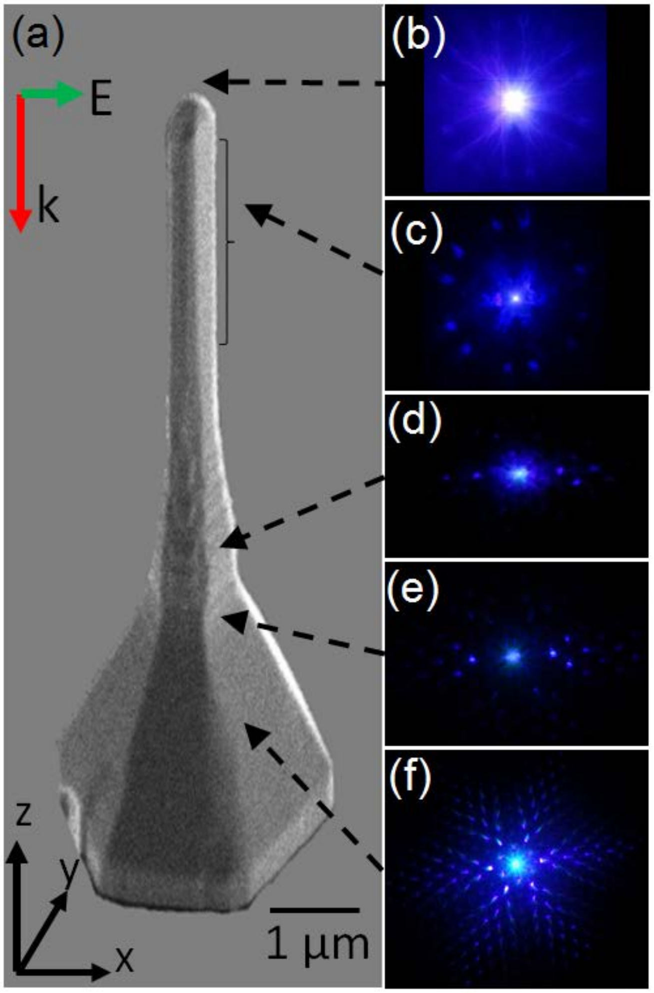

Figure 5.11. Dark field optical images of the nonlinear optical response from the ZnO SMR/ GaN pyramid structure. The images named (b)-(f) are taken by scanning the focus of the laser beam through the symmetric axis of the structure. The arrows represent the axial locations from which the optical images are taken.

The second harmonic field efficiency was measured for two different pump polarizations and is represented in figure 5.10. The efficiency was calculated using the ratio of SH power to pump power. Linearly polarized light in the X direction was chosen as it provided a higher SH signal compared to its counterpart in the Y direction. A pump wavelength of 840 nm was used merely because of the availability of a high performing narrow band pass filter at 420 nm. The nonlinear spectra were filtered to collect just the SH signal using a Pico watt meter. The graphs in figure 5.10 show that SHG efficiency is proportional to the pumping power and is approximately equal to 4 x 10^{-7} and 5 x 10^{-7} for a pump power of 15 mW.

The optical images pictured in figure 5.11 shows that nonlinear light radiated from the ZnO/GaN rod/pyramid structure is extremely directional. As the geometry of the structure changes, so does the directionality of the radiated light. The pump laser is pumping only the center bright structure. It appears that at the rod/pyramid interface, there is some loss in directionality probably created by the stacking fault like defects. Localization of radiated photons can be clearly observed in figures 5.11 c and f. This is believed to be caused by multiple coherent scattering and the constructive interference of the scattering paths. The constructive interference of coherent scattering can create strongly correlated photon modes (modes with SHG frequency in this case) resulting in the enhancement of the SHG. Localization of SHG in space and time using ultra short femtosecond pulsed laser using 30-100 nm randomly oriented ZnO nano needles was observed[6]. The position control attained in the samples under study achieved via SAG method provides an additional controllability of the scattering.

5.4 Conclusions

The array of ZnO sub-micron rods was fabricated using selective area growth and excellent position controlled growth was achieved. NLO light generation was observed in ZnO SMRs for excitation wavelengths ranging from 720 nm to 900 nm. Multiphoton transition induced by tightly focused femto-second NIR radiation results in an excitonic UV emission at 385 nm and was observed for energies below and above the half bandgap energy and half the exciton transition energy. SHG was also observed from these pyramids for excitation below the band gap energy. The UV emission due to 2PA is stronger at the interband resonance when the energy of incident field corresponds to half the bandgap energy of ZnO. A green emission was observed for above band gap energy. The pump intensity dependence on PL shows nonlinear behavior in the absorption process, and the number of photons involved in the transition depends on the excitation energy. A quadratic dependence was observed confirming SHG process as expected. Anomalous power dependence was observed for the UV emission peak and is attributed to a co-operative emission mechanism. Spatial measurements show a localization of UV emission at the ZnO SMR tip and can be clearly seen from the optical image. Besides, the spatial maps show that the generated UV light and SHG is guided through the long axis of the rod toward the tip. The polarimetry of nonlinear light generation from ZnO SMRs show a dipole symmetry for both UV and SHG radiation and is attributed to bulk nonlinearity from the ZnO rod. A "flipping" of SHG radiation symmetry was observed close to the tip of the rod. This could mean that either a blend of crystal structure or the asymmetry in the axial geometry may occur resulting in the “flipping” of SH radiation symmetry, and must be verified by high resolution TEM studies. An SHG efficiency equal to 4 x 10^{-7} and 5 x 10^{-7} was observed for s-polarization and circular polarization, respectively for a pump power of 15 mW. Localization of radiated photons was observed in the ZnO SMR array and is believed to be caused by the constructive interference of the multiple coherent scattering paths. The position control attained in the array of ZnO rods via SAG method provides an additional controllability in shaping the propagation of NLO generated light.

5.5 References

(1) Angerer, W. E.; Yang, N.; Yodh, A. G.; Khan, M. A.; Sun, C. J. Ultrafast Second-Harmonic Generation Spectroscopy of GaN Thin Films on Sapphire. *Phys. Rev. B* **1999**, *59* (4), 2932–2946.

(2) Miragliotta, J.; Wickenden, D. K.; Kistenmacher, T. J.; Bryden, W. A. Linear- and Nonlinear-Optical Properties of GaN Thin Films. *J. Opt. Soc. Am. B* **1993**, *10* (8), 1447–1456.

(3) Sun, C.-K.; Liang, J.-C.; Wang, J.-C.; Kao, F.-J.; Keller, S.; Mack, M. P.; Mishra, U.; DenBaars, S. P. Two-Photon Absorption Study of GaN. *Appl. Phys. Lett.* **2000**, *76* (4), 439–441.

(4) Barzda, V.; Cisek, R.; Spencer, T. L.; Philipose, U.; Ruda, H. E.; Shik, A. Giant Anisotropy of Second Harmonic Generation for a Single ZnSe Nanowire. *Appl. Phys. Lett.* **2008**, *92* (11), 113111.

(5) Semin, S. V.; Sherstyuk, N. E.; Mishina, E. D.; Gherman, C.; Kulyuk, L.; Rasing, T.; Peng, L.-H. Mapping of Two-Photon Luminescence Amplification in Zinc-Oxide Microstructures. *Semiconductors* **2012**, *46* (3), 360–362.

(6) Mascheck, M.; Schmidt, S.; Silies, M.; Yatsui, T.; Kitamura, K.; Ohtsu, M.; Leipold, D.; Runge, E.; Lienau, C. Observing the Localization of Light in Space and Time by Ultrafast Second-Harmonic Microscopy. *Nat. Photonics* **2012**, *6* (5), 293–298.

(7) Liu, W.; Wang, K.; Long, H.; Chu, S.; Wang, B.; Lu, P. Near-Resonant Second-Order Nonlinear Susceptibility in c-Axis Oriented ZnO Nanorods. *Appl. Phys. Lett.* **2014**, *105* (7), 071906.

(8) Peyghambarian, N.; Koch, S. W.; Mysyrowicz, A. *Introduction to Semiconductor Optics*; Prentice Hall series in solid state physical electronics; Prentice Hall: Englewood Cliffs, N.J, 1993.

(9) Dadap, J. I.; Shan, J.; Eisenthal, K. B.; Heinz, T. F. Second-Harmonic Rayleigh Scattering from a Sphere of Centrosymmetric Material. *Phys. Rev. Lett.* **1999**, *83* (20), 4045–4048.

(10) Johnson, J. C.; Yan, H.; Schaller, R. D.; Petersen, P. B.; Yang, P.; Saykally, R. J. Near-Field Imaging of Nonlinear Optical Mixing in Single Zinc Oxide Nanowires. *Nano Lett.* **2002**, *2* (4), 279–283.

(11) Dai, D. C.; Xu, S. J.; Shi, S. L.; Xie, M. H.; Che, C. M. Efficient Multiphoton-Absorption-Induced Luminescence in Single-Crystalline ZnO at Room Temperature. *Opt. Lett.* **2005**, *30* (24), 3377.

(12) Abe, M.; Awata, N.; Matsushita, T.; Hakamata, M.; Ozawa, K.; Murakami, R.; Shoji, I.; Kondo, T. Accurate Measurement of Quadratic Nonlinear-Optical Coefficients of Zinc Oxide. *J. Opt. Soc. Am. B* **2012**, *29* (9), 2392.

(13) Bi, Z.-F.; Rodriguez, A. W.; Hashemi, H.; Duchesne, D.; Loncar, M.; Wang, K.-M.; Johnson, S. G. High-Efficiency Second-Harmonic Generation in Doubly-Resonant χ^(2) Microring Resonators. *Opt. Express* **2012**, *20* (7), 7526.

(14) Sutherland, R. Handbook of Nonlinear Optics https://www.crcpress.com/Handbook-of-Nonlinear-Optics/Sutherland/p/book/9780824742430 (accessed Oct 15, 2016).

(15) Hong, Y. J.; An, S. J.; Jung, H. S.; Lee, C.-H.; Yi, G.-C. Position-Controlled Selective Growth of ZnO Nanorods on Si Substrates Using Facet-Controlled GaN Micropatterns. *Adv. Mater.* **2007**, *19* (24), 4416–4419.

(16) Equilibrium Shape of Nano-Cavities in H Implanted ZnO. *Appl. Phys. Lett.* **2015**, *106* (21), 212102.

(17) Klingshirn, C. F.; Meyer, B. K.; Waag, A.; Hoffmann, A.; Geurts, J. *Zinc Oxide*; Springer Series in Materials Science; Springer Berlin Heidelberg: Berlin, Heidelberg, 2010; Vol. 120.

(18) Zhang, C. F.; Dong, Z. W.; You, G. J.; Zhu, R. Y.; Qian, S. X.; Deng, H.; Cheng, H.; Wang, J. C. Femtosecond Pulse Excited Two-Photon Photoluminescence and Second Harmonic Generation in ZnO Nanowires. *Appl. Phys. Lett.* **2006**, *89* (4), 042117.

(19) Prasanth, R.; Vugt, L. K. van; Vanmaekelbergh, D. a. M.; Gerritsen, H. C. Resonance Enhancement of Optical Second Harmonic Generation in a ZnO Nanowire. *Appl. Phys. Lett.* **2006**, *88* (18), 181501.

(20) Klingshirn, P. C. F. High Excitation Effects and Nonlinear Optics. In *Semiconductor Optics*; Graduate Texts in Physics; Springer Berlin Heidelberg, 2012; pp 491–506.

(21) Das, A.; Heo, J.; Bayraktaroglu, A.; Guo, W.; Ng, T.-K.; Phillips, J.; Ooi, B. S.; Bhattacharya, P. Room Temperature Strong Coupling Effects from Single ZnO Nanowire Microcavity. *Opt. Express* **2012**, *20* (11), 11830–11837.

(22) Lai, Y.-Y.; Lan, Y.-P.; Lu, T.-C. Strong Light–matter Interaction in ZnO Microcavities. *Light Sci. Appl.* **2013**, *2* (6), e76.

(23) He, T. C.; Chen, R.; Lin, W. W.; Huang, F.; Sun, H. D. Two-Photon-Pumped Stimulated Emission from ZnO Single Crystal. *Appl. Phys. Lett.* **2011**, *99* (8), 081902.

(24) Shen, Y. R. *The Principles of Nonlinear Optics*; J. Wiley: New York, 1984.

(25) Bonifacio, R.; Lugiato, L. A. Cooperative Radiation Processes in Two-Level Systems: Superfluorescence. *Phys. Rev. A* **1975**, *11* (5), 1507–1521.

(26) Ding, C. R.; Lin, W.; Chen, B. C.; Zhao, F. L.; Dong, J. W.; Shi, M.; Wang, H. Z.; Hsu, Y. F.; Djurišić, A. B. Super-Radiance of Excitons in a Single ZnO Nanostructure. *Appl. Phys. Lett.* **2008**, *93* (15), 151902.

(27) Hauschild, R.; Kalt, H. Guided Modes in ZnO Nanorods. *Appl. Phys. Lett.* **2006**, *89* (12), 123107.

(28) Johnson, J. C.; Yan, H.; Yang, P.; Saykally, R. J. Optical Cavity Effects in ZnO Nanowire Lasers and Waveguides. *J. Phys. Chem. B* **2003**, *107* (34), 8816–8828.

(29) Hauschild, R.; Lange, H.; Priller, H.; Klingshirn, C.; Kling, R.; Waag, A.; Fan, H. J.; Zacharias, M.; Kalt, H. Stimulated Emission from ZnO Nanorods. *Phys. Status Solidi B* **2006**, *243* (4), 853–857.

(30) Gruzintsev, A. N.; Red'kin, A. N.; Makovei, Z. I.; Barthou, C. Spontaneous and Stimulated Emission of Vertically Aligned ZnO Nanorods of Different Lengths. *Inorg. Mater.* **2007**, *43* (10), 1080–1084.

(31) Carletti, L.; Locatelli, A.; Neshev, D.; De Angelis, C. Shaping the Radiation Pattern of Second-Harmonic Generation from AlGaAs Dielectric Nanoantennas. *ACS Photonics* **2016**, *3* (8), 1500–1507.

(32) Cisek, R.; Barzda, V.; Ruda, H. E.; Shik, A. Nonlinear Optical Properties of Semiconductor Nanowires. *IEEE J. Sel. Top. Quantum Electron.* **2011**, *17* (4), 915–921.

(33) Hu, H.; Wang, K.; Long, H.; Liu, W.; Wang, B.; Lu, P. Precise Determination of the Crystallographic Orientations in Single ZnS Nanowires by Second-Harmonic Generation Microscopy. *Nano Lett.* **2015**, *15* (5), 3351–3357.

(34) Boyd, R. W. Chapter 1 - The Nonlinear Optical Susceptibility. In *Nonlinear Optics (Third Edition)*; Academic Press: Burlington, 2008; pp 1–67.

(35) Ren, M.-L.; Agarwal, R.; Liu, W.; Agarwal, R. Crystallographic Characterization of II–VI Semiconducting Nanostructures via Optical Second Harmonic Generation. *Nano Lett.* **2015**, *15* (11), 7341–7346.

(36) Timofeeva, M.; Bouravleuv, A.; Cirlin, G.; Shtrom, I.; Soshnikov, I.; Reig Escalé, M.; Sergeyev, A.; Grange, R. Polar Second-Harmonic Imaging to Resolve Pure and Mixed Crystal Phases along GaAs Nanowires. *Nano Lett.* **2016**, *16* (10), 6290–6297.

CHAPTER 6

SUMMARY AND FUTURE OUTLOOK

6.1 Summary

"The quest for nanoscale light sources with designer radiation patterns and polarization has motivated the development of nanoantennas that interact strongly with the incoming light and are able to transform its frequency, radiation, and polarization patterns"[1]. As mentioned in the introduction to this dissertation, manipulation of electromagnetic waves in the optical regime can be done using the three main entities: photonic crystals, optical cavities and optical antennae. The background and significance of nonlinear optics, especially using semiconductor micro- and nano- structures were established. Manipulation of nonlinear optical phenomena using these three entities made of semiconductor materials enables new functionalities. Towards attaining this broader goal, this dissertation investigated the fundamental nonlinear optical properties from individual semiconductor structures of various shape grown with position control. Mainly three types of structures/geometries made of nitrides and ZnO were studied. NLO light generation was observed in all structures for NIR excitation wavelengths above and below the bandgap of the semiconductors used. The results are summarized below and a graphic representation of the summary of results is depicted in figure 6.1.

Semi-polar GaN micro-pyramidal structures, nonpolar InGaN/GaN multiple quantum well submicron tubes, and ZnO submicron rods on GaN micro-pyramids were fabricated on patterned substrates by MOCVD using ELO growth technique. Excellent position control was obtained to study the optical response from individual structures as fabricated rather than dispersing it on a foreign substrate. Processes such as spontaneous emission, coherent spontaneous emission, and optical frequency conversion were observed in these structures as a result of multiphoton transitions induced by tightly focused femto-second NIR pumping. Spontaneous emission from near band-edge and defect states due to third order susceptibility were observed for moderate-to-high input optical densities for all the structures supported by the pump power dependence on output radiation. The MPL due to 2PA is stronger at the interband resonance when the energy of incident field corresponds to half the bandgap energy of GaN. Similarly, frequency conversion due to second order nonlinearity (SHG) was observed in all structures for below half band gap pumping energies, which showed the typical quadratic dependence. Excitation and collection of the nonlinear response from lower dimensions such as the tip of pyramids and ZnO submicron rods however showed an exponential power dependence than expected values for 2PA or 3PA induced radiation. Utilizing various semiconductor materials for the fabrication of the studied structures allowed the tuning of UV emission peak wavelength. The SHG from these structures, especially the ZnO submicron rod on GaN micro-pyramid structure can be selectively turned on by using a low optical pump density. Increasing pump density from moderate to high power regime increases the UV emission significantly compared to the defect level emission.

The nonlinear response from a 15 μm size GaN pyramid depends on the excitation energy and geometrical position on the micro-pyramid. SHG observed from these structures showed maximum intensity at about 4 μm above the base of the 15 μm pyramid. Quasi-WGM like modes were observed at this axial location of the pyramid for off-resonant excitations and is attributed to the enhanced response of the second order nonlinearity. The axial inhomogeneity in the micro-pyramid provides hexagonal cross-section slices with varying diameters offering flexible

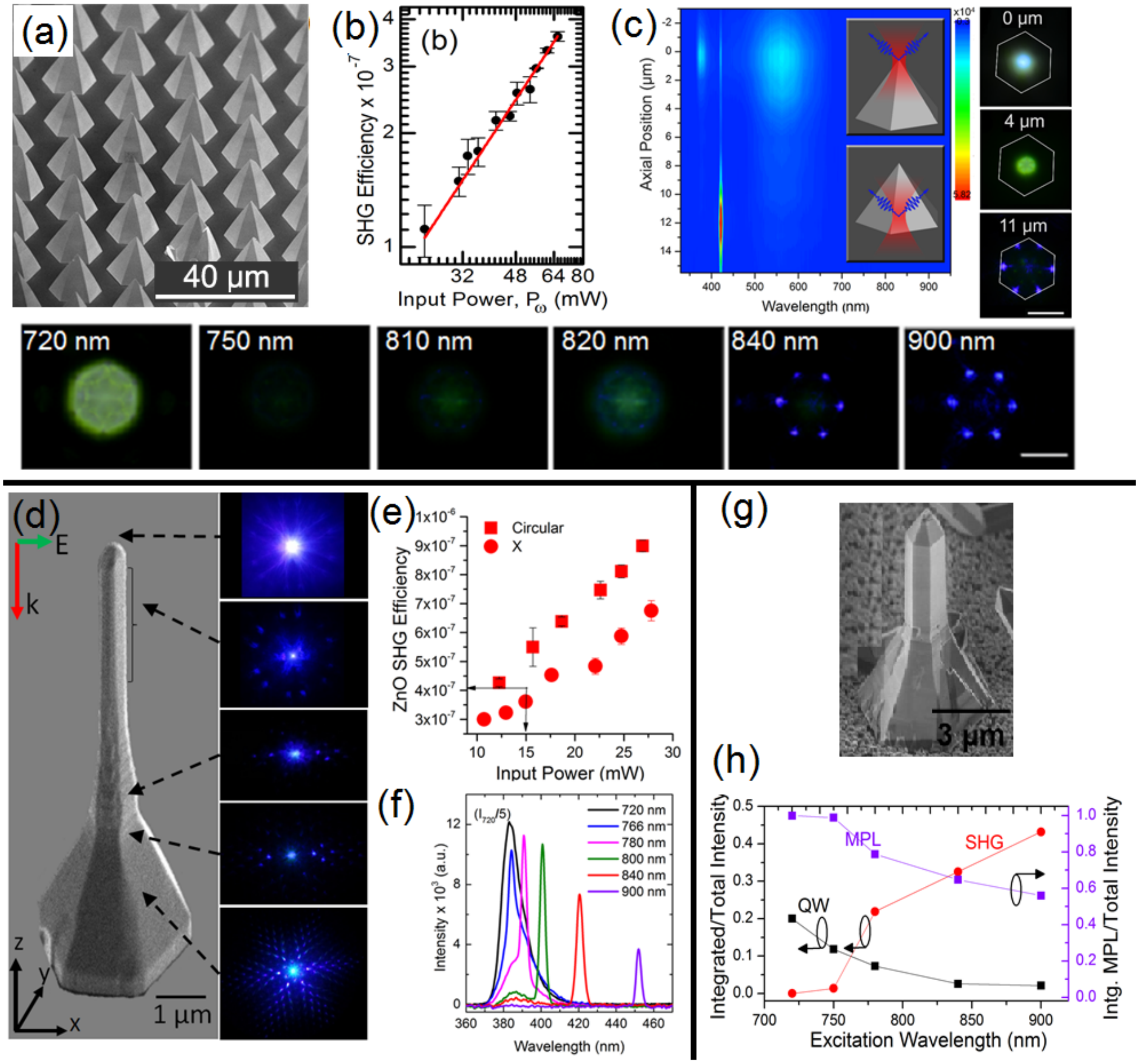

Figure 6.1. Summary of results observed in this dissertation in a nut-shell. Panels (a)-c) summarizes the NLO generation in larger micropyramids. (a) show the larger micro-pyramid arrays fabricated using SAELO method, (b)- SHG efficiency obtained using circular pump polarization and (c)-spatial mapping of GaN micropyramid showing controllable onset of second- and third order nonlinear processes along the axial direction along with the color profile of the emission. The panel images labeled 720 nm – 900 nm represents the NLO generation as a function of the pump wavelength from the axial position where maximum SHG was observed. Panels (d)-(f) show the work from ZnO SMRs. (d)-SEM of a single ZnO SMR along with the coherent scattering patterns as a function of its axial geometry, (e) - SHG efficiency obtained in a single ZnO SMR using two pump polarization states and (f)- the range and spectral profile of NLO generation. Panels (g)-(h) summarizes the findings from InGaN SMTs. (g)- SEM of a single InGaN SMT on a micro pyramid and (h)- the ratio of intensities showing a competition between the second- and third- order NLO processes.

WGM conditions for a range of wavelengths.

The results indicate that GaN micro-pyramids have large optical nonlinearity due to dimensional effects, crystalline quality and cavity formation. Ideally confined WGM modes require a coupled waveguide to extract the light out. The pyramidal shape with inclined facets allows the detection of such modes. However, for 3 µm pyramids, the six bounce modes observed was not confined within a pyramid. Maximum SHG generation in the 3 µm pyramid was unable to determine due to the inhomogeneity of the structures. The larger GaN micro-pyramids allows the control of color temperature and coherence of the light generation by selective onset of the nonlinear process by varying axial excitation of the pyramidal cross-section. In the case of smaller pyramids, no discrete control of the second and third order processes as a function of the axial position were observed. Apices of both the pyramids showed brighter UV emission and is attributed to 1) larger optical nonlinearity due to enhanced dipole moments at the sharp edges and tip and 2) a decrease of the absorption in the bulk during propagation out to the surface. In addition, light generation from the smaller pyramid array created interesting optical scattering patterns that could potentially be used for further studies to manipulate the NLO processes for photonic applications.

High resolution electron microscopy measurements as discussed in chapter 4 demonstrated the growth of InGaN/GaN MQWs on the nonpolar and semi-polar facets of GaN submicron tubes. Time resolved PL measurements show a reduction in the emission decay time for non-polar MQWs compared to polar MQWs confirming lack of strain in the QW/barrier layers reducing the piezoelectric field. Besides STEM measurements, single photon luminescence was performed on the sample during each step of the multi-layer process, which distinctively identifies the luminescence of InGaN/GaN MQWs. Both STEM and optical measurements show a low indium incorporation in the QWs confirming the presence of InGaN/GaN quantum well emission in the UV region. Nonlinear interaction of light in these structures were observed. A two photon excited photoluminescence was observed at room temperature from an InGaN/GaN QW tube at around 390 nm, independent of excitation wavelength. However, the QW emission intensity was maximum close to half the bandgap of GaN. In addition, the second harmonic signal of the excitation laser was also observed at half the wavelength of the fundamental wavelength. Wavelength dependent measurements showed the tunability of SHG range from 720 nm – 900 nm; the range of SHG was limited by the tunability range of excitation laser.

Nonlinear interaction of light in the ZnO submicron tubes generates excitonic UV emission centered at 385 nm at room temperature. An anomalous power dependence was observed for the UV emission peak on the pumping density and is attributed to a co-operative emission mechanism. Spatial measurements and nonlinear optical micrographs show a localization of UV emission at the ZnO SMR tip, and the generated UV light and SHG is guided through the long axis of the rod toward the tip. The polarimetry of nonlinear light generation from ZnO SMRs show a dipole symmetry for both UV and SHG radiation and is attributed to bulk nonlinearity from the ZnO rod. A "flipping" of SHG radiation symmetry was observed close to the tip of the rod. This could mean that either a blend of crystal structure or the asymmetry in the axial geometry may occur resulting in the “flipping” of SH radiation symmetry, and must be verified by high resolution TEM studies. An SHG efficiency equal to 4E-7 and 5E-7 was observed for s-polarization and circular polarization, respectively for a pump power of 15 mW. Localization of radiated photons was observed in the ZnO SMR array and is believed to be caused by the constructive interference of the multiple coherent scattering paths. The position control attained in the patterned array of ZnO rods via SAG method provides an additional controllability in shaping the propagation of NLO generated light.

6.2 Achievements

This dissertation demonstrated for the first time the enhancement of SHG via WGM mode confinement using GaN micro-cavities, demonstrated the discrete controllability of NLO processes using pyramidal geometry and showed an efficiency of 1.1E-7 at the SHG wavelength of 420 nm with 840 nm pumping for an incident power of 24 mW. NLO generation of light was observed from nonpolar InGaN/GaN MQW structures. Using patterned array of ZnO submicron rods on GaN pyramids, localization of SHG photons can be controlled via coherent scattering. A 90 degree change in the phase of SHG dipole radiation field was observed towards the tip of ZnO. To resonate with the aims mentioned in the introduction, 1) the range of the frequency conversion that can be achieved using semiconductor micro-cavities studied here was found to be from 720 nm – 900 nm, which was limited to the availability of laser line for pumping. The efficiency of GaN micro-cavities and ZnO SMRs were estimated to be of the order of 10^{-7}. 2) The back reflection geometry that was used in this optical study was not favorable to conclude whether the light emission from GaN micro pyramids was being efficiently harvested using ZnO rods/InGaN tubes as optical antennae. 3) The nonlinear processes from these structures can be controlled via varying the excitation/absorption cross-section of the geometrical structures studied here, modulating the power density and changing the pump polarization. 4) By using three different semiconductor structures and materials and a combination thereof affects the multi-photon induced emission energies. Using ternary and quaternary compounds of GaN, the efficient frequency range for SHG can be tuned.

6.3 Future Outlook

The intensity dependence of the NLO light generation from the apex of the 15 µm pyramid as discussed in section 3.3.2.2 shows an unexpected power dependence. The slope of the power dependence representing the number of photons showed a value of 3 and 4 instead of a 2 and 3. This means that a 3 photon transition was observed where a 2 photon transition was expected. This unexpected behavior was explained as due to high carrier density generation from high intensity pumping. A transition from EHP to stimulated emission was speculated. A slight change (~ 3 nm) in peak position was observed; however, this observation is very ambitious as it falls within the experimental uncertainty due to the resolution of the spectrometer. However, there was no change in the FWHM of the UV emission peak. Similarly, a higher power exponent value was observed for ZnO SMRs as well. In this case no change in peak maximum of FWHM was observed. One of the first improvements that can be initiated is to use a larger range of power variation at least of an order of 10. Moreover, studying the transient properties of the emission from these samples would provide more insight into the emission mechanism. Also, performing the power dependence measurements at low temperature would allow to reduce the thermal effects affecting the emission.

One of the predetermined goal of this dissertation was to study whether the ZnO SMR can harvest the light generation in the GaN micropyramid and transmit it efficiently. This is well tested in a transmission geometry set up. Unfortunately, this goal was not met due to unpolished back surface of the sample. Therefore, current measurements were all performed in the reflection geometry, where the sample was translated through the focus of the pump beam. Hence, excitation and collection was simultaneously done from the same axial plane. It would be interesting to do these measurements in a transmission geometry employing two objective lenses, where the excitation side objective as well as the sample remains stationary, while the collection objective is scanned through the axial geometry of the sample. Problems such as diffusion of carriers or optical losses may be encountered reducing the light harvesting/transmitting ability of ZnO SMR from the bulk of excited GaN pyramid.

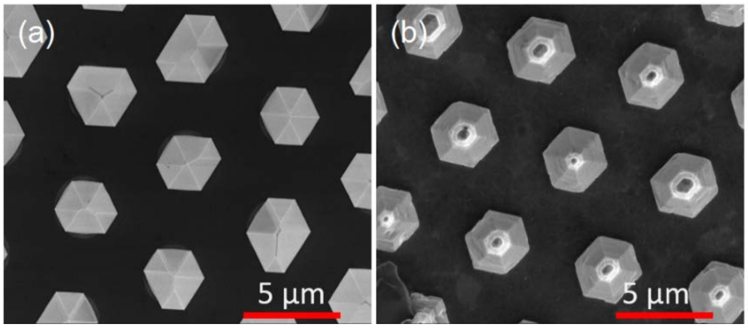

Figure 6.2. Orientation of individual crystal structures in a hexagonal lattice structure. (a) Hexagonal pyramids with facets facing each other, (b) Hexagonal pyramids with corners facing each other

Coherent scattering was observed in all the patterned samples. ZnO and GaN due to its wurtzite crystalline structure results in the fabrication of hexagonal structures. The orientation of the facets of the excited structure with respect to the neighboring ones as shown in figure 6.2 significantly affects the pattern and directionality of the coherent scattering. Figure 6.3 c and d represents the scattering patterns from samples with orientation in figure 6.2 b and a, respectively. Since the scattering patterns represented in figure 6.3 c and e are from differently oriented array, the individual structure shape is also different. It would be ideal to compare two samples with same structures in different orientation.

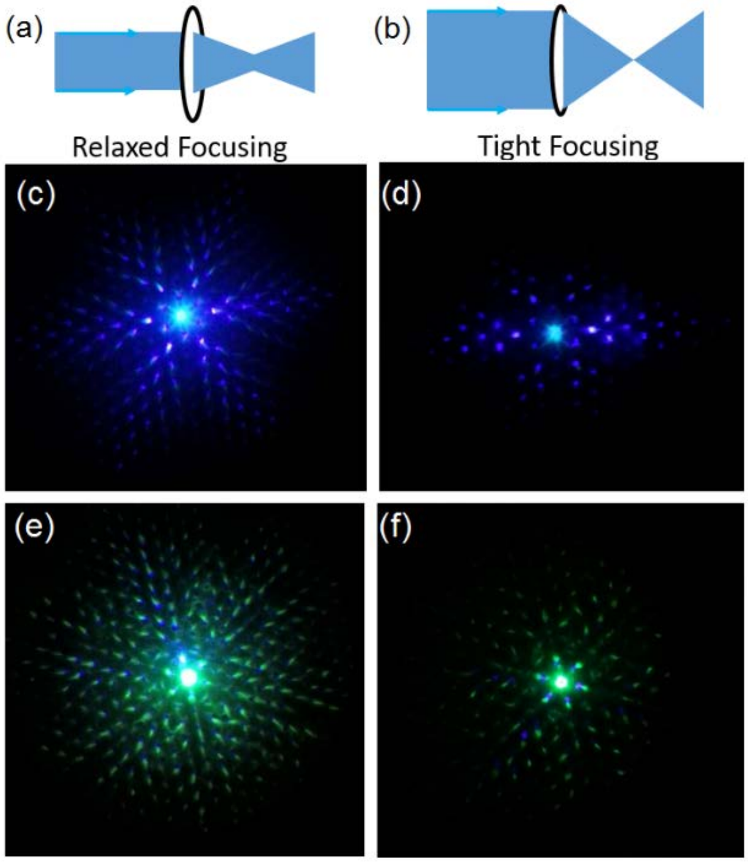

Figure 6.3.Coherent scattering pattern from ZnO rod on GaN pyramids and GaN pyramids.

It is well known that the numerical aperture of a lens system affects the light collection efficiency. The greater the NA is, the larger the efficiency of the collected signal is. The diffraction limited spot of an objective lens is usually calculated using either Abbe or Raleigh diffraction criteria. In order to apply this formula correctly, the back aperture of the objective lens must be completely illuminated using a telescope system to expand the usual 1 mm diameter laser beam. However, a common laboratory practice is pass the laser beam directly into the objective to pump samples. Although this doesn’t affect the lateral resolution significantly, the axial resolution may be significantly affected. Figure 6.3 a and c schematically represents the differences created in the focus without and with back aperture filling of an objective lens. Consequently, the coherent scattering pattern observed especially in the case of ZnO SMRs on

GaN pyramids is also different. A relaxed focusing shows six lobe scattering pattern, whereas, tightly focused beam shows dominant two lobe scattering pattern. The origin of the differences in scattering pattern/directionality is unclear and would be a study topic to consider in the future.

Understanding of the fundamental nonlinear optical properties from structures grown with position control can further used to improve the efficiency of nonlinear signal generation. Several strategies have been executed currently to explore the enhancement in efficiency of nonlinear signal such as WGM dielectric cavities[2,3] and using surface plasmon resonance (SPR) by incorporating metal nano-structures[4,5] and a combination of both[6] from randomly grown or dispersed single structures. Having demonstrated the existence of Quasi-WGM modes in GaN micro-cavity allows to extend this study to investigate the incorporation of SPR enhancements methods to increase the efficiency of SHG. The attempt to use a smaller size pyramidal cavity did not produce results with acceptable certainty due to inhomogeneous size and shapes of the hexagonal pyramid. It would be interesting to study a pyramid that is of the same order in size as the pumping or SHG wavelength. Use of the materials/ structures studied here could be effectively combined with photonic crystal (PhC) cavity design to enhance the NLO properties. Attempts in the two dimensional PhC direction have been made[7–10]; therefore, these structures in a PhC array would provide an additional dimensionality.